Creation and Optimisation of Plasma Etch Processes for the Manufacture of Silicon Microstructures

Christopher Bolton

Swansea University
Prifysgol Abertawe

Submitted to Swansea University in fulfilment of the requirements for the degree of Doctor of Philosophy

Swansea University 2022

Abstract

Microneedles are an area of growing interest for applications in transdermal delivery. Small, minimally invasive medical or cosmetic devices, microneedles are intended to penetrate the skin's outer protective layer (*stratum corneum*) to facilitate delivery of active formulations into the skin. Delivery of solution via microneedles has the benefits associated with hypodermic injection, i.e. avoiding the first-pass metabolism systems, with the added advantages of painless delivery and dose sparing from the reduced solution volumes required.

Advancements in semiconductor processing technologies and equipment have enabled the creation of devices and structures that could not have been fabricated in the past. This is also true for the fabrication of microneedles, where previous manufacturing methods have relied on hazardous chemicals such as Hydrofluoric Acid and Potassium Hydroxide to create the sharp tip of the needle, required to reduce insertion force.

In this thesis, the realisation of a hollow bevelled silicon microneedle fabricated using only plasma processing techniques is presented, providing a route to scalable manufacture of high-performance, sharp-tipped microneedles. The microneedle fabrication process consists of three main etch steps in the process flow to create hollow structures. For each of the Bevel, Bore, and Shaft processes the development and optimisation is detailed. Throughout the process development, several unexpected processing issues were encountered, including depth non-uniformity, "notching", and "silicon grass". Investigations have been performed to determine the root cause of each issue and fine-tune processes to optimise the final devices. A discussion of the process hardware is also presented, with reference to the benefits for each specific application process.

Following development and optimisation of each individual process, the Bevel, Bore, and Shaft processes were integrated in the manufacturing flow to create the final hollow silicon microneedle device. Issues arising from the combination of the three processes have been investigated, resolved, and optimised. This includes the conception and execution of a novel process for the plasma smoothing of an angled silicon surface, which improved the quality of lithography on the non-planar bevel surface and minimised grass formation.

Preliminary testing, undertaken to assess the suitability of these devices for transdermal use, included mechanical fracture force, skin penetration, and injection testing. The microneedles were found to be strong enough to remain intact during insertion, and demonstrate successful penetration and injection through the *stratum corneum* and into the deeper skin layers.

Information in this document has been redacted to protect the commercial interests of the sponsor company.

Declarations

This work has not previously been accepted in substance for any degree and is not being concurrently submitted in candidature for any degree.

Signed..... 

Date..... 30/03/2022

This thesis is the result of my own investigations, except where otherwise stated. Other sources are acknowledged by footnotes giving explicit references. A bibliography is appended.

Signed..... 

Date..... 30/03/2022

I hereby give consent for my thesis, if accepted, to be available for photocopying and for inter-library loan, and for the title and summary to be made available to outside organisations.

Signed..... 

Date..... 30/03/2022

The University's ethical procedures have been followed and, where appropriate, that ethical approval has been granted.

Signed..... 

Date..... 30/03/2022

Contents

Acknowledgements

Firstly, my thanks go to **Professor Owen Guy** and **Dr Sanjiv Sharma** for their help and guidance throughout this process.

I would also like to thank my employer SPTS Technologies Ltd, and all those at the company that have aided me in many and various ways. In particular, thanks to **Kerry Roberts** and **Roland Mumford** for fielding my questions, and my managers **Nigel Davies**, **Mark Carruthers**, and **Huma Ashraf**, not only for the technical advice, but also for the unwavering support and understanding during both my time on this project and my time with the company so far.

Thanks to my family who are always available when required. Especially **Sally Bolton**, my mother and biggest fan.

To my friends, **Kathleen Wallace**, **Brian Couper**, **Tom Offin**, **Nia Richards**, **Simon Dawson**, **Joe Taylor**, **Adam Beachey**, **Alex Wood**, **Alex Tompkins**, and several others who can't be named for fear of this section being too long. Your constant encouragement, advice, and distractions have kept me sane and productive. Thanks to you all for supporting me to the end.

And finally; **Tiggy**, **Tess**, **Frankie**, **Sparky**, **Scamp**, **Dash**, and **Marms**. You have helped me in ways impossible for you to comprehend, and my time with each of you will never be enough.

“Plan for cloudy with a chance of anvils” – Aesop Rock

Abbreviations

3D	Three Dimensional
APC	Automatic Pressure Control Valve
AR	Aspect Ratio
CD	Critical Dimension
CMP	Chemical-Mechanical Polishing
DC	Duty Cycle
DI	De-Ionised
DOE	Design of Experiments
DRIE	Deep Reactive Ion Etching
ER	Etch Rate
ESC	Electrostatic Chuck
HF	Hydrofluoric Acid
HFr	High Frequency
ICP	Inductively Coupled Plasma
IP	In-Plane
KOH	Potassium Hydroxide
LFr	Low Frequency
MB	Methylene Blue
MEMs	Microelectromechanical Devices
MN	Microneedles
OCT	Optical Coherence Tomography
OOP	Out-of-Plane
POR	Process of Record
PPE	Personal Protective Equipment
PR	Photoresist
RIE	Reactive Ion Etching
RF	Radio Frequency
SEM	Scanning Electron Microscope
TSV	Through-Silicon Via
UDRIE	Ultra-Deep Reactive Ion Etching
UV	Ultraviolet

Units

µm	Micrometre
nm	Nanometre
mm	Millimetre
s	Seconds
min	Minute
hr	Hour
Hz	Hertz
W	Watts
N	Newtons
°	Degrees
°C	Degrees Celsius
mT	Millitorr
sccm	Standard Cubic Centimetres per Minute
µl	Microlitres

List of Figures

List of Tables

Publications

Lab on a Chip, Volume 20 Issue 15, p.2788-2795, 2020

C. J. W. Bolton, O. Howells, G. J. Blayney, P. F. Eng, J. C. Birchall, B. Gualeni, K. Roberts, H. Ashraf, O. J. Guy

"Hollow silicon microneedle fabrication using advanced plasma etch technologies for applications in transdermal drug delivery"

DOI: 10.1039/d01c00567c

IEEE 71st Electronic Components and Technology Conference (ECTC), 1st June - 4th July 2021

S. Suhard, K. Kennes, P. Bex, A. Jourdain, L. Teugels, E. Walsby, **C. Bolton**, J. Patel, H. Ashraf, R. Barnett, F. Fodor, A. Phommahaxay, D. La Tulipe, G. Beyer, E. Beyne

"Demonstration of a collective hybrid die-to-wafer integration using glass carrier"

DOI: 10.1109/ECTC32696.2021.00325

ECSCRM Conference, 24-28th October 2021

B. Jones, J. Mitchell, J. Evans, F. Monaghan, M. Jennings, **C. Bolton**, K. Riddell, H. Ashraf, O. Guy

"Introducing Foundry-Compatible SiC and GaN Trench Processing Technologies for Reliable Automotive Application"

DOI: 10.4028/p-xd84zm

CS Mantech Conference, 9-12th May 2022, paper abstract accepted

A. Croot, F. Monaghan, **C. Bolton**, K. Riddell, H. Ashraf, B. Jones, J. Mitchell, J. E. Evans, M. R. Jennings, O. J. Guy

"Rounded base corners in SiC trenches for power MOSFETs"

Hilton Head Workshop, 5-9th June 2022, paper abstract accepted

A. Lotfi, M. P. Hardin, Z. Liu, A. Wood, **C. Bolton**, K. Riddell, H. Ashraf, J. Carpenter, F. Ayazi

"Wafer-level high-aspect-ratio deep reactive ion etching of 4H-Silicon Carbide On Insulator substrates"

Best Poster Award – Runner-Up

Patent Pending, Lodged 22/12/21

R. Mumford & **C. Bolton**, for SPTS Technologies Limited

"Method of reducing surface roughness"

Application Number GB2118859.4

Chapter 1

Introduction

An overview is given of basic concepts of microneedles, their manufacture, and applications. The history, development, and benefits of microneedles are discussed, and the main aims of this project are defined.

1.1 Introduction

Advancements in the processing of silicon microstructures have made possible devices that would previously have been inconceivable. The semiconductor processing industry is continually looking to advance capability in line with the demands of device manufacturers, allowing increasingly complex structures to be produced [15-18].

With the conception of each new device, extensive developments and optimisations must be carried out to improve their effectiveness and reliability for their intended purpose. Each microstructure can have several process steps in their manufacture using a range of semiconductor processing techniques. For example, process types can be plasma (dry) [15, 18-20] or acid (wet) [21-24] based, and depending on the desired outcome can be etching [19, 23, 24], deposition [25], cleaning [26-28], or smoothing [29, 30]. The job of optimising these processes is often the responsibility of Process Engineers, whose focus within an institution is usually the improvement of the multitude of processes used in the complex manufacture of microstructures.

The focus of this thesis is the development, optimisation, and manufacture of novel silicon microstructures using state-of-the-art semiconductor plasma processing techniques. The structures chosen for this work are microneedles, the concept of which will be explained in more detail in the following sections. The techniques used to process the devices will be described, and the results of developmental and optimisation studies will be presented.

1.2 Microneedles

1.2.1 Introduction to Microneedles

Microneedles (MN) are a cover-all term to describe micron-scale minimally invasive devices for penetrative cosmetic or medical purposes [31, 32]. The primary purpose of

microneedles is to penetrate the protective outer skin layer (*stratum corneum*) and facilitate the transport of fluid, agents (e.g. vaccines) or particles to the dermal layers where solutions can be absorbed, agents can interact with specific cells in the skin compartment and drugs can be delivered locally or systemically – depending on the depth of penetration and efficacy of transdermal drug transport [31, 32]. Without MN penetration, the intact *stratum corneum* otherwise acts as a barrier which prevents significant transdermal fluid absorption due to its hydrophobic qualities [32, 33].

The first patent for a microneedle device was granted in 1976 for Martin Gerstel and Virgil Place for the Alza Corporation [34], and was granted for several conceptual designs of polymer and metal needles. The first proof of concept study on the use of microneedles for transdermal delivery applications was not published until 1998 [35]. Interest in microneedles has been growing since then. A literature search for the term 'Microneedles' reveals just 127 publications in 1998, rising to 2770 in 2020. Spikes in publications occurred in 2012 and 2021 and are probably linked to events that occurred 1-2 years prior, the 2009-10 H1N1 Swine Flu and 2019-current SARS-CoV-2 COVID-19 pandemics likely causing a surge in research in response to world events.

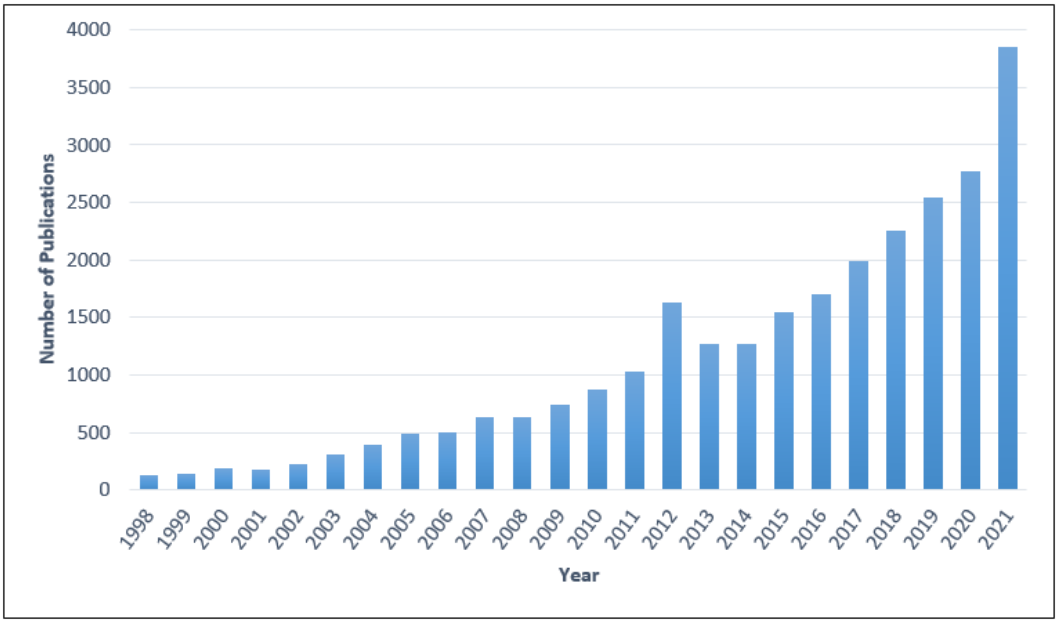

Figure 1.1. *Chart showing the increase in research publications related to microneedles by year.*

Microneedles have been developed for a variety of applications and can usually be separated into the categories of cosmetic or medical devices. Cosmetic microneedles, as implied by the name, focus on the treatment of superficial skin appearance. Examples of this include scars [36, 37], skin conditions [38, 39], and beauty products [40, 41]. The transport of the formulation through the *stratum corneum* can significantly increase the availability of active molecules in the deeper skin layers in comparison to simple topical cream applications [42-45] by bypassing relatively impenetrable outer skin layers [32, 40, 43]. This is particularly so for hydrophilic or water soluble molecules and for large molecules – both of which have minimal penetration through the *stratum corneum* [33].

There are also several medical applications for microneedles, where the target is not the skin but the vascular system to allow direct absorption of the therapeutic solution into the bloodstream. Some medical applications for microneedles include insulin delivery [46-50], allergy testing [49, 51], protein delivery [52], and brain implants [53]. Vaccines are also an area of significant interest for MN, with inoculations delivered by microneedle being

developed for Influenza [54-56], Anthrax [57], Coronavirus [58], and Hepatitis B [59]. The use of MN to administer vaccines is of particular interest due to the reduced training required to give the inoculations and the reduced dose needed compared to intramuscular injection [54, 56-59].

1.2.2 Existing Microneedle Designs

The general physical form of microneedles can be described as one of five major groups. These are Solid, Coated, Dissolving, Porous, and Hollow. Illustrations of each type can be seen in Figure 1.2.

- **Solid Microneedles:** These are the simplest form of microneedle, and consist only of a structure protruding above the baseplate (substrate) that the MN is created on. The fundamental purpose of solid microneedles is simply to penetrate the skin layers, and thereby create a conduit in the outer skin layer, through which liquids can passively diffuse into the body [32]. The delivery method using solid MN is often referred to as 'poke and patch' due to the method of usage being to create the holes in the skin before applying the intended substance to the surface [60].
- **Coated Microneedles:** Similar in initial design to the solid MN form, coated microneedles consist of solid MN covered in a formulation containing a substance that needs to be absorbed by the skin. In reference to purely solid MN, coated microneedles application is referred to as 'coat and poke'. Their application relies on the ability of the coated substance to diffuse from the MN coating formulation into the skin *in situ*, improving efficiency of the delivery [61]. Dosage is limited to the amount of coating that can be applied to the surface area of the MN [62], and thicker coatings can reduce the sharpness of the MN tip and limit the ability to penetrate the skin [63]. The incorporation of the active

agent into the formulation and the adhesion of the formulation to the MN also need to be considered, as well as the diffusion release of the active agent from the coating [64].

- **Dissolving Microneedles:** In this design, the tip of the MN is formed from the substance to be absorbed rather than the material of the MN body – the material to be inserted into the skin forms the sharp tip to the MN. Once inserted, the formulation is dissolved in the interstitial skin fluid and absorbed [65-67]. This allows a higher volume of material to be inserted per MN than the coated variety (but is still limited by volume).
- **Porous Microneedles:** As opposed to the coated and dissolving MN, porous microneedles contain the active solution in cavities in the porous MN surface which hold the formulation while the microneedle is inserted, rather than having the solution on the external MN surface. This allows the formulation to diffuse into the skin from the porous surface once *in situ* [68-70].
- **Hollow Microneedles:** This design contrasts all the other varieties of MN, which rely on passive diffusion. The hollow microneedles utilise a hole that reaches all the way through the MN, known as a bore, to flow solution from a reservoir behind the MN and into the skin [71]. In this way, increased doses can be administered with ease due to the injection capabilities similar to hypodermic needles. The presence of the bore leads to several options for MN design, including with the bore central [13, 72, 73], offset [14, 74, 75], or exiting the side of the MN [76], though this flexibility with design comes at the cost of complex manufacturing methods required to integrate the bore into the microneedle shaft.

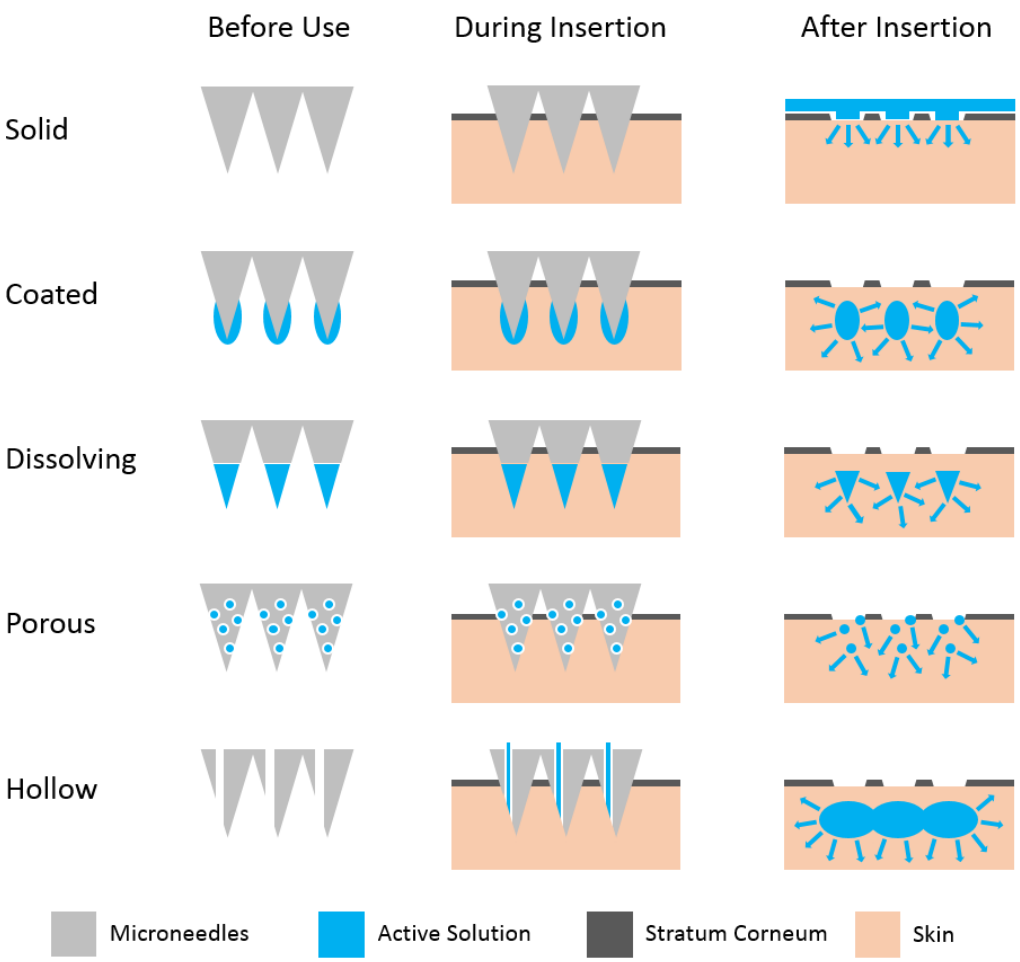

Figure 1.2. *Graphic representation of different microneedle types, showing the mode of solution delivery into the skin.*

1.2.3 Microneedle Materials

Microneedles can be manufactured from several different materials. The most common materials used to fabricate microneedles are Polymer [77, 78], Metal [79, 80], Ceramic [70, 81], and Silicon [9, 82, 83]. The microneedles created with each material also contain several possible variations, with the specific design and application dictating the exact material used for fabrication.

Polymers are a popular choice for the fabrication of simpler microneedle designs, partially due to their ease of manufacture and low production cost. Some examples of polymers used for microneedle manufacture are polycarbonate [78], photoresists [84-86],

and various printable or mouldable plastics [77, 87, 88]. Microneedles fabricated from polymers do encounter some issues with the more complex designs due to the typical manufacturing methods employed, namely printing, lithography, two-photon polymerisation, or moulding. Most polymer MN are manufactured to be solid [61, 86, 88-90], coated [49, 91], or dissolving [66, 92, 93]. Some hollow polymer microneedles do exist [94-97] but integration of the bore has some difficulties related to the common additive manufacturing methods and reduced MN strength with less material, so to avoid these issues there are also designs that utilise an open channel design for passive diffusion [87, 98, 99].

Metal [79, 80], and Ceramic [70, 81] MN are less common. Metal and ceramic MN can be manufactured using the sintering process [100], but for hollow MN the most common method of bore production is CNC micro-milling which can be hard to reproduce in a production environment [101]. Metal microneedles, while generally being biocompatible, can induce allergic reactions in some cases [102]. Physical micromachining/milling is also an expensive method of fabrication, leading to a high cost (~$200 per patch) [101].

Microneedles manufactured from silicon are biocompatible [74] and offer a good alternative to both polymer and metal, in terms of cost and performance. The method of fabrication is also highly scalable. Semiconductor processing is a mature technology, having been used in production environs for decades to mass-manufacture commercial components [15, 17, 18]. The mature processing techniques also provide an excellent basis for the development of new and complicated designs [15-17]. Fundamentally, the biggest restrictions with silicon processing are the cost of material and capital equipment costs. Costs decrease with higher throughputs in manufacturing environments, but this limits low-volume production and development [15]. However, the benefits in performance can justify even expensive, low-volume production in niche, high value applications, whilst mass production can reduce costs to levels viable for cosmetic and vaccine products.

1.3 Silicon Microneedles

1.3.1 In-Plane and Out-of-Plane Manufacture

Silicon is a commonly used material for microneedles because of the design flexibility afforded from the extensive methods of semiconductor manufacture. This allows new shapes to be conceived and implemented, without some of the restrictions imposed on traditional microfabrication methods required for metal processing [100, 101].

Semiconductor grade silicon comes in the form of a wafer, a round disc which can be processed into devices [103]. In the case of microneedles, the aim is to produce sharp protrusions out of the wafer that can then be inserted into skin. Using silicon wafers, there are two main ways to manufacture structures like this which are known as in-plane [104-106] and out-of-plane [76, 105, 106].

- **In-plane (IP):** Microneedles are manufactured such that they are in the in the plane of the wafer. This allows longer needles to be manufactured as the limit is effectively the diameter of the wafer. The drawback with this type of structure is the limit on numbers of devices per wafer due to their increased size, and the process/manufacturing complications associated with completely removing the Si from areas of the wafer and additional steps involved with adding a bore [82].
- **Out-of-plane (OOP):** Structures are fabricated perpendicular to the wafer surface. This increases the number of devices per wafer compared to In-plane designs and avoids the issues with through-etching large parts of the wafer. However the height of the MN is limited by the thickness of the wafer [76]. This is not considered to be a major issue, as the purpose of MN is to be less than

1mm in length in order to avoid pain from injection related to longer needles stimulating the nerves beneath the dermis.

Figure 1.3 shows a graphical representation of these two MN types.

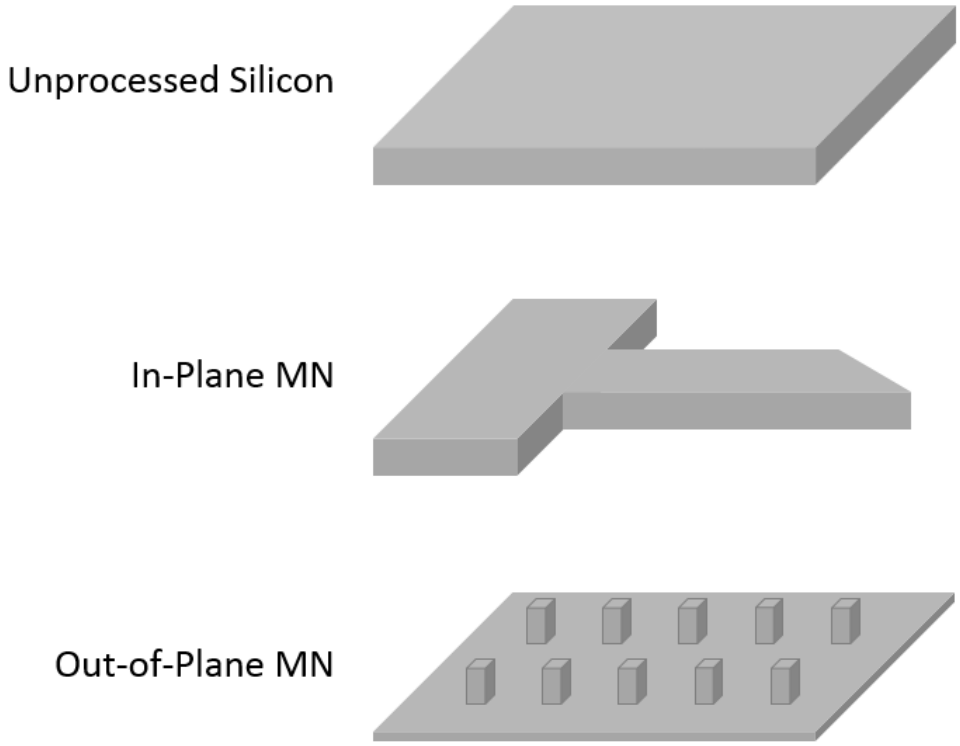

Figure 1.3. *Graphic representation of In-Plane and Out-of-Plane microneedles. IP MN are manufactured from the width of the silicon, and OOP MN are produced from the thickness.*

Both IP and OOP methods are effective ways to produce silicon microneedles, though for different applications. The length afforded to in-plane MN makes them ideally suited for probes into hard-to-reach areas [82, 107]. This length is not required for transdermal delivery [38], for which the increased device per wafer numbers offered by OOP MN make this the preferred device type.

1.3.2 Forms of Microneedle Design

As well as orientation of device in relation to the wafer, there are several options for the design of the microneedle itself. These were previously described in Section 1.2.2, and all

these forms are possible in silicon-based manufacture. Dissolving MN tend not to be produced in Si due to the relative simplicity of design, meaning that Polymer MNs offer the best value, albeit with reduced performance, if that is the development target.

Porous silicon microneedles can be produced by the use of Hydrofluoric Acid (HF) in electrochemical, metal-assisted, or stain etching to produce nano-pockets in the surface of the microneedle [68, 108, 109]. These pockets provide areas for the active solution to be passively captured, then allowing diffusion into the skin once the MN is inserted [68-70, 108].

There are several examples of solid [9, 11] and hollow [13, 14, 74, 105, 110] silicon microneedles reported in the literature (Figure 1.4) and these can be broadly described by their physical characteristics, specifically the presence of a bevel, shaft, and bore. These features can be seen graphically in Figure 1.5. These characteristics can take several forms in practice, but can be differentiated based on the function they provide. A bevel provides a sharp surface for insertion, a shaft increases length for depth of insertion, and the bore is a conduit through which a solution can be flowed. Variations of these very simple illustrations are possible, such as hollow MN with no bevel [13] or a sharp rim [73], or side-exiting bore holes [74, 76]. The limits of MN design are not strict and can be expanded with the advent of novel process solutions. Currently the production of hollow bevelled MNs is completed either using Potassium Hydroxide (KOH) [75] or HF [14] to achieve the angled bevel surface, dangerous wet chemicals that require extensive training and safety procedures [111, 112], or plasma etching technology that results in a shape not immediately recognisable as a needle [73, 74]. Finding a new way to produce hollow bevelled silicon microneedles while avoiding the existing techniques of bevel production is a direction that can be explored further.

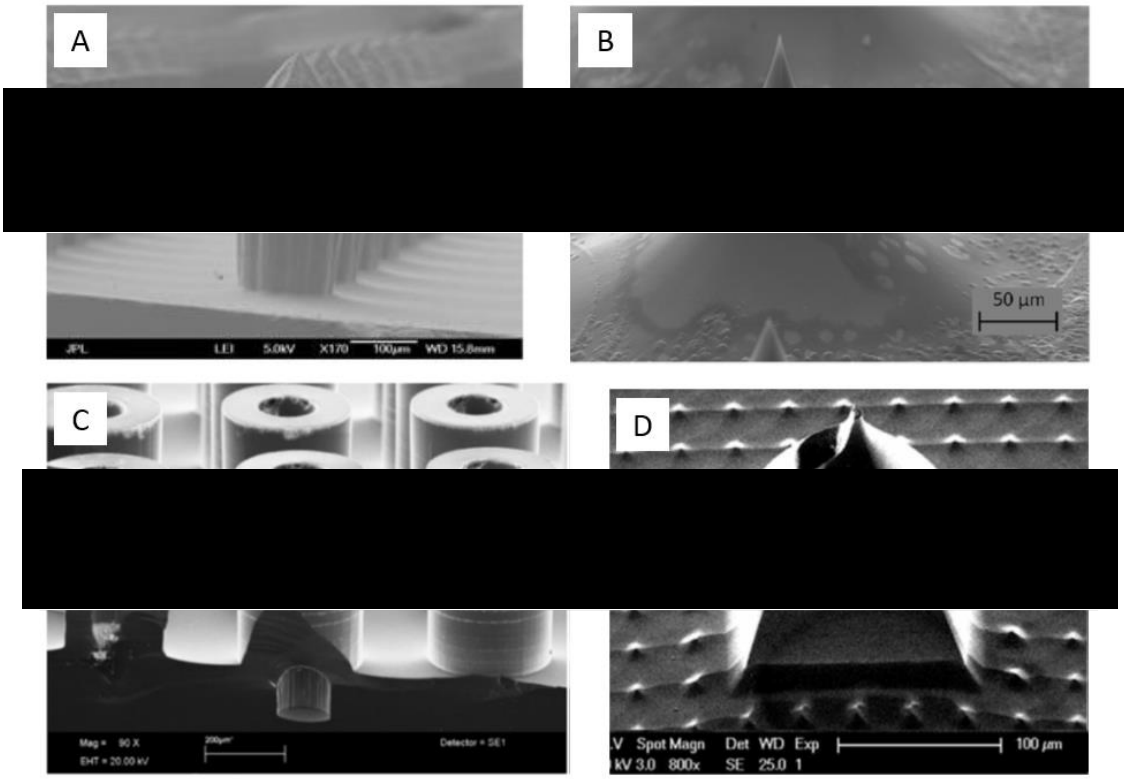

Figure 1.4. *Examples of silicon microneedles from literature. A) Plasma etched solid MN showing a bevel and shaft [9]. B) Solid MN with an angled bevel surface [11]. C) Hollow MN fabricated with plasma etching, consisting of a shaft and bore [13]. D) Wet etched hollow MN, with a bore exiting on a bevelled surface [14].*

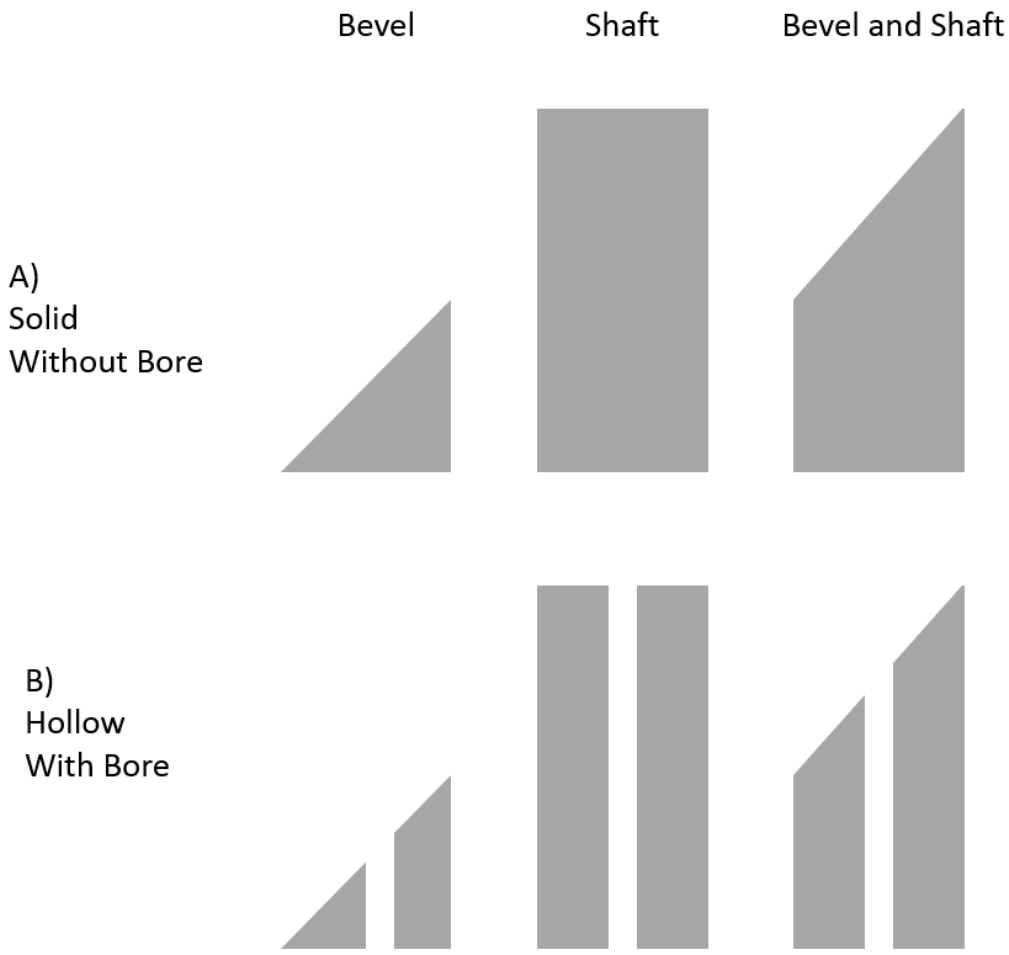

Figure 1.5. *Illustration of basic MN physical characteristics. Each of the features can be varied in appearance and combined to give the required form for the application. Row (A) shows each of the bevel and shaft combinations that form Solid MN, while row (B) shows these variations with the bore in place to give Hollow MN.*

1.3.3 Commercial Silicon Microneedles

Examples of silicon microneedle devices are currently available on the commercial market. One such device is the MicronJet from Nanopass which was the first <1mm MN device to receive clearance from the U.S. Food and Drug Administration (FDA) for intradermal drug delivery [113]. The design is hollow, consisting of only a bevel and bore with no shaft, with three MN present in a single array, suitable for therapeutic or cosmetic applications [4]. The bevel in this case is achieved using wet KOH etching of the silicon

substrate before a dry plasma etch is used to create the bore [110]. Images can be seen in Figure 1.6a.

DebioTech also have a product on the commercial market. Also a hollow MN, their DebioJect design [114] is offered as an array of microneedles or a single MN, with several height options. The structure of the MN is a conical top with a long vertical shaft, and a bore hole that exits through the side of the MN near the top, as can be seen in Figure 1.6b. The DebioJect device has been shown to offer effective delivery of a Rabies vaccine [10] and Cells [38], and a spring mechanism in the applicator ensures efficient penetration of the MN [115].

Another silicon MN that can currently be purchased is the device available from U-needle [116]. Their Bella-mu product is a single microneedle rather than an array, manufactured from silicon with a long shaft and hollow bore [117]. Bella-mu primarily focuses on pharmaceutical applications, such as dose sparing of vaccines [116]. It is an intradermal injection device, so is longer than other available microneedles, and is fabricated by producing the long MN in-plane, before bonding into an application device to reduce the usable height to target the intended depth in skin, as shown in Figure 1.6c [12].

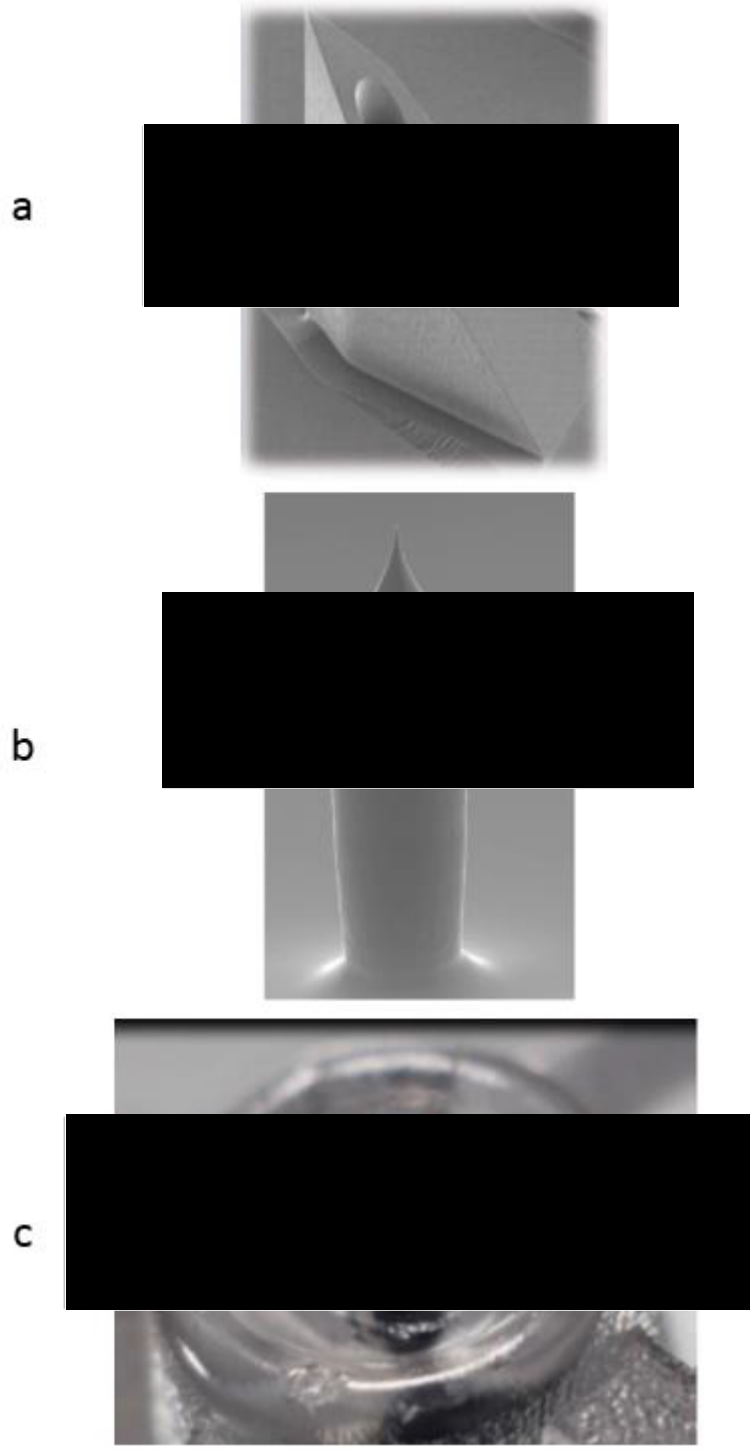

Figure 1.6. *Images of commercial silicon microneedles. a) Nanopass MicronJet, 600µm tall from base-to-tip with a bevelled surface for insertion [4]. b) DebioTech DebioJect, 750µm tall with a side-exiting bore at approximately 500µm from the base [10]. c) U-needle Bella-mu, height is controlled by setting the needle in epoxy giving the functional length of the device [12].*

1.4 Skin Architecture

On the macro scale, skin consists of 3 main layers. The innermost layer is the hypodermis, which is mostly adipose tissue and provides a platform for the second layer, the dermis. The middle layer in the skin's composition, the dermis contains structures such as hair follicles, sweat glands, nerves, and blood vessels surrounded by collagen [71]. The sweat glands and blood vessels in the dermis are the main tools used to regulate the temperature of the body. The outermost layer is known as the epidermis, and is the body's protective barrier against external environments. These layers can be seen graphically in Figure 1.7.

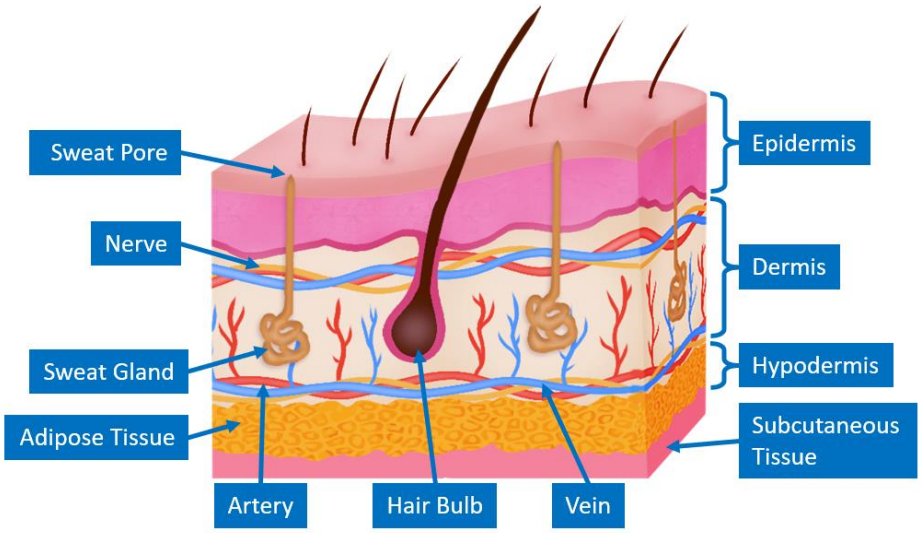

Figure 1.7. *Diagram of the dermal skin layers, showing the difference between the epidermis, dermis, and hypodermis [2]. The typical combined thickness of these three layers is 1.69 to 2.28mm in the upper arm [8].*

The epidermis can be further split into distinct layers, as can be seen in Figure 1.8. 90% of the skin cells in the epidermis are keratinocytes of some form [118]. Starting next to the dermis, the *stratum basale* is the lowest layer in the epidermis and keratinocytes are formed here. As keratinocytes age, they migrate up through the epidermis due to the production of new cells in the *stratum basale* [119]. Once in the *stratum spinosum*, keratinocytes stop proliferating and begin the process of keratinisation, continuing to move towards the surface

as they age [120]. The *stratum granulosum* is comprised of keratinocytes that have lost their nuclei, with the layer being named for the granular appearance of the cytoplasm in the dying cells [121]. Beyond the *stratum granulosum* layer the keratinocytes are dead, and in some places on the human body (such as palms or soles of feet) they then form the *stratum lucidum*, an additional barrier providing more thickness to the skin [118, 122]. The final layer of the epidermis is the *stratum corneum*, a layer usually <20µm in thickness entirely comprised of dead keratinocytes (AKA corneocytes) [123, 124]. In the *stratum corneum* these corneocytes provide a barrier to penetration from microbes and toxic substances, as well as the hydrophobic qualities to prevent significant absorption of solutions into the skin [33]. After some time in the *stratum corneum* and on the outer surface of the skin, corneocytes undergo desquamation and are shed from the skin's surface.

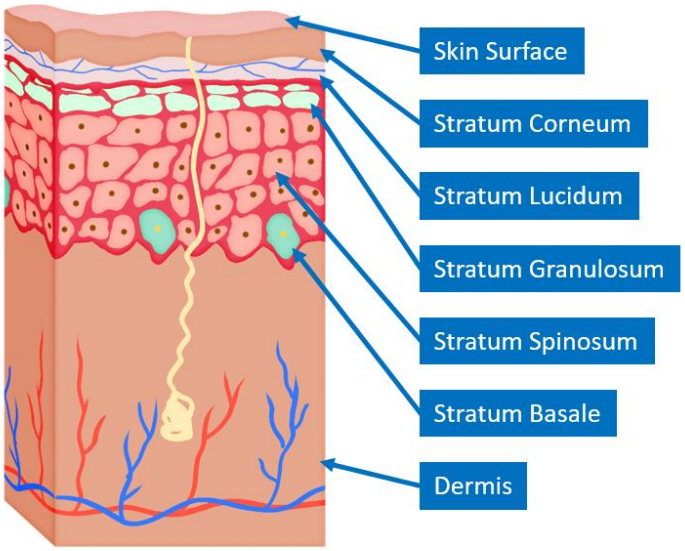

Figure 1.8. *Illustration of the individual layers that make up the epidermis, from the surface of the skin down to the dermis [3]. The epidermis on the shoulder can be up to 110µm thick, with the stratum corneum typically less than 20µm [7].*

Together, these layers make up the most expansive organ of the body, accounting for 16% of an average person's body mass [63]. In addition to its functions of sensing temperature, contact, and pain, the skin plays a vital role in repelling harmful substances or

microorganisms away from the bodily internals where they might be able to cause illness [33].

1.5 Microneedles Vs Hypodermic Needles

1.5.1 History of Hypodermic Needles

The advantages of introducing foreign substances beneath the epidermis for medical applications are seen during the development of modern vaccinations, notably with the smallpox inoculations carried out in Asia and the Middle East, before being studied by Dr Edward Jenner and reported in 1798 [125].

Medical treatment by injection was popularised in the 19th century after the invention of the first skin-piercing hollow hypodermic needle by Dr Alexander Wood [126]. This allowed for repeatable and less invasive injection of materials into the patient's system when combined with a syringe to control dose. This has been the primary technology for all sub-dermal injections since Dr Wood's original design, but the basic principle and overall technology has not changed much for modern applications. While hypodermic needles offer many advantages over other types of drug administration there are still areas that can be improved with the development of new technologies.

While hypodermic needles are readily available and used for many medical applications, they have some drawbacks which are overlooked due to the benefit they introduce to the patient. When injected with a traditional hypodermic needle, the patient will typically experience pain associated with puncture into the subcutaneous layer under the skin. This is a particular problem for children who may not understand the health benefits of such a treatment or immunisation, which can induce a lasting 'needle phobia' that stays with the

individual into adulthood [127]. This pain can also be an issue for people who must self-medicate using hypodermic needles, such as Type 1 diabetics.

Hypodermic needles also require safety training to correctly administer treatments to patients, as sharps injuries are common among even trained professionals. In 2008, the Royal College of Nurses commissioned a survey which showed that 96% of UK nurses use needles, and 52% "fear needlestick injury either 'a great deal' (23%) or a 'fair amount' (29%)" [128]. 48% of those surveyed had experienced an injury by a sharp that had already been used on a patient, leading to an increased risk of infection for the nurse [128]. A later study by Saia *et al.* in 2010 estimated that 100,000 injuries are caused by sharps among UK medical professionals every year [129]. This need for training to avoid injury and administer the appropriate dosage to the correct depth in the skin is a limiting factor in the speed with which vaccinations can be deployed in certain circumstances. Many developing countries may have a shortage of trained medical staff to combat epidemics before international intervention. This also extends worldwide to pandemic episodes, where many people need to be treated with a limited number of medical staff available.

Due to the prevalence of needlestick injuries, safety protocols for the handling of sharps are needed to protect individuals who may come into contact with these items. All medical professionals that are required to use, or otherwise come into regular contact with, sharps such as hypodermic needles must receive training in their safe handling and protective equipment to minimise this risk [130, 131]. However, disposal of these objects is also a major concern, as this can also expose waste disposal staff to the dangers associated with medical sharps. As such, protocols are also required for the removal of any sharps waste, increasing the number of people needed to be specifically trained to safely handle sharps at all stages of the usage cycle [132].

A typical disposal scheme requires the use of dedicated sharps bins to be removed by trained waste removal staff to a facility that specifically deals with the destruction or incineration of potentially hazardous materials. For self-medicating patients this is often not the most common method for discarding needles; a survey in 2003 by Olowokure *et al.* showed that only 12-14% of the diabetic population is estimated to use this disposal method [133]. In the same survey, 84% of people who had a normal amount of sharps awareness disposed of blood-stained materials either loose in household rubbish or contained in a drinks can, bleach bottle or other makeshift household receptacle [133]. These patients may feel conscious of leaving a dedicated medical bin outside their homes, but this unsafe disposal of used needles and other sharps in normal household waste exposes many more people to potential injury or infection [133-135]. People encountering sharps in this way may not be expecting to come across such material and are therefore less vigilant to the dangers associated with needlestick injury and potential infection risks.

Although hypodermic needles possess a high risk of injury or infection, even when handled correctly, their advantages are also extensive. Being a mature technology with several decades of development, the manufacture of hypodermic needles is optimised to a high degree. When stored in the correct conditions they do not spoil, so can be stockpiled for rapid deployment. With the correct training, depth of injection and minimisation of injury risk can be somewhat controlled to achieve effective transdermal delivery in the safest way possible with the technology available [136].

But despite time consuming and exhaustive control methods, needlestick injuries are estimated to cause 2 million cases of serious infection among healthcare workers worldwide annually according to a WHO-ICN collaboration on the prevalence of such injuries. This is also noted as probably being a low estimate, based on “the lack of surveillance and underreporting of injuries” [130], with one survey of UK professionals indicating the rate of

non-reporting could be in the region of 50%, due in part to a low perceived risk of infection [137]. It would therefore be beneficial to replace hypodermics where possible for an alternative injection device, which can provide a better safety standard to self-injectors, professionals, and waste disposal staff while maintaining efficient transdermal delivery.

1.5.2 Benefits of Microneedles

When compared to hypodermic needles, MN are considered painless due to their minimally invasive nature [138, 139]. The length of the microneedle means that the nerves in the deeper layers of skin are not stimulated, and with this reduced discomfort the phobia associated with injections and needles is also lessened [127, 138-140], facilitating self-injection for more people who would previously have not considered it.

As well as reducing the risk of outright injury from penetration, the risk of infection when using microneedles is lower than their hypodermic counterpart [60, 140, 141], and this combination results in medical professionals being exposed to a significantly lower level of risk from sharps injuries [130, 132, 139-141]. This is also beneficial for the intended use of the MN, with patients experiencing lower risk of post-injection microbial infections [60, 140, 142].

By utilising transdermal delivery, microneedles bypass the gastrointestinal tract and first-pass metabolism systems [62, 93, 123, 142]. This results in an increased efficacy of administered solutions, meaning that reduced doses can be given to achieve the same results which extends the supply of the active formulation [31, 93, 143, 144].

Additionally, due to their diminutive stature and lack of direct injury risk, microneedles don't require the same dedicated disposal practices as other medical sharps [60]. For cases of repeated self-injection, such as IVF or diabetes, this ease of disposal is beneficial for the injecting individuals and improves compliance with local waste protocols. This leads to a

reduced risk of workers unexpectedly encountering and being injured by incorrectly disposed medical sharps [60].

Despite these benefits microneedle uptake has been slow, particularly in the medical sector. This is in part due to unfamiliarity with MN devices but can also be partially explained by the advantages of the MN overlapping with areas of lower priority for medical applications such as pain reduction, and that MN have limited use in intramuscular applications where hypodermic needles excel. With sufficient training, the hypodermic needle provides a good all-in-one injection platform in an understood and mature technology. However, with additional understanding in the general populous of the advantages of MN, they could be adopted for specific applications.

To summarise, the key advantages of microneedle use compared to hypodermic needles are bypassing the first-pass metabolism systems [62, 93, 123, 142], painless delivery [60, 145-147], dose sparing [31, 93, 143, 144], targeted delivery via shallow injection [148], easier disposal practices [60], reduced fear of injection [127, 138-140], and less risk of post-insertion infection [60, 140, 142].

1.6 Project Overview

The initial conception of a new hollow bevelled silicon microneedle structure using only dry plasma etching technology occurred before the commencement of this research with a patent being filed in 2018 by Roberts *et al.* for SPTS Technologies Ltd. The patent was granted in Europe in 2020 [149], and in the US in 2021 [150].

Initial development of these fabrication steps was completed on previous generation plasma processing hardware. Although the quality of the resulting products was enough to show that the concept could be realised, there was significant improvement possible with

the transfer to current generation etch tools. The use of state-of-the-art processing hardware in this body of work also presented the opportunity to study the new processes involved both individually and together, allowing potential improvement, optimisation, and learning to be achieved through in-depth process development. The goal of this project was the microfabrication of a functional device using state-of-the-art machinery, with the secondary objectives of process optimisation and understanding the mechanisms and processes involved to improve results.

During the development of new processes and applications issues are to be expected, especially in the case of multiple processes being combined. Unforeseen consequences are common due the complexity involved with device processing, however when these issues were encountered the aim was to generate novel and effective solutions to allow improved fabrication steps in the future.

Upon the fabrication of microneedle devices, basic proof-of-concept experiments were conducted to demonstrate functionality of the final device structure for skin penetration and transdermal delivery. Although a dedicated study would be required to fully assess the effectiveness and biocompatibility of the devices, initial testing determined their potential for transdermal delivery.

1.7 Design and Process Flow

The fabrication of hollow silicon microneedles relies on three main silicon etch processes. Each of these will be explained in detail including motivation, benefits over current methodology, plasma process development, and results achieved.

Figure 1.9 details all the stages in the fabrication sequence, showing cross-sectional schematics for each major etch step in the sequence. Each process step provides a specific functional benefit to the final form of the microneedle:

(A) Bevel; it has been found in previous studies that a bevelled microneedle results in greatest penetration, allowing easy insertion into human skin with lower forces [73, 151]. The curved shape to the bevel etch ensures that the bevel does not continue too far down the microneedle.

(B) Bore; the central hole through which fluid will be transported from the syringe into the sub-dermal layers of skin after microneedle penetration.

(C) Shaft; this provides the vertical height to the microneedles. Full MN insertion depth can be determined by controlling the etch time of this process, allowing different layers of skin to be targeted depending on application.

In the subsequent chapters, the development and optimisation of the plasma etch processes for the creation of Hollow Silicon Microneedles will be detailed.

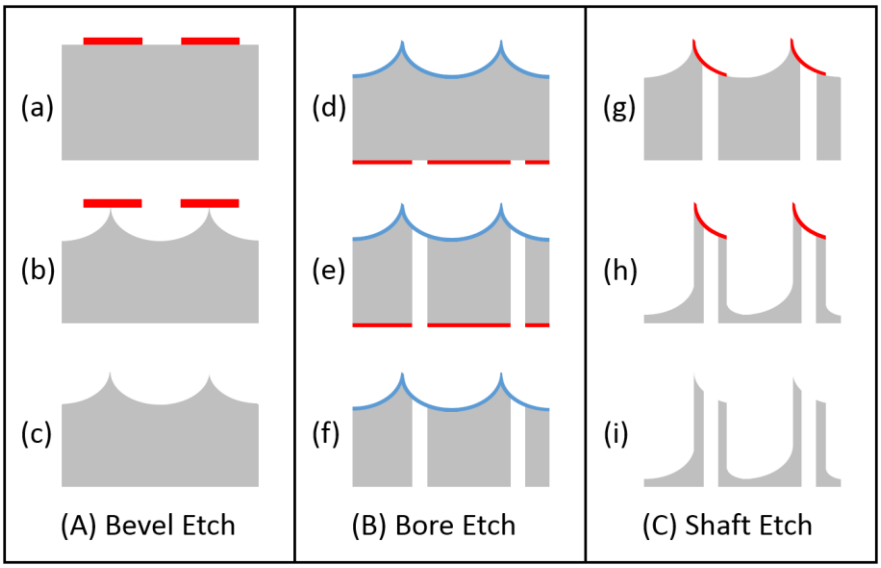

Figure 1.9. *Schematic diagrams of main process fabrication steps, partitioned by individual etch processes. The silicon substrate is shown in grey, masks are shown in red, and etch stop layers are shown in blue. The columns (A), (B), and (C) show the individual applications that are required to completed the process flow, with mask patterns (a, d, g), etches (b, e, h) and mask removals (c, f, i) shown. [6]*

Chapter 2

Method

Materials and analysis methods are described in this chapter with relevance to state-of-the-art plasma etch processes. Key measurement terminologies are defined, and plasma etch hardware and process regimes are described. Methods for process recipe development and optimisation are discussed.

2.1 Materials

Plasma micromachining at its most fundamental level aims to create micro- and nano-scale devices. In order to achieve this, material is etched in a plasma chamber to create the correct shape for the intended use. The material inserted into the chamber is typically silicon, and in the form of a wafer [103, 152], as can be seen on the left of Figure 2.1. Wafer is the term used to refer to the disc of material to be etched, and its dimensions are standardised by an organisation called SEMI [153] so that the semiconductor industry is aligned, and machines are compatible with each other in a production environment.

The details of both the hardware and process of etching will be expanded on in this chapter. Put simply, the wafer is placed in a controlled environment and a chemical reaction between the plasma and the wafer removes the required material [15-18, 154]. This effect occurs indiscriminately across the whole wafer, so to form a desired shape some areas of the wafer are covered with a protective coat. This is referred to as a 'mask pattern' and is usually Photoresist (PR, organic-based polymer) or some form of Hardmask (e.g. Silicon Oxide (SiO2, oxide), Silicon Nitride (SiN), metal masks, etc.) [155]. Choice of mask material depends on several factors, including material to be etched and the intended application; most of the work completed in this development utilises a PR mask due to its advantages in ease of application, as it requires no other plasma processing. An image of a silicon wafer with a PR mask on the surface can be seen on the right of Figure 2.1.

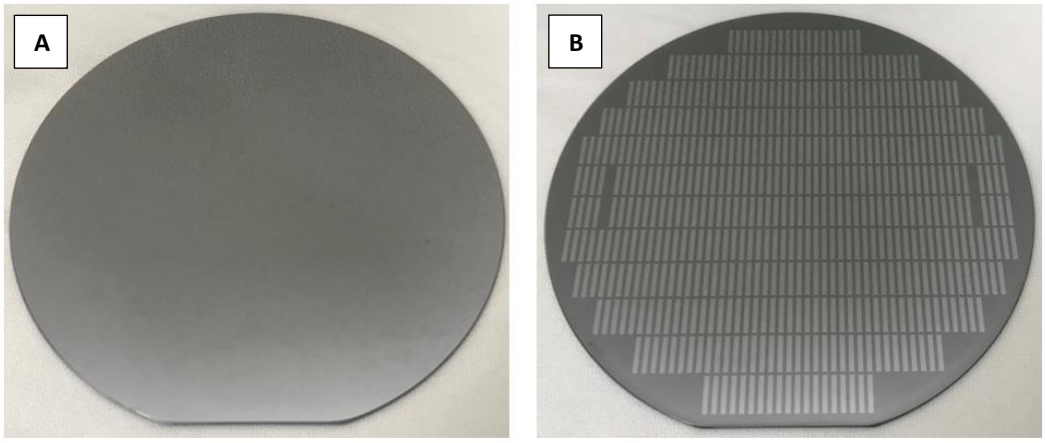

Figure 2.1. *100mm silicon wafers. (A) Bare Si with no mask coating. (B) Silicon wafer with PR mask applied to surface. Masking steps performed by Olivia Howells at Swansea University.*

The photoresist and the developer fluid were purchased from Microchemicals GmbH, and silicon wafers were purchased from Si-Mat (Silicon Materials, Germany). Depending on the application PR can be 'spun' (using a rotating chuck to spread PR onto the wafer), or 'sprayed' (a movable nozzle uniformly coats the top wafer surface). If sprayed, a SUSS MicroTec AS8 is used to deposit AZnLof2070 PR onto the wafer. If spun, AZ125 NXT PR is applied using a Laurell WS-650 spin coater. To harden the PR in the correct areas a SUSS MicroTec MA8 UV aligner was used to expose the mask pattern, before the wafers were washed in AZ276 developer to remove excess resist from opened areas.

2.2 Plasma Etching Basics

One of the four fundamental states of matter, plasma is a fluidic state characterised by the presence of free electrons in an ionic gas with equal numbers of positive and negative charges [156, 157]. Plasma makes up most of the visible matter in the universe [156, 157], and some examples of naturally occurring plasma include Stars, Lightening, and the Aurora Borealis [156]. 'Artificial' plasmas can be created by the excitation of gas in a vacuum

chamber, using an electric field to excite and strip electrons from the gaseous atoms leaving a sea of free electrons and ions [156].

Plasmas can be reactive when produced in the correct environment. Plasma etching aims to harness this reactive element, and focus it onto the wafer surface. Any area of the wafer which is not masked chemically reacts with the plasma, causing material to be removed [154]. This is desirable to create three-dimensional (3D) structures in the wafer, defined by the mask pattern and designed to achieve the required dimensions. These applications can be anything from photonics to microelectromechanical devices (MEMs), and span a wide range of materials, but the basic principle remains the same and this method of etching is referred to as 'Reactive Ion Etching' (RIE) [16, 158, 159].

Plasma is created for RIE in a confined and pressure-controlled chamber. Gasses enter the chamber and are excited to the plasma state by an electromagnetic field generated around the chamber at a frequency of 13.56MHz (RF) [160]. This method of plasma generation is known as Inductively Coupled Plasma (ICP). The aim of ICP-RIE is to remove material from the wafer surface by the presence of a reactive plasma, with the by-products being removed from the chamber [15]. For silicon, this is typically achieved by using a fluorinated gas to generate Fluorine (F) free radicals in the plasma which react with the silicon to give Silicon Tetrafluoride (SiF_4) which is then pumped away through an exhaust in the chamber [17, 18, 154].

Plasma etching is a type of 'dry etching', so named for the absence of wet chemicals used to process wafers [16, 159]. An alternative form of etching uses reactive chemicals, usually acids, and is referred to as 'wet etching'. A typical wet etch station has a much larger footprint and requires a significantly larger facility to not only process wafers, but to adequately clean them to prevent unwanted etching [21, 27, 161]. Additionally, wet etch chemicals are often extremely hazardous, and as such there are significant and rigorous

safety procedures that must be followed to prevent harm befalling any engineers or operators charged with the use of Potassium Hydroxide (KOH) or Hydrofluoric Acid (HF) [111, 112]. Wet etching results in isotropic or crystal oriented etch forms which can be hard to control [18]. The avoidance of these dangers and the ease of anisotropic etching are the main benefits of using plasma etch technologies [18].

Types of plasma etching can usually be described by one of three terms; Chemical, Physical, or Combined etching [16, 154]. Chemical etching relies on the reactions of the plasma constituents with the surface of the substrate, removing material by the reaction between the free radicals in the plasma and the wafer. Physical etching uses a RF generator beneath the wafer to accelerate the ions present in the plasma to the wafer surface, removing material by sputtering. As the name suggests, Combined etching utilises both the effects of chemical and physical etching, combining the reactive and sputtering elements to achieve a more efficient and controllable process.

In order to etch the correct areas of a wafer to produce a desired device, a mask pattern is applied to the wafer surface. PR is used to cover the wafer where the silicon substrate needs to be protected, and the PR is opened to expose the substrate in the specific areas to be etched. A basic schematic for patterning and etching steps is shown in Figure 2.2. Processing starts at step 1 with a bare wafer before a layer of mask material (blue) is applied as in step 2. The master mask pattern (red) for the intended application is placed over the wafer as shown in step 3. The wafer is exposed to UV as in step 4, which cures the required areas of the mask. In step 5, the master mask pattern is removed and the wafer is soaked in developer before the excess PR is removed in step 6. Step 7 shows the exposed areas of the wafer being etched, and when this is completed the remaining mask is removed, leaving the result shown in step 8.

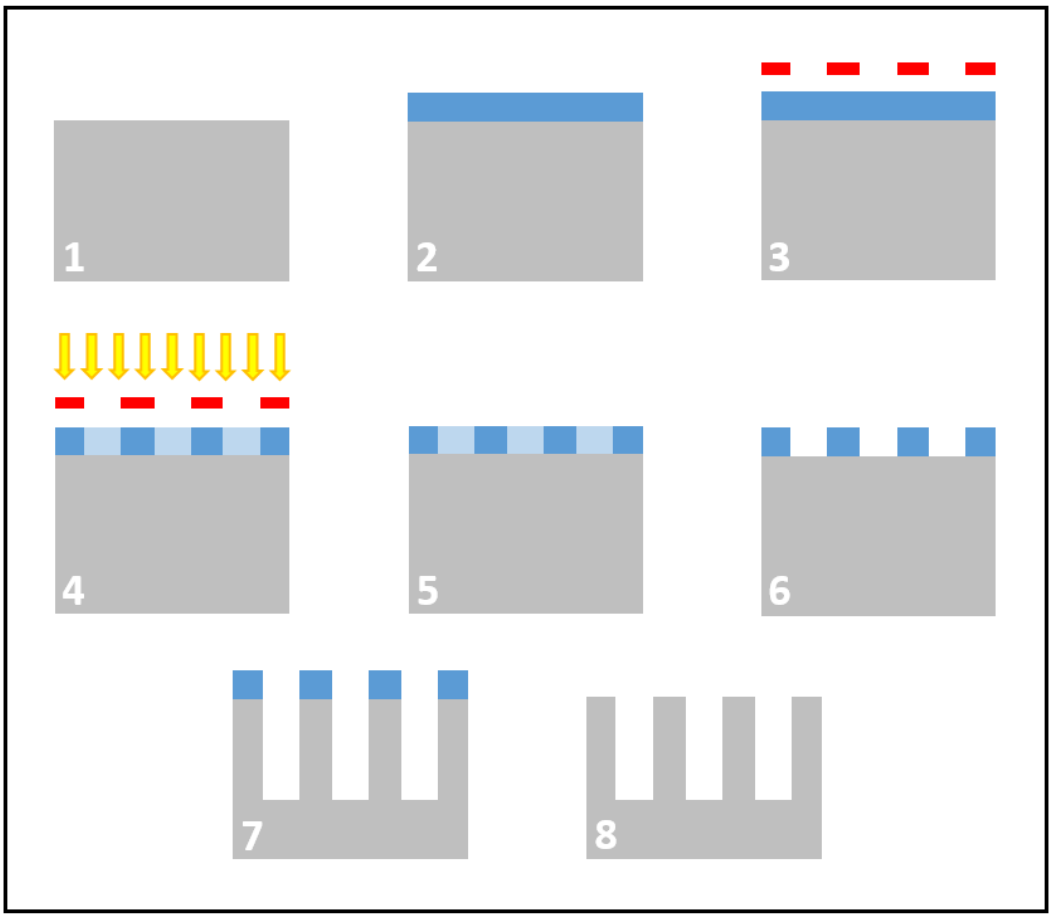

Figure 2.2. *Illustration of generalised PR masking/etching steps. In step (1) the wafer is shown in grey, with the PR represented with blue in step (2). The master mask pattern is shown in (3) in red, with UV rays symbolised by the yellow arrows in step (4). The light blue areas of the mask in (4) and (5) have been exposed to the UV and so can be washed away in developer leaving the mask pattern as in (6). Step (7) shows the etching of the features, with (8) being the final result after the removal of the remaining PR mask.*

Semiconductor devices are designed in three dimensions. The mask pattern defines the plan view of the device, and controlling the etch is key to achieving the correct shape of the final product. The most common targets for etching are Depth and Profile as these have the largest effect on the shape, with other targets mostly focussing on the quality of the etch rather than the shape.

2.3 Process Terminology & Definitions

In order to characterise etched features, process results are examined under a Scanning Electron Microscope (SEM). Using a cleaved cross-section of the etched wafer piece, measurements were made using the integrated metrology software available on the Zeiss Sigma SEM [162]. These can then either be used directly or combined to give other parameters. Below is a list of common measured or calculated parameters, including their definitions and formula (if applicable), and the measurement positions are illustrated in Figure 2.3.

Depth: Straight-line height measurement from the bottom of the mask to the bottom of the etched feature.

Critical Dimension (CD): Straight-line width measurement of the feature. Position of measurement in the etched feature is specified, with most common used being Top CD (width of etched feature at mask interface) and Bottom CD (width of etched feature at the base).

Etch Rate (ER): Calculated by dividing the Depth by the time of the process, given in µm/min.

Non-Uniformity: Quoted in form $\pm\, x\ \%$, a measure of variation of a parameter across a wafer. Calculated by dividing the Median by the Mean using the formula

$$\text{Non-Uniformity} = \frac{\max - \min}{2 \times \text{avg}} \times 100 \tag{1}$$

and used most frequently for depth. A low non-uniformity figure is desirable, as it shows consistency of results across a wafer.

Profile: The angle of the etched sidewall in degrees, relative to the horizontal. Inconsistent angle measurements are possible with SEM because of the scanning and imaging/measurement errors, therefore Profile is calculated using the Top and Bottom CD's (CD_T and CD_B respectively) in combination with the Depth by the formula

$$\text{Profile} = 90 + \tan^{-1}\left(\frac{CD_B - CD_T}{2 \times \text{Depth}}\right) \quad (2)$$

Undercut: Lateral distance between the mask sidewall and etch sidewall.

Mask Thickness: Vertical height of the mask as measured, pre- and post-etch.

Selectivity: Ratio of material etch depth to mask etch depth. Unit-less, selectivity is a useful metric to assess the process regime space, or to calculate how deep one can go with a given pre-etch mask thickness. Calculated with the formula

$$\text{Selectivity} = \frac{\text{Etch Depth}}{\text{Mask}_{\text{Pre}} - \text{Mask}_{\text{Post}}} \quad (3)$$

and usually shown in the form of a ratio (e.g. 10:1 Si:PR, indicating that 10µm of silicon is etched for every 1µm of mask).

Passivation: Deposition from the process that remains present on the feature sidewall. Small amounts are desirable to protect the sidewall, but too much or too little can induce damage from unintended etching in the sidewall.

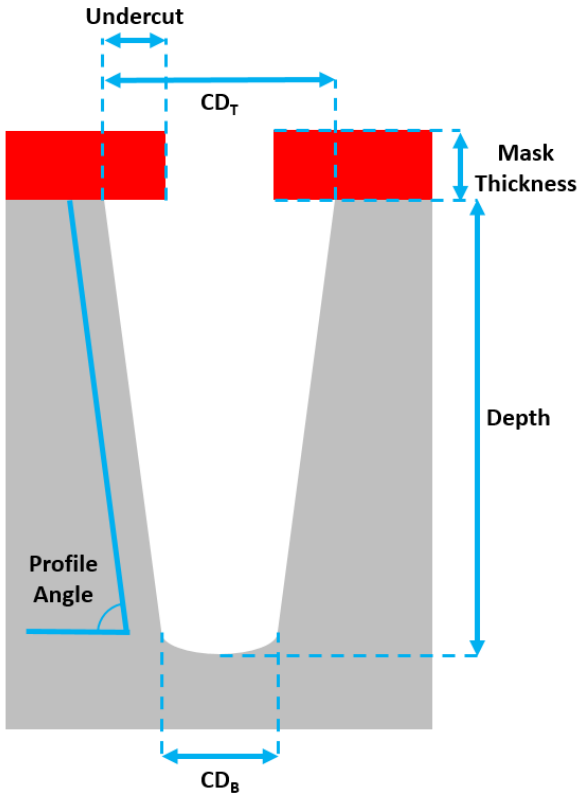

Figure 2.3. *Illustration of the common measurements made of an etched feature. Profile Angle is measured in degrees from horizontal, with the other measurements being taken in micrometres. CD_T and CD_B are the feature widths at the top and bottom respectively, also known as Critical Dimensions.*

2.4 Plasma Etch Tool Hardware

2.4.1 Basic Machine Setup

A simplified cross section of a typical etch system is shown in Figure 2.4. A wafer is placed on a platen inside the vacuum and process gas enters via an inlet, with an exhaust leading to a vacuum pump to maintain the low chamber pressure. The chamber is surrounded by an electromagnetic RF coil to excite the gas to plasma, and in many cases, there is a second RF source connected to the platen itself to accelerate ions toward the wafer, known as Bias [18].

The hardware above is enough to perform RIE on a silicon wafer with the correct gas/power inputs, however the process control afforded by this setup is limited.

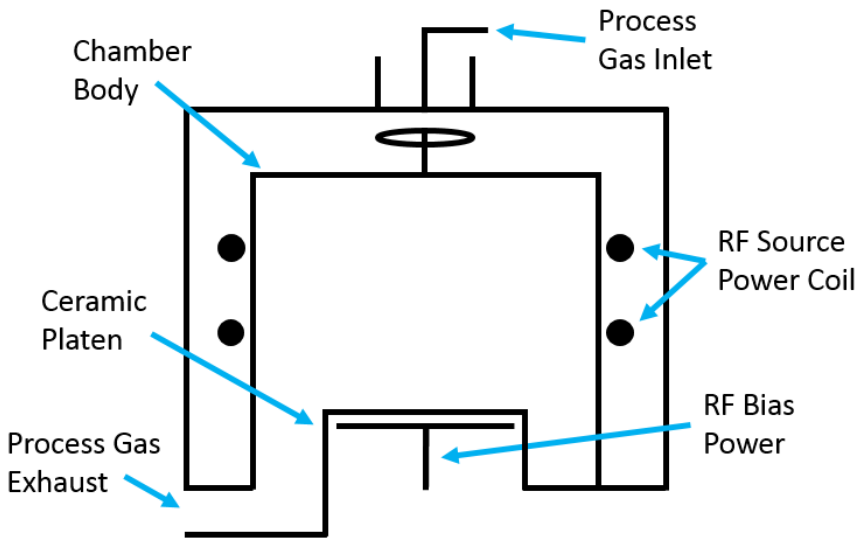

Figure 2.4. *Conceptual cross-section of a generic ICP-RIE chamber for plasma etching. Key design elements are highlighted.*

2.4.2 SPTS Deep-Reactive Ion Etch (DRIE) Machines

In addition to the model above, the SPTS systems utilise additional design features to aid the control of the etch process. An APC (Automatic Pressure Control) valve sits between the chamber and the vacuum pump, allowing fine control of the pressure during process. Plasma etching also increases the temperature of the wafer, with both the exothermic chemical reactions and radiative heat from the plasma having an effect. To counter this, the platen is cooled by an internal liquid flow to evacuate heat from the wafer. To ensure good thermal contact between the wafer and platen, the platen contains an electrode to electrostatically clamp the silicon substrate to the surface. Additionally, helium gas is flowed to the backside of the wafer to aid in increasing the thermal contact and conductive heat transport.

The tools available for this development, the Rapier™ and the DSi-v™, are both produced by SPTS Technologies Ltd and are considered Deep Reactive Ion Etching (DRIE) machines [17, 163]. While both module types derived from the same previous module and are designed for deep silicon etching, containing all the elements mentioned above, their hardware differs to give advantages in specific areas:

Rapier™: 'Dual Source', contains two regions of plasma generation – Source 1, a bell jar at the top of the chamber; and Source 2, a wider area around the chamber body. By controlling the Source 1+2 RF powers and gas flows, it is possible to alter the spatial etching characteristics and maintain a better non-uniformity compared to a single source tool. Desirable for sensitive applications such as small vias and trenches with the need for good profile or tilt [164].

DSi-v™: 'Reduced Volume', the internal volume of the module is smaller than others, including the Rapier™, so the vacuum pump is more effective at removing by-products from the chamber and the APC can more efficiently achieve a demand pressure. Etch steps are more effective and this usually results in a higher etch rate with fewer micromasking events, desirable for high open area applications [164].

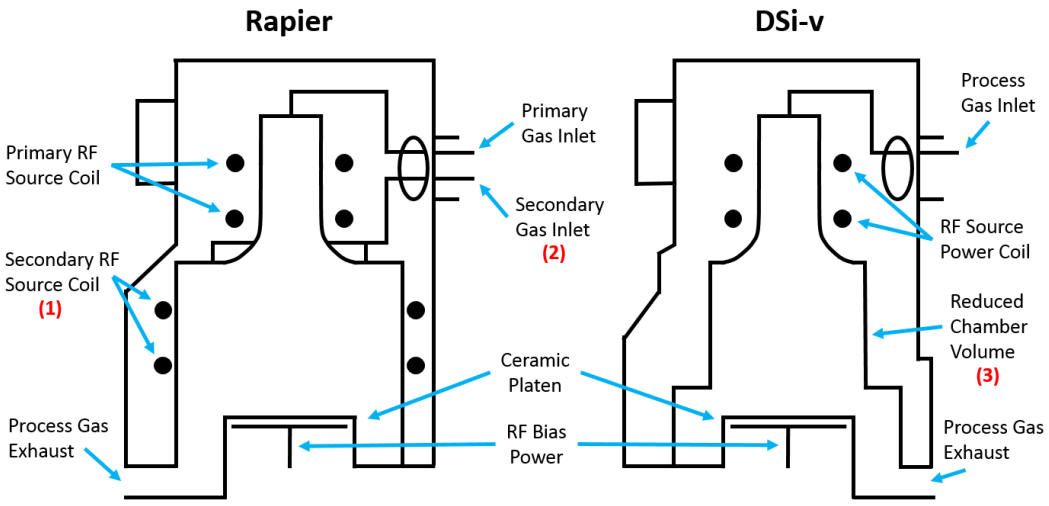

Figure 2.5. *Conceptual cross-sections of SPTS Technologies Ltd Rapier™ and DSi-v™ DRIE chambers. Key hardware is highlighted, with the main difference between the chambers being the presence of a secondary RF (1) and gas inlet (2) on the Rapier™, and the reduced chamber volume (3) of the DSi-v™.*

2.5 Plasma Etch Regimes

2.5.1 Plasma Formation

To form a plasma capable of etching, a starting gas is selected that will be reactive with the target substrate. For silicon this is commonly Sulphur Hexafluoride (SF_6), though any fluorinated gas would also be sufficiently reactive with the wafer surface.

Generation of the reactive plasma is achieved by the excitation of the input gas by a RF coil around the chamber providing electromagnetic energy to the chamber contents. This excitation causes the dissociation of SF_6 via the mechanism [165]

$$SF_x + e^- \rightarrow SF_{x-1} + F + e^-. \quad (4)$$

Ionisation of the SF_6 is also possible by the interactions

$$SF_6 + e^- \rightarrow SF_5^+ + F + 2e^- \quad (5)$$

and

$$SF_6 + e^- \rightarrow SF_6^-. \quad (6)$$

This gives the plasma etch its physical component, by providing charged particles that can be accelerated towards the wafer surface by the RF power applied beneath the substrate.

2.5.2 Plasma Interaction with Substrates

Free fluorine radicals are reactive with the silicon substrate, and etch the surface most commonly via the mechanism

$$4F + Si \rightarrow SiF_4, \quad (7)$$

where SiF_4 is a volatile gaseous by-product that desorbs form the wafer surface and can be pumped away [154]. This reaction provides the chemical component for etching.

If required, plasma can be used to deposit material onto the wafer. Typically this is achieved by using Octafluorocyclobutane (C_4F_8) gas in the chamber. Under the conditions in the chamber, multiple products are created from C_4F_8, including C_4F_8, CF_4, and C_2F_6 along with other products and their various states of ionisation. The deposition effect is achieved by the reaction

$$C_nF_k^- + C_4F_8 \rightarrow C_{n+4}F_{k+8} + e^- \quad (8)$$

which forms chain polymers that gather on the wafer surface [159, 166]. This effect in plasma processing is commonly referred to as deposition or passivation and this term is not specific to C_4F_8. The terms refer to the act of coating the wafer with a protective layer during the plasma process, though this is most commonly achieved with C_4F_8 for silicon etch processing.

2.5.3 Non-switched Plasma Etch Regime

Non-switched is the term used for a method of plasma processing where the recipe (the total collection of process parameters) is written in one step. In their simplest forms, Non-switched processes comprise of a single step run for a fixed time with static parameters, although it is possible to either alter parameter values over the course of a step or have successive steps with differing parameters. In general, a recipe can be called non-switched if the steps are relatively long and don't repeat (AKA loop) throughout the process. As the steps don't explicitly interact, if multiple steps are present in a process they must each function as a standalone process, combining the etch gasses and any necessary passivants all in one, meaning that a balance must be struck to achieve the required etch. Directionality of the etch is very hard to control in these conditions, so the resulting etch shape usually presents as pseudo-isotropic with a significant lateral etch component [19]. A typical non-switched etch shape is shown in Figure 2.6.

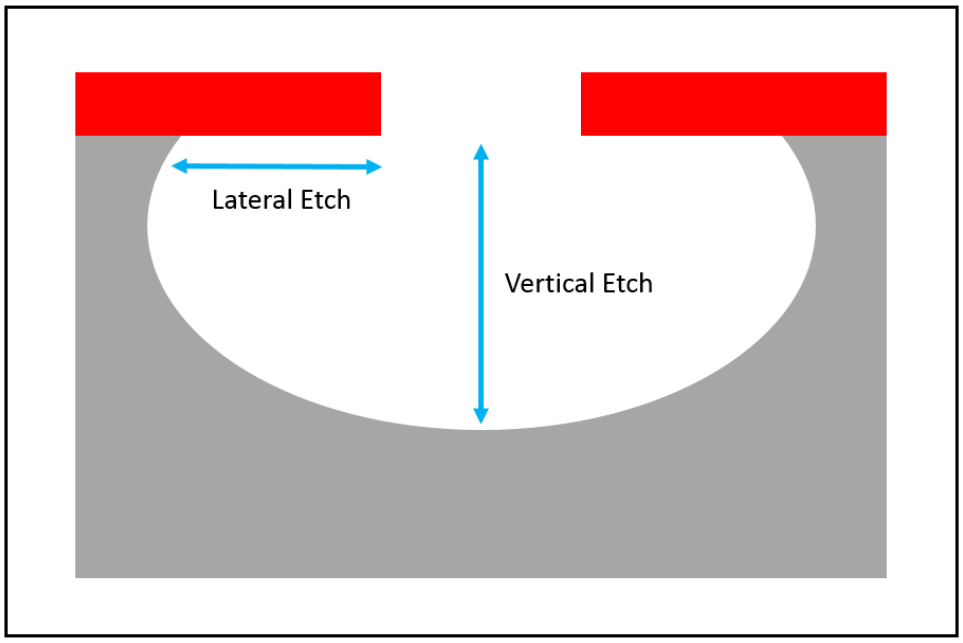

Figure 2.6. *Illustration of a typical single step etch shape. The combination of etching and passivation gasses in a non-switched regime results in a process where the directionality is hard to control, leading to a pseudo-isotropic etch shape.*

2.5.4 Switched Plasma Etch Regime

Switched processing consists of two or more steps of a recipe which are completed one after the other. Once the final step is over, a 'loop' is complete; the process then returns to the first step. The recipe terminates after a predetermined number of loops. The looped regime allows the separation of etching and deposition steps. Deposition is laid down to protect the sidewalls of the etched feature, while the etch step(s) are used to selectively remove the deposition from the feature base and etch the silicon beneath. Switched plasma etch regimes combine repeated isotropic etches with protective deposition steps to form highly anisotropic etch features [15, 16, 154].

The classical two step regime is commonly known as the Bosch Process [18, 167], though more modern iterations of this looped regime have yielded a 3-step version.

2-Step "Bosch" Process: Consists of a deposition step and an etch step. The etch step must balance the directional etch needs of removing the base deposition and chemical requirement to etch the silicon. Illustrated graphically in Figure 2.7.

3-Step Process: Usually consists of a deposition step, a physical etch step, and a chemical etch step. The separation of the physical and chemical etch elements allow more controlled tuning of the process and results. Illustrated graphically in Figure 2.8.

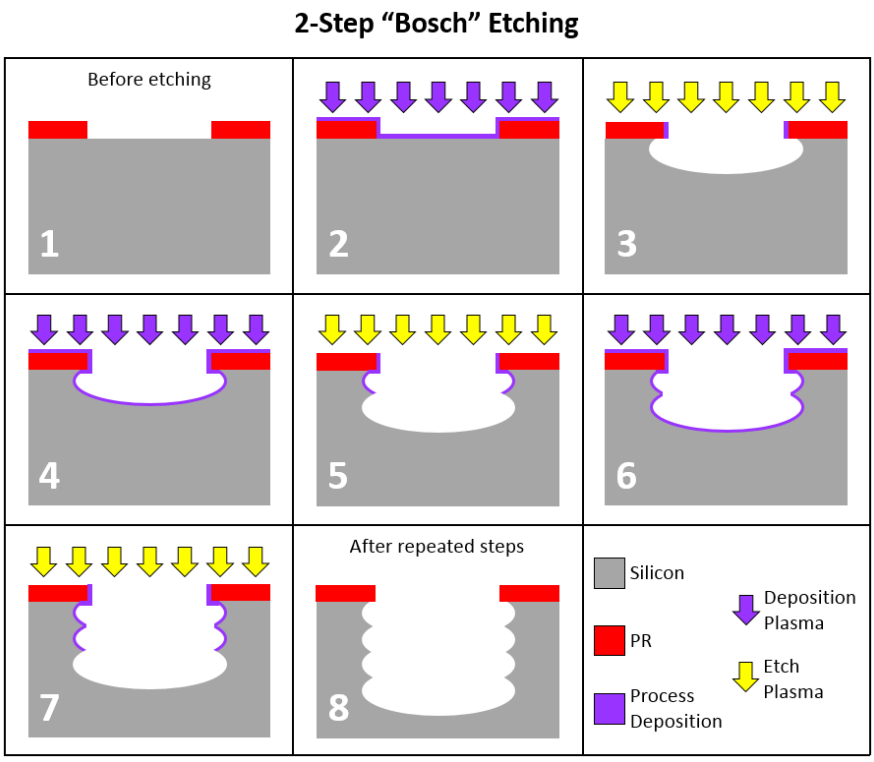

Figure 2.7. *Illustration of the step progression in a 2-step Bosch regime. Panel (1) shows the masked wafer before processing, deposition (2, 4, 6) is then laid down to protect the side of the feature from the isotropic etch steps (3, 5, 7). After repeated alternating steps, an anisotropic etch form is achieved as shown in panel (8). The etch step is used to both clear the deposition from the base and etch the Silicon beneath.*

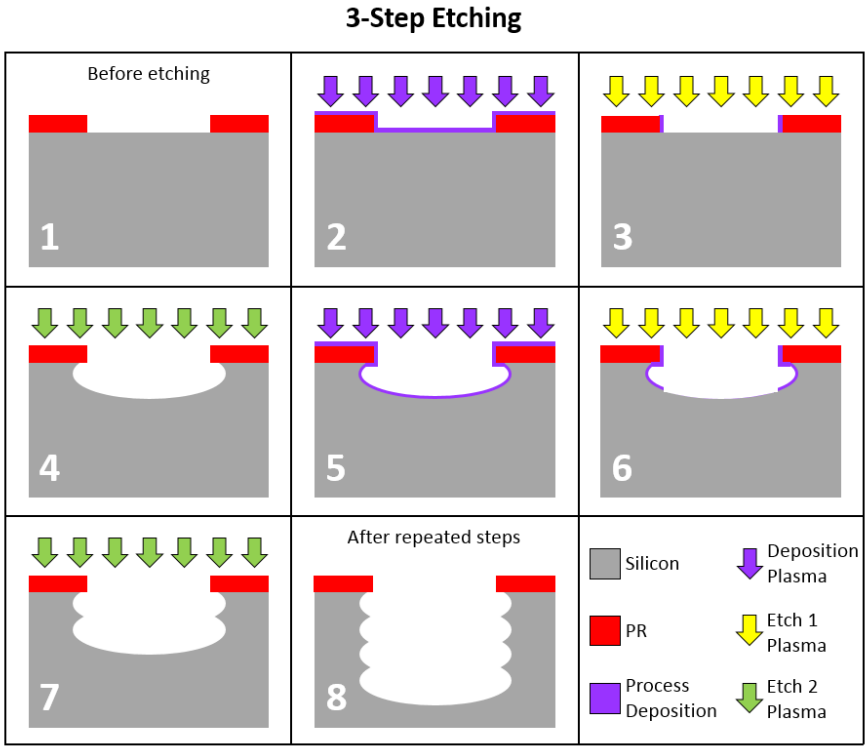

Figure 2.8. *Illustration of the step progression in a 3-step regime. Panel (1) shows a masked wafer before processing. Deposition (2, 5) is laid down to protect the feature before the physical Etch 1 (3, 6) step clears the deposition from the base, allowing the chemical Etch 2 (4, 7) to isotropically etch the silicon. After repeated steps, an anisotropic etch is formed as shown in panel (8). The separated Etch 1 and Etch 2 steps mean that the removal of the deposition and the etching of the silicon can be tuned separately. [6]*

2.6 Basics of Analyis and Process Development

2.6.1 Analysis Methods

In order to analyse etched features, two primary methods of analysis were employed. Optical imaging provided a non-destructive top-down view of the wafer, good for assessing the incoming quality of wafer surfaces and scanning etched features for defects. Optical images were taken using a Leica DM12000 [168] or Olympus MX50 [169] optical microscope.

Detailed cross-sectional analysis were completed using a Zeiss Sigma Scanning Electron Microscope (SEM) [162]. In a SEM, a beam of electrons is emitted from the ‘electron gun’

towards the sample. After random scattering from interaction with the sample, the electrons are detected and an image can be formed from their energies. A basic schematic of a SEM can be seen in Figure 2.9.

Features were viewed side-on in order to properly characterise depth, CDs, undercut, and mask thickness. To facilitate this, features were cleaved through vertically by using a diamond scribe to break the wafer along the Si crystal plane. Wafer pieces were then placed in a Zeiss Sigma SEM for analysis, using the integrated metrology capabilities to measure the etched features.

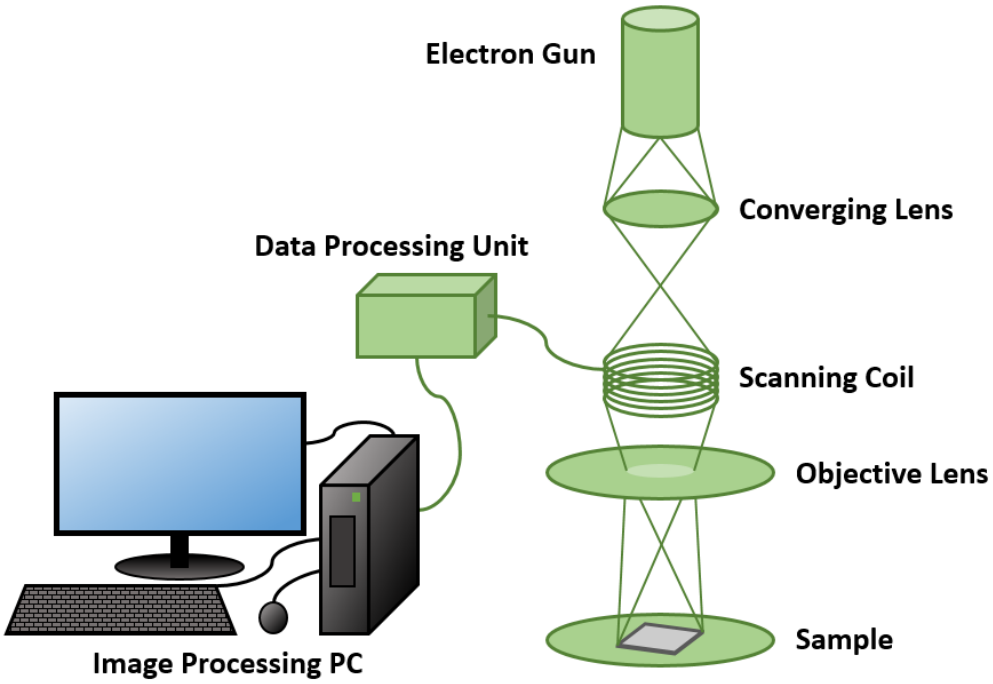

Figure 2.9. *Schematic of SEM analysis of a sample. [1]*

2.6.2 Process Recipe Development

With an abundance of material and consistency of methodology, a 'Design of Experiments' (DOE) [170] can be completed. This method of process development attempts to model the best possible process results by changing a few key parameters and measuring

the etch results. As different process changes often affect the same measured result, e.g. both source RF power and chamber pressure affect the etch rate, the interactions of the process parameters must also be studied. Specialist modelling software can then map the results of changes and interactions between parameters, and interpolate the data to provide a 'best process' which can then be tested to see if it aligns with the expected result. While this method is time efficient, as all necessary tests can be processed together before analysis, as mentioned above it requires a significant amount of material to produce the results. As such, the DOE is usually reserved for larger companies with the budgets to support this development type.

Trial and error is a standard method for process development but this requires a high level of experience to achieve good results in the fewest possible tests. This was the primary method employed for the optimisations in this work, to maximize the learning and development possibilities from the available material.

Chapter 3

Design, Process Flow, and Bevel Etch Development

This chapter will describe the overall design of the hollow microneedle and the fabrication process steps in detail. The development of the first dry etch step, the bevel etch will then be explained, including optimisation methodology and results.

3.1 Introduction to Bevel Etch

Other examples of silicon microneedles, both hollow and solid, have been developed in the past. In general, the fabrication process for the bevel is either a form of wet etching involving Potassium Hydroxide (KOH) [75, 110, 140, 144] or Hydroflouric Acid (HF) [14, 74], or a plasma etch in a process flow that results in an unconventional needle shape [9, 73, 74, 145]. In both cases, significant disadvantages exist.

For wet etching, this disadvantage is that the chemicals required to perform the step. The handling of KOH and HF require exhaustive training and Personal Protective Equipment (PPE) measures in order to be used with any degree of safety [111, 112], and indeed even with appropriate measures in place, risk associated with wet chemicals cannot be avoided. Significant advantages in wet processing exist in the initial tool cost and low non-uniformity as it is a predicatable chemical reaction that follows the crystal plane of the wafer, and as such it is repeatable across and consistent between wafers meaning that the increased risk is often considered acceptable. Typically wet etching also requires that a whole area of a production facility has to be dedicated to this one step - in practice, a large footprint is required to safely complete the etching step as well as wafer cleaning to prepare for further production steps. It is therefore of beneficial to both the health and safety of factory personnel and to the optimisation of facility space to perform this step on a dry plasma etch system, as the safety risks are significantly reduced and the smaller footprint of the machine allows more floor space to be used for additional processing machinery. In addition KOH etching of Si results in a fixed, continuous angle [22]; this has negative effects for MN use, in particular the ease of MN skin penetration where shallower angles are more beneficial [73] – a fixed, shallow angle takes up too much height of the MN, so a curved shape is preferable to provide an angle that aids with insertion while not using too much of the total MN height.

Another advantage is the ease with which microneedle length can be increased without impacting the mask design requirements. Where the angled surface is completed with dry etching in other process flows, the disadvantages lie with the microneedles rather than their manufacture. In other process flows, the overall design of production flow and needles limit the final shapes that can be produced, resulting in microneedles that are either unfamiliar or require special instructions to use [14, 20, 74, 144].

In this work, a recognisable needle shape is fabricated for the microneedle that is intuitive to use. The first challenge in producing this shape is the curved bevel that is immediately familiar from hypodermic needles, which serves the purpose of reducing the tip angle and facilitating penetration of the needle into skin with low force [73, 151] and minimising the training required for safe use. Other challenges such as maintaining a uniform etch depth on a wafer with a high open area of silicon are discussed in length later in Section 3.3.2.

3.2 Bevel Etch Method and Metrology

3.2.1 Wafer Preparation and Photolithography

As this is the first step in the sequence, the wafers do not have topography and the polished surfaces are ready to be patterned for the bevel etch step. Lithography steps were completed at Swansea University by Olivia Howells.

Due to the flat surface, spin coating PR provides a conformal coating suitable for the masking of this etch step. Negative AZ125 NXT photoresist was spun onto the wafers using a Laurell WS-650 spin coater, before being baked on a hotplate set at 130°C for 10 minutes to harden the PR. The wafers were then allowed to cool, before being transferred to a SUSS MicroTec MA8 for UV exposure of the pattern. When washed in AZ726 developer, the photoresist exposed to UV remains in place, while any portions of the PR that were not

exposed dissolve. De-Ionised (DI) water was used to remove excess developer and the wafers were left to dry before use in the production flow.

100mm device wafers were bonded to a 150mm carrier wafer for etching in the SPTS process module. This was achieved using Crystalbond 555-HMP adhesive, which has a thermal flow point of 66°C and allows the device wafer to be mounted onto the carrier using only a hotplate. Once cooled, the wafers are firmly bonded until more heat is applied to separate them.

3.2.2 Etch Targets

In order to penetrate the *stratum corneum* effectively with low forces, the needle must have a sharp tip [73, 151]. Practically this translates to a requirement for a curved shape for the bevel etch, to provide the sharp tip while also not using too much of the total MN height for the top surface so that vertical height and insertion depth can be controlled by a subsequent etch. In terms of quantifiable results, the aim is to produce a needle tip with peak angle 15-30° that curves down to the feature base; it must extend at least 300µm horizontally across the wafer surface to accommodate the full microneedle width. No specific depth target is set as the height of the MN is controlled with a later step. The primary concerns for the bevel etch are peak angle and MN width.

3.2.3 Metrology and Analysis

Primary analysis of bevel etch runs was carried out using cross-sectional SEM imaging. Wafers were cleaved along the Si crystal structure using a diamond-tipped scribe and placed in the SEM, measurements were then taken of the cleaved face using the integrated metrology capabilities of the Zeiss SEMs, providing quantitative results. Top-down optical inspections were also carried out to assess general surface quality, though no measurements

of significance can be taken in this manner so it is purely qualitative analysis; in any case, top-down optical imaging is often complicated by the topography of etched wafers.

Quantitative comparisons of etched features between test runs are not possible if only etch depth is considered, as not all etches are completed to the same depth (as a specific depth is not a target for this step). For this reason, as well as the non-importance of depth etch rate, comparisons between runs were completed using the ratio of the etch depth of trench at position x divided by the maximum trench depth on that wafer. The resulting value between 0 and 1 gives the relative etch depth across the wafer, which can be used for analysis of regular etch parameters such as non-uniformity but also allows the direct comparison of etch depths at each position x between two runs that would otherwise be limited to more simplistic comparative analysis. The ratios of multiple runs can be plotted on the same axis and compared directly across the whole wafer, as if the etch depths were the same, to properly show the differences in uniformity 'shape'. This normalised parameter is referred to as the 'Depth Etch Ratio' during analysis.

3.3 Bevel Etch Development and Results

3.3.1 Etch Module and Initial Results

A SPTS Technologies Rapier™ module was selected for the etching of Si microneedles; a large number of parameters can be altered to achieve the final result as described in Chapter 2 Section 2.4.2, the presence of primary & secondary coils and gas flows provides multiple options for process alterations during development.

As the desired shape to the bevel is similar to that of an isotropic etch [19], the starting process was a single step etch with fixed, low platen RF power which allows the etch to propagate in the necessary manner. The basics of single step plasma etching are described

in Chapter 2 Section 2.5.3, and the reason for its implementation in the manufacture of the bevel is clear – the angled surface produced by the long step time and low platen power the shape desired for low insertion force of the final microneedle [73, 151].

The starting etch process parameters were determined by a combination of previous similar etches and experience working with plasma etch processing. In this case, the parameters can be seen in Table 3.1.

The initial results with this set of parameters were promising, with the desired bevel shape present across the etched wafer – the etch rate was higher than expected and no quantitative data could be obtained from the first run. In subsequent runs, etch time was decreased to allow for the collection of comparative data. The process window was also explored and the startpoint conditions varied, with pressure, source powers, and platen power changed to assess the effect on results. In total eleven tests were completed, but all exhibited a common problem in that the etch non-uniformity was much higher than is normally acceptable for silicon etching. The best run of the initial eleven, Run 8, included some minor modifications to the original process – the parameters can be seen in Table 3.1, and SEMs are shown in Figure 3.1. Even though the etch shape is close to the requirements laid out before the development began, the non-uniformity for all runs was high and it required further investigation.

Parameter (Units)	Run 1	Run 8
{ REDACTED }		

Table 3.1. *Rapier™ process parameters from the startpoint (Run 1) and the best of the initial eleven development runs (Run 8).*

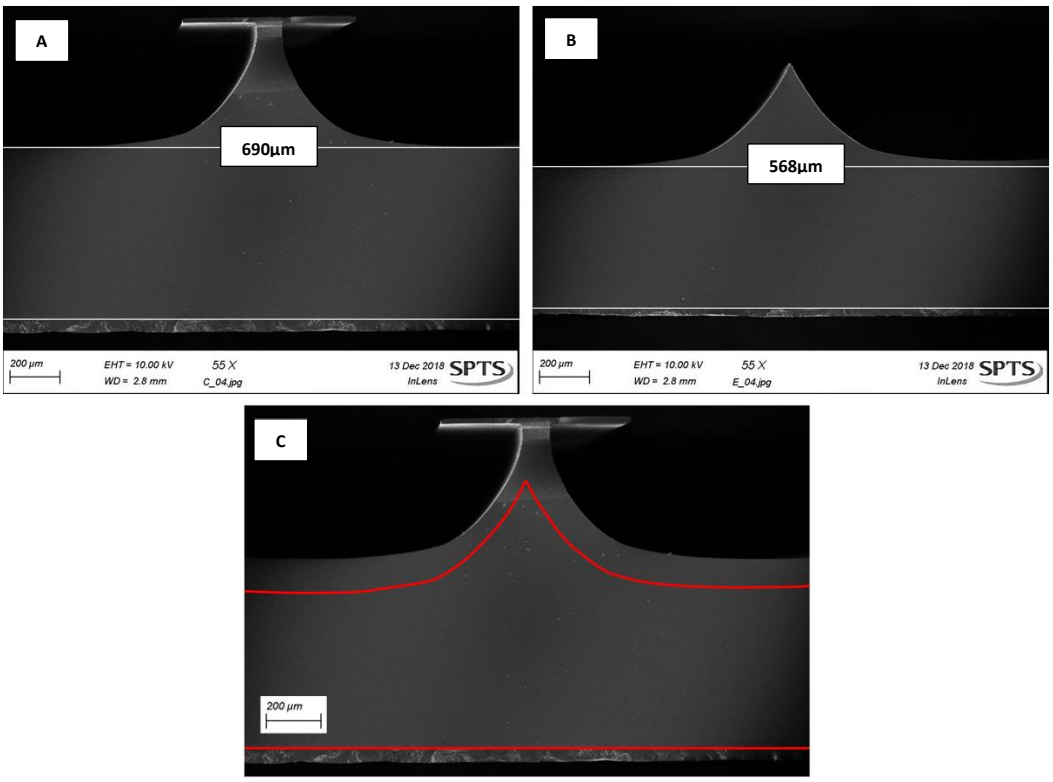

Figure 3.1. *SEM images of the centre (A) and edge (B) trenches from the best result of the initial eleven process tests, Run 8. Remaining Si thickness was measured using the SEM software as the Si under the mask at the edge has undercut completely and begun to thin the substrate. Image (C) shows an overlay of the edge profile in red on top of the centre image, showing the difference in etch shape and depth.*

3.3.2 Uniformity Investigation

Optimisation of uniformity is a key factor of yield, as good uniformity means that the performance of devices at the edge of the wafer closely matches that of the devices at the centre. Plasma etch processes all have a non-uniformity figure that can be calculated and altered using hardware and process changes. A good non-uniformity for a DRIE process is generally considered to be <±5%. For the baseline run of this development the non-uniformity was calculated at ±11.3%; although the etch result provides the correct shape, the magnitude of the depth non-uniformity implies that there is hardware and process development needed to improve the bevel etch step.

In the bevel etch case, the mechanism for high non-uniformity was unknown at the beginning of the work. It was hypothesized that the non-uniformity of the etch depth is adversely and significantly affected by the lack of open silicon within a certain radius of the feature being analysed, known as 'local open area'. In areas where more of the wafer surface is covered with PR, and abundance of fluorine radicals is available to etch the open silicon compared to areas where more silicon is open with the same amount of fluorine. This increases the etch rate in the more patterned areas of the wafer, in practice for the bevel etch this is the wafer edge. This was due to the sudden stop on the wafer pattern, which led to a very low open area and abundance of fluorine radicals to etch a relatively small amount of silicon.

To test the local open area hypothesis, one patterned wafer was partially taped (Figure 3.2) to cover a section of features. This moved the effect away from the edge and allowed depth and non-uniformity measurements to be made without possible interference from uncharacterised edge effects. The best process so far from the development was run on this wafer, and calculating the Depth Etch Ratio as described in Section 3.2.3, a graph of the profile can be created, as shown in Figure 3.3. Significantly, the 'taped' result had an almost

identical non-uniformity when compared with the baseline process on an ‘untaped’ wafer (±11.2% vs. ±11.3%), showing that the presence of tape does allow the effective study of local open area effects.

The shape of the graph in Figure 3.3 does show that the local open area has an effect on the etch depth, increasing the etch rate for the trenches closer to the tape indicated by the increase in Depth Etch Ratio in comparison to the baseline result. If the local loading had no effect on etch uniformity, the etch rate would not change near the tape compared to the untaped baseline. However, the effect is not as pronounced as the edge of the wafer due to several reasons, including wafer edge effects and inherent non-uniformity of the etch process; the largest contributing factor however is the difference in shape of the pattern at the extremities of the wafer. On the true wafer edge, the features conform approximately to a circle, while the tape cuts the wafer’s local open area in a straight line; this means that the area of missing pattern at the edge of the wafer can be modelled as the area where two circles overlap, and the area missing for a taped section is simply a circular segment.

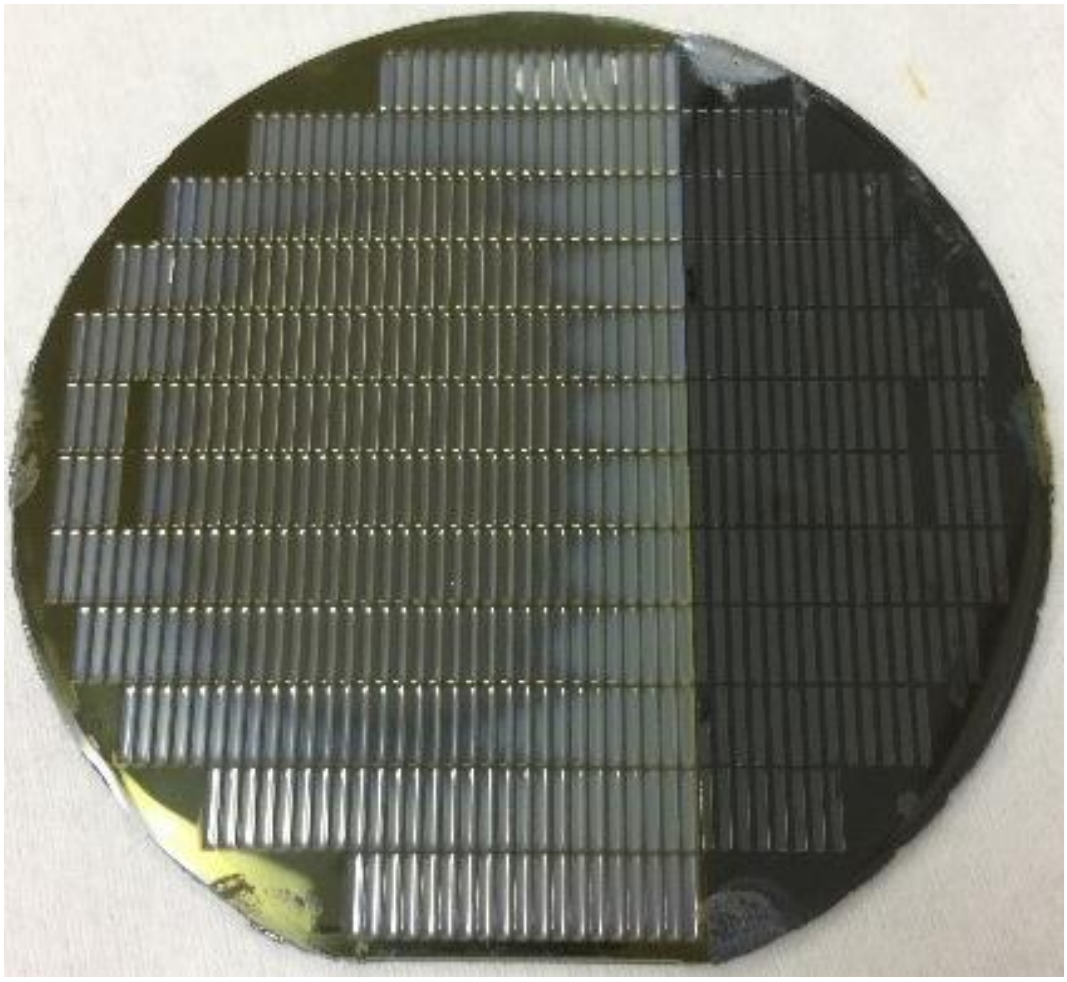

Figure 3.2. *A photograph of a wafer after process. The dark portion on the wafer's right was covered by tape to prevent etching and determine that local loading is the dominant effect on non-uniformity.*

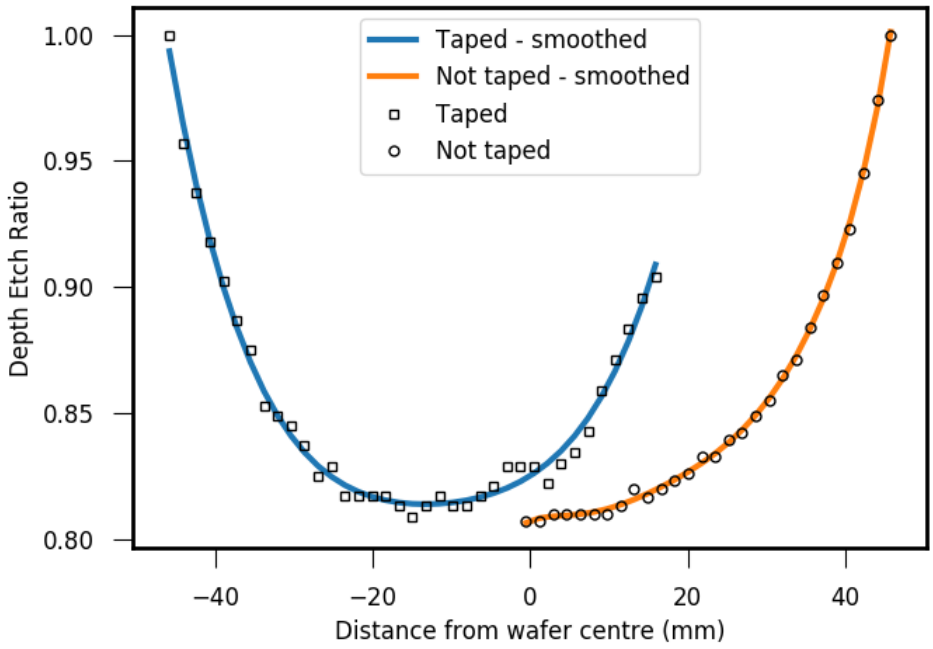

Figure 3.3. *Depth etch ratios across the taped test wafer (blue), shown with an untaped control wafer run with the same process (orange). Half of the control wafer trace (orange) is shown as the etch profile is radially symmetric. The shift of the rise in depth etch ratio from the edge of the wafer (50mm) to the edge of the tape (16mm) clearly shows the effect of local loading.*

As local open area is the dominant effect on uniformity and the two are linked, it is possible to approximate the uniformity profile from the calculated local open area of features across the wafer. By calculating the open area of silicon around a target feature from the real, curved wafer edge to the straight taped edge, the asymmetric etch depth ratio can be modelled due to the difference in areas between two overlapping circles and a simple circular segment. For ease, the wafer pattern is approximated to a circle with radius r_1, and the open area affecting a given trench was assumed to be a smaller circle with radius r_2. Defining the wafer such that the middle corresponds to the Cartesian coordinates $(0,0)$ and positioning the smaller circle such that it's origin rests at $(d, 0)$, the radii can be expressed as

$$r_1^2 = x^2 + y^2, \tag{9}$$

$$r_2^2 = (d - x)^2 + y^2, \tag{10}$$

where x and y are the values for the intersection points of the two circles, shown in Figure 3.4. Rearranging (9) for y^2 and substituting into (10) gives

$$r_2^2 = (d - x)^2 + (r_1^2 - x^2), \tag{11}$$

which can be expanded and simplified to give the equation for x as

$$x = \frac{r_1^2 - r_2^2 + d^2}{2d}. \tag{12}$$

An expression for y can also be derived by substituting equation (12) into equation (9)

$$y^2 = r_1^2 - x^2 = r_1^2 - \left(\frac{r_1^2 - r_2^2 + d^2}{2d}\right)^2. \tag{13}$$

Solving for y gives the equation

$$y = \frac{1}{2d}\sqrt{4d^2 r_1^2 - (d^2 - r_2^2 + r_1^2)^2}. \tag{14}$$

This can be further factorised to form the expression

$$y = \frac{1}{2d}\sqrt{(-d - r_1 + r_2)(-d + r_1 - r_2)(-d + r_1 + r_2)(d + r_1 + r_2)}, \tag{15}$$

giving equations for x, equation (12), and y, equation (15), in terms of the radii of both circles and the horizontal distance between their centres.

To solve for the intersecting area of the two circles, the general equation for the area of a circle segment can be used

$$A = r^2 \cos^{-1}\left(\frac{h}{r}\right) - h\sqrt{r^2 - h^2}, \tag{16}$$

where A is the area of the segment, r is the radius of the circle, and h is the triangular height of the segment. The area of two overlapping circles is comprised of two circle segments with different radii and triangular heights, therefore the full area in this case is

$$A = A_1 + A_2, \tag{17}$$

with A_1 and A_2 respectively defined as

$$A_1 = r_1^2 \cos^{-1}\left(\frac{h_1}{r_1}\right) - h_1\sqrt{r_1^2 - h_1^2}, \tag{18}$$

$$A_2 = r_2^2 \cos^{-1}\left(\frac{h_2}{r_2}\right) - h_2\sqrt{r_2^2 - h_2^2}. \tag{19}$$

To solve these equations, substitutions can be made into equation (12) using the properties of the triangular heights $h_1 = x$ and $h_2 = d - x$ (Figure 3.4)

$$h_1 = \frac{r_1^2 - r_2^2 + d^2}{2d}, \tag{20}$$

$$h_2 = d - h_1 = \frac{r_2^2 - r_1^2 + d^2}{2d}. \tag{21}$$

This leaves expressions for $h_1$and h_2, meaning equations (20) and (21) can be substituted into equations (18) and (19) respectively to give

$$A_1 = r_1^2 \cos^{-1}\left(\frac{r_1^2 - r_2^2 + d^2}{2dr_1}\right) - h_1\sqrt{r_1^2 - h_1^2}, \tag{22}$$

$$A_2 = r_2^2 \cos^{-1}\left(\frac{r_2^2 - r_1^2 + d^2}{2dr_2}\right) - h_2\sqrt{r_2^2 - h_2^2}. \tag{23}$$

The last term of equation (22) can be manipulated using equation (9), rearranged to find y, and the property of the triangular height, $h_1 = x$ (Figure 3.4)

$$h_1\sqrt{r_1^2 - h_1^2} = h_1\sqrt{r_1^2 - x^2} = h_1 y. \tag{24}$$

Now using the identity $h_1 + h_2 = d$ (Figure 3.4) it can be further rearranged to give

$$h_1\sqrt{r_1^2 - h_1^2} = h_1 y = (d - h_2)y. \tag{25}$$

Similarly, the final term of equation (23) was rearranged using equation (10) and the property $h_2 = d - x$ (Figure 3.4)

$$h_2\sqrt{r_2^2 - h_2^2} = h_2\sqrt{((x-d)^2 + y^2) - h_2^2} = h_2\sqrt{(-h_2)^2 + y^2 - h_2^2}. \quad (26)$$

Expanding the brackets and simplifying leads to the expression

$$h_2\sqrt{r_2^2 - h_2^2} = h_2 y. \quad (27)$$

Substituting equations (25) and (27) back into equations (22) and (23) respectively defines the areas of each segment as

$$A_1 = r_1^2 \cos^{-1}\left(\frac{r_1^2 - r_2^2 + d^2}{2dr_1}\right) - (dy - h_2 y), \quad (28)$$

$$A_2 = r_2^2 \cos^{-1}\left(\frac{r_2^2 - r_1^2 + d^2}{2dr_2}\right) - h_2 y. \quad (29)$$

Combining and simplifying equations (28) and (29) to give the total area of overlap as defined in equation (17) gives

$$A = A_1 + A_2 = r_1^2 \cos^{-1}\left(\frac{r_1^2 - r_2^2 + d^2}{2dr_1}\right) + r_2^2 \cos^{-1}\left(\frac{r_2^2 - r_1^2 + d^2}{2dr_2}\right) - dy. \quad (30)$$

The definition of y from equation (15) can now be substituted in, which leaves the final expression for total overlap area only in terms of r_1, r_2, and d,

$$A = r_1^2 \cos^{-1}\left(\frac{r_1^2 - r_2^2 + d^2}{2dr_1}\right) + r_2^2 \cos^{-1}\left(\frac{r_2^2 - r_1^2 + d^2}{2dr_2}\right) - \frac{1}{2}\sqrt{(-d + r_1 + r_2)(-d + r_1 - r_2)(-d + r_1 + r_2)(d + r_1 + r_2)} \quad (31)$$

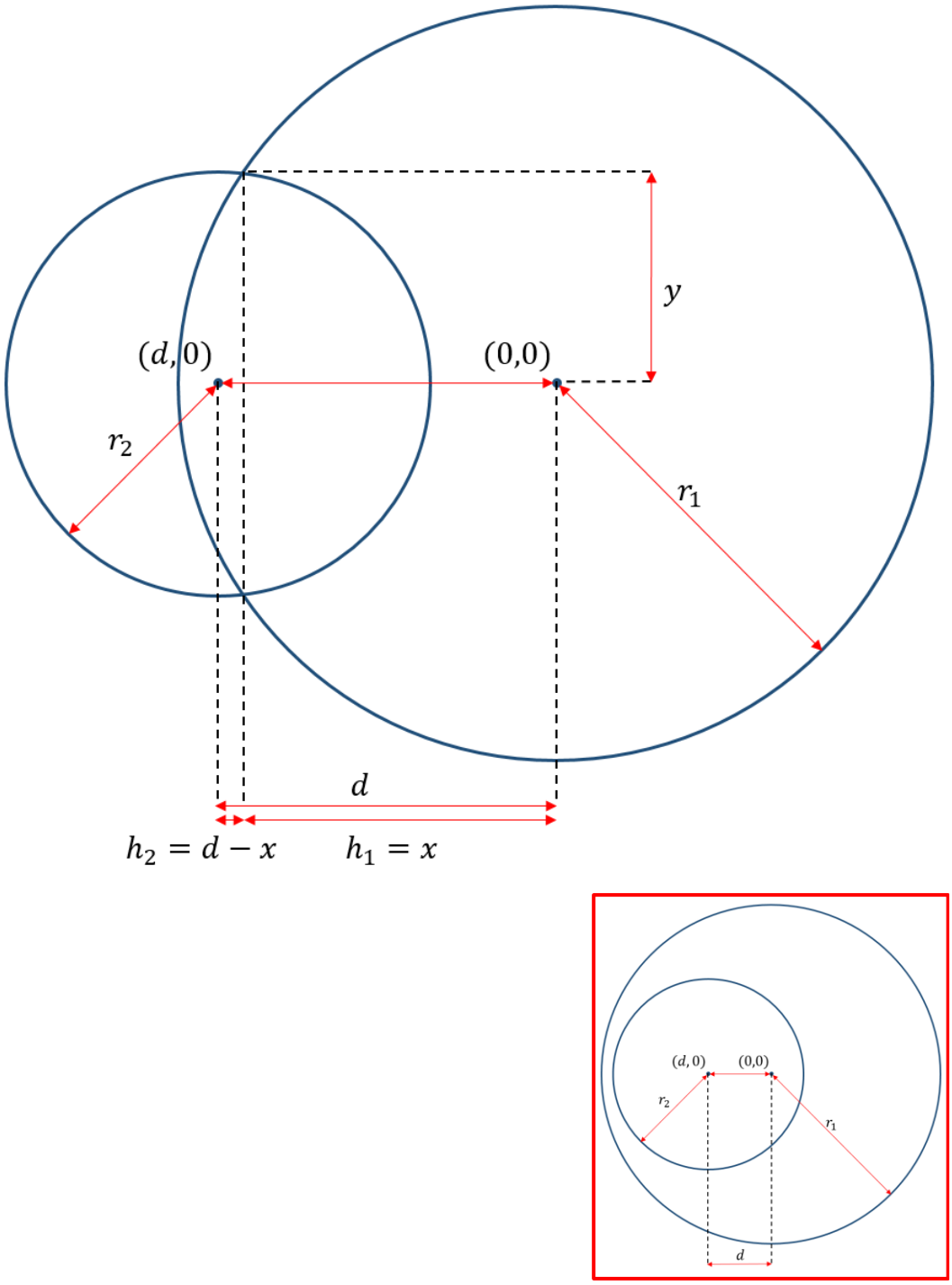

Figure 3.4. *A diagram of two overlapping circles, including centre positions in Cartesian coordinates and related variables and identities. Coordinate (d, 0) is the position of the feature for which local open area within the radius r_2 is being calculated. Length r_1 is the radius of the wafer pattern. Inset: A diagram showing an example of a feature closer to the centre, where the local open area is entirely contained within the wafer pattern.*

In the real-world case, r_1 is known and fixed due to the pattern shape. The value for d corresponds to the position of the measured feature on the x axis of the wafer, and a plotted of A versus d was acquired for a fixed value of r_2.

The missing section of the taped side of the wafer is similarly calculated, but uses the equation for a circle segment

$$A_s = \frac{r_2^2}{2}(\theta - sin\theta) \tag{32}$$

Where A_s is the area of the segment, r_2 is the radius of the circle as in Figure 3.4, and θ is the internal angle of the chord from the circle centre. The positions of the trench being analysed and the taped wafer section are known, and as θ can be expressed as a function of d through Pythagorean mathematics a plot for A_s versus d can be obtained for this side of the wafer.

A plot of A versus d of a whole wafer was found for a given r_2. In this case, the best value for r_2 was found to be approximately 20mm after plotting A versus d for $r_2 = 10, 15, 20, 25, 30\text{mm}$ and comparing to the shape obtained by the real-world case in Figure 3.3. Figure 3.5 shows the plot obtained purely by area calculations with a $r_2 = 20\text{mm}$, and visually it can be seen to have a very similar shape to the measured depths in Figure 3.3 for both the 'baseline' non-taped case, and the partially taped case. The magnitudes of the uniformities differ between the calculated and measured data due to several effects on the wafer during etch, including process set points, step height differences and carried wafer setup all effecting the plasma response at wafer level. However, the close similarities of the expected and actual etch shapes clearly demonstrate a dominant local loading effect which increased etch rate at the edge of the pattern, shown for both the real wafer edge and taped test.

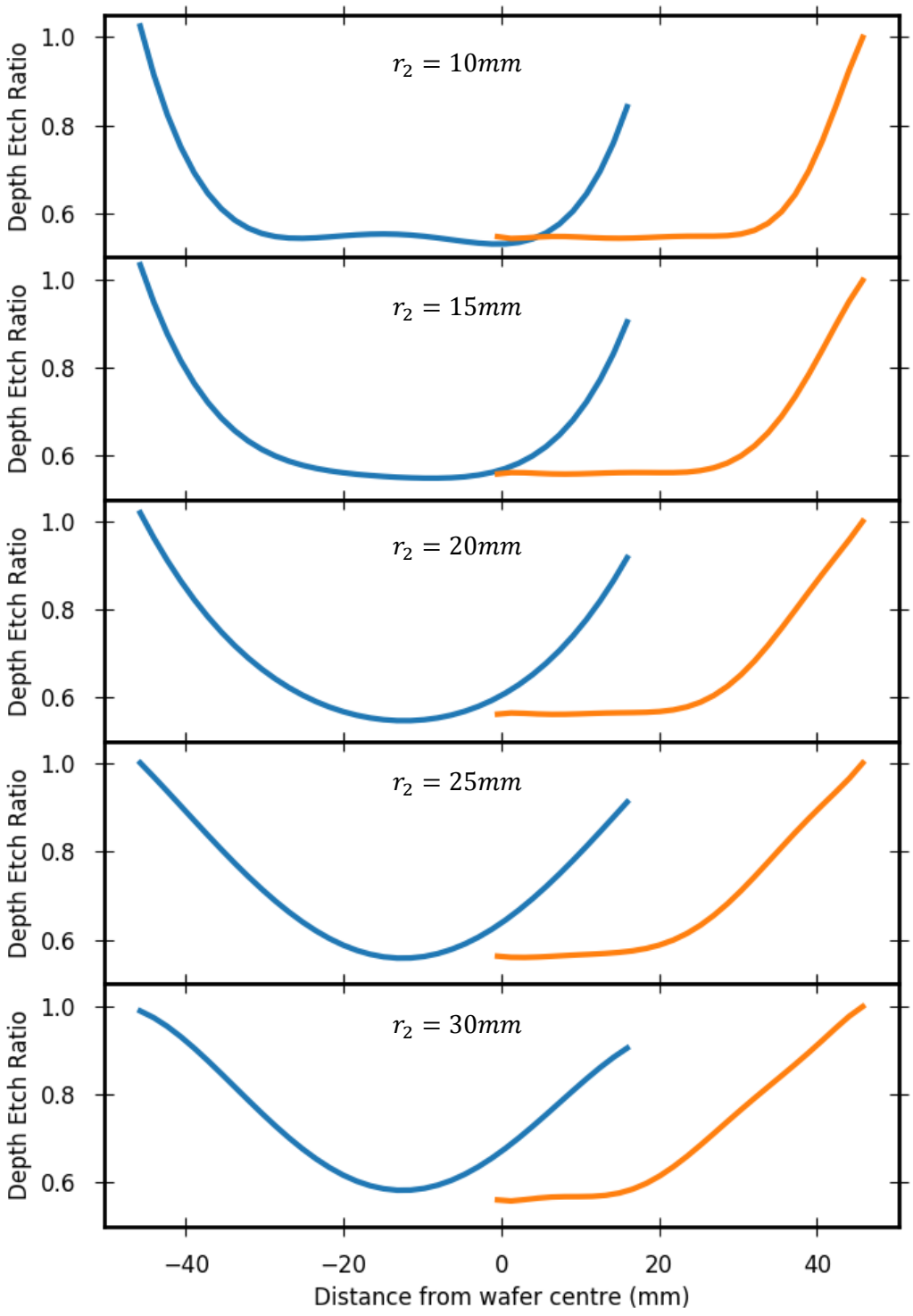

Figure 3.5. *Calculated depth etch ratio versus distance from wafer centre for five fixed values of r_2, using the area of two overlapping circles. Fitted lines appear wavey in some cases due to the use of polynomials. Orange shows the expected Depth Etch Ratio profile for half a normal wafer, with the Blue line showing the expected trace from a wafer taped in the same manner as the physical test. In both cases, the only effect on the trace is the local open area.*

3.3.3 Tuning for Uniformity – Hardware

Previous studies have explored the effects of open area on local etch rate and/or depth non-uniformity [171, 172], usually with a view to optimise a specific mask pattern for minimal depth variations. In addition, these studies often focus on microloading or within-die effects. This program of work is more general and maintains a fixed mask pattern limited to carried wafers, and demonstrates a link between theoretical cause and practical effects of whole-wafer non-uniformity issues while providing an actionable remedy, at least in part, for the high non-uniformity observed for this specific application.

To further test the local loading hypothesis, and improve the etch, hardware options were explored to reduce this effect. SPTS Technologies provides 'Uniformity Rings' for this purpose; Quartz or Ceramic rings to surround the wafer during process to affect the amount of free radicals or plasma sheath shape. In this case, the installation of such a hardware option would not be of any use due to the 100mm diameter device wafers being mounted on 150mm diameter carriers, meaning that the device wafers are 25mm from the uniformity ring significantly reducing its impact. The masked carrier offers no Si to be consumed, resulting in a significant local loading effect on the edge features of the device wafer. Carriers used in this way are not typically part of a normal DRIE production flow, but have to be used in this case due to the topography of wafers after the bevel etch and the presence of a Through-Silicon Via (TSV) after the bore, which would allow Helium to flow through the wafer and compromise wafer clamping and cooling during process. Advantages and challenges to scaling all processes to a carrier-less 150mm production flow is discussed in detail later as part of Further Work, in Chapter 6 Section 6.3.2.

As the device wafers in this case are 100mm on 150mm carriers the uniformity ring was 25mm away from the device wafer in all directions, outside the 20mm shown to affect the local loading in Section 3.3.2. The practical effect of this was changing the uniformity ring in

this setup would not have any benefit on the device wafer's etch depth non-uniformity. In order to test the open area hypothesis, Si pieces were bonded to the carrier around the edge of the device wafer to mimic a whole wafer with uniformity ring setup, shown in Figure 3.6. The bonding of silicon so close to the wafer edge provided a reasonable approximation to the effect a Quartz uniformity ring would have on the process, as the purpose of both is to give the artificial effect of moving the open area beyond the device wafer edge. In certain cases, this shifts the faster etch rate with it, reducing the non-uniformity across the device wafer. This effect is dependent on several factors including wafer pattern, etch requirements, and process being employed. Using Si pieces in this way is not typical of a production environment, but was necessary in this development as appropriate 150mm wafers for device fabrication were not available.

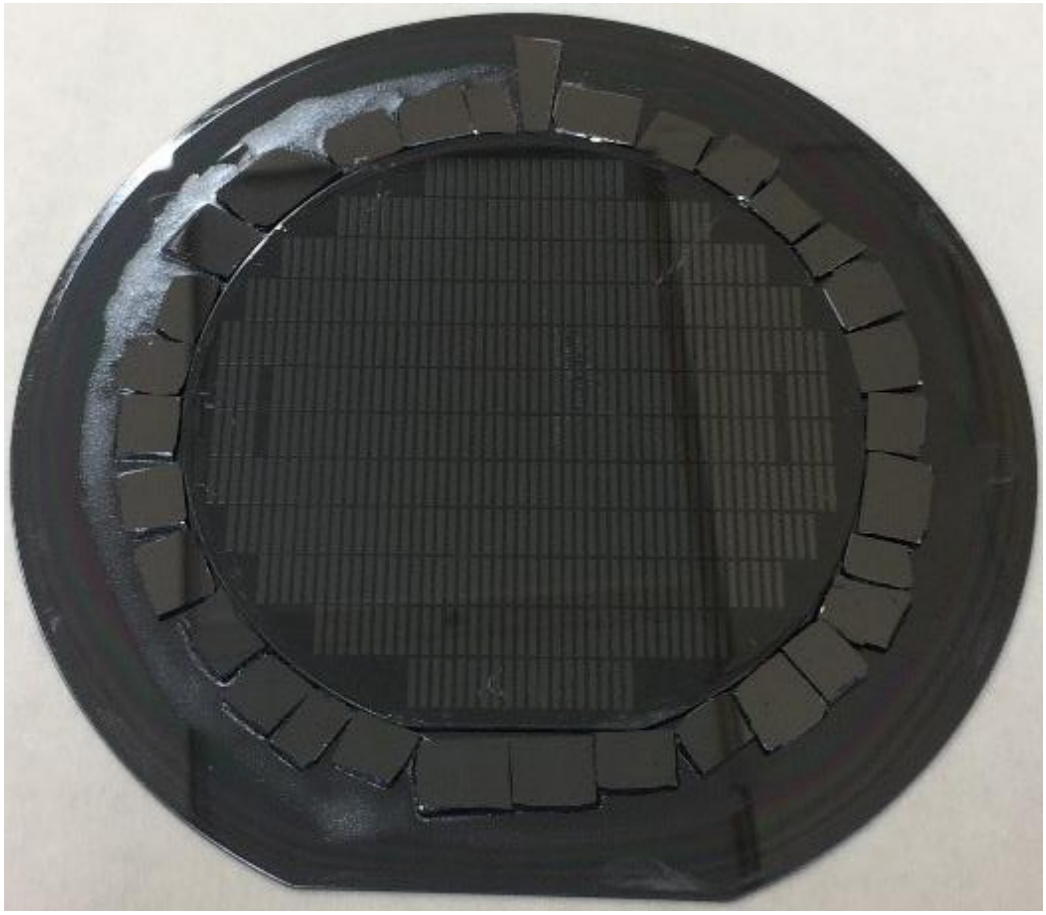

Figure 3.6. *A photograph of a 100mm device wafer before being processed. The device wafer is surrounded by sacrificial Si pieces, with both the wafer and Si pieces bonded to a 150mm oxide carrier ready for etching.*

As can be seen in Table 3.2 and Figure 3.7, this change to the method of wafer carrying has a significant positive effect for the high open area application of the bevel etch, reducing the non-uniformity across the wafer from ±11.3% to ±6.8% when comparing identical processes. This result was expected as both the modelled and practical investigations undertaken in Section 3.3.2 show a heavy reliance on local open area.

Distance from Wafer Edge (mm)	4.2	7.6	12.8	19.6	28.2	36.8	45.4	50.5	Non-Uniformity (±%)
Baseline	1	0.945	0.897	0.855	0.833	0.820	0.810	0.807	**11.31**
Si Ring	1	0.963	0.934	0.906	0.889	0.878	0.876	0.876	**6.80**

Table 3.2. *Depth Etch Ratio results showing the improvement to non-uniformity of a fixed wafer pattern when sacrificial Si is placed around the wafer when processing.*

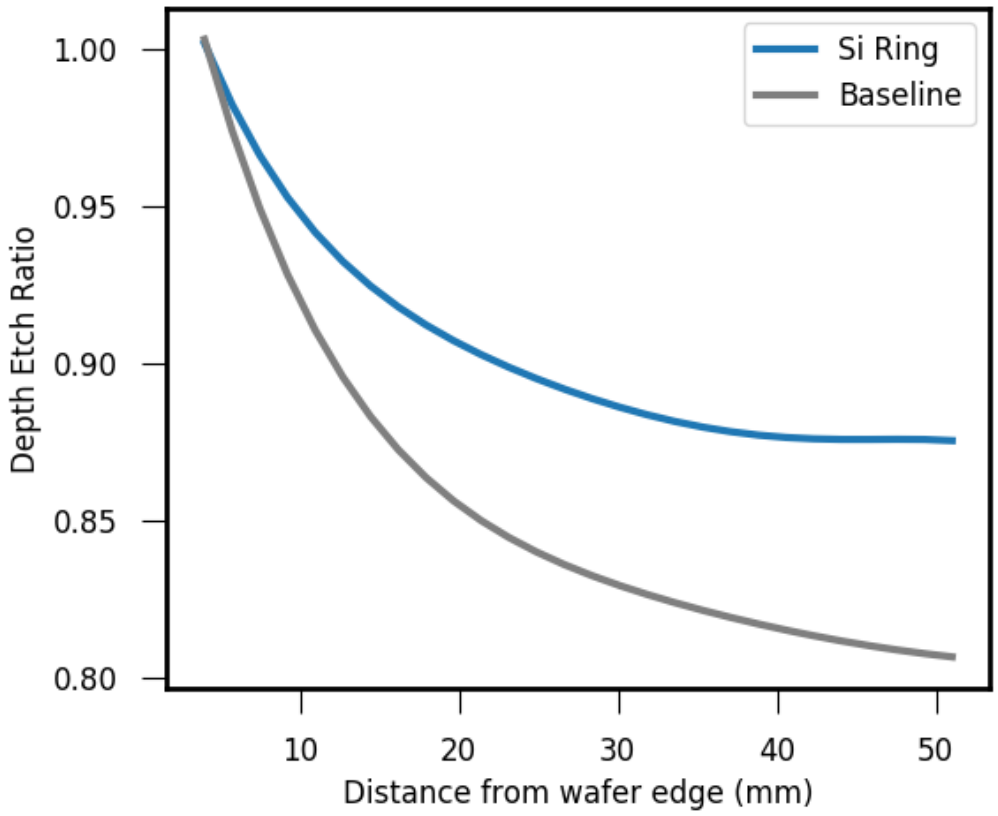

Figure 3.7. *Experimental data showing the improvement in non-uniformity from the baseline (grey) result to the same process with a Si ring (blue) present.*

3.3.4 Tuning for Uniformity – Process

In addition to improving the Si etch uniformity with hardware changes, it was also assumed that the process could be altered to give a more uniform result. Three key parameters were identified for process development based on previous plasma etch experience with the SPTS Rapier™ chamber, focussed on increasing the energy available to

breakdown the SF_6 precursor gas into greater numbers of fluorine radicals available for etching in the desired areas:

- Source RF power; increasing source RF power created a more energetic plasma with more free fluorine radicals available for the etching of silicon. This helps uniformity in high open area etches where local etch rates are dominantly affected by etchant availability, i.e. the etch rate would increase where the Si was previously starved of F radicals, and remain stable where the plasma was already at saturation.
- Secondary source RF power; reducing or eliminating secondary power results in most ionisation occurring over the wafer centre. As the bevel process has a higher etch rate at the wafer edge, an increase of available ions at the wafer centre (and the etch rate increase linked to this) would improve uniformity.
- Process chamber pressure; decreasing the chamber pressure has the effect of reducing the residence time of the reactive species. This decreases the etch rate in regions where the plasma is already saturated but has limited effects on the etch rate of starved areas, as there is still enough F radicals to maintain the previous etch rate.

These parameters were varied individually with the Si ring in place around the edge of the device wafer, and results are compared to the original process with the Si ring in Table 3.3, Figure 3.8. All three process adjustments improved the non-uniformity versus the original recipe, with the largest difference seen in the removal of secondary source power providing an improvement in the non-uniformity from ±6.80% to ±4.23%.

Distance from Wafer Edge (mm)	4.2	7.6	12.8	19.6	28.2	36.8	45.4	50.5	Non-Uniformity (±%)
Si Ring	1	0.963	0.934	0.906	0.889	0.878	0.876	0.876	**6.80**
Primary RF Only	1	0.966	0.952	0.946	0.933	0.923	0.920	0.920	**4.23**
Pressure Down	1	0.973	0.944	0.935	0.916	0.907	0.899	0.894	**5.70**
Source RF Power Up	1	0.960	0.949	0.926	0.911	0.900	0.894	0.894	**5.70**

Table 3.3. *Depth Etch Ratio results from the process variations to test non-uniformity. Si ring data is included as a comparison to discern the effect of individual process changes.*

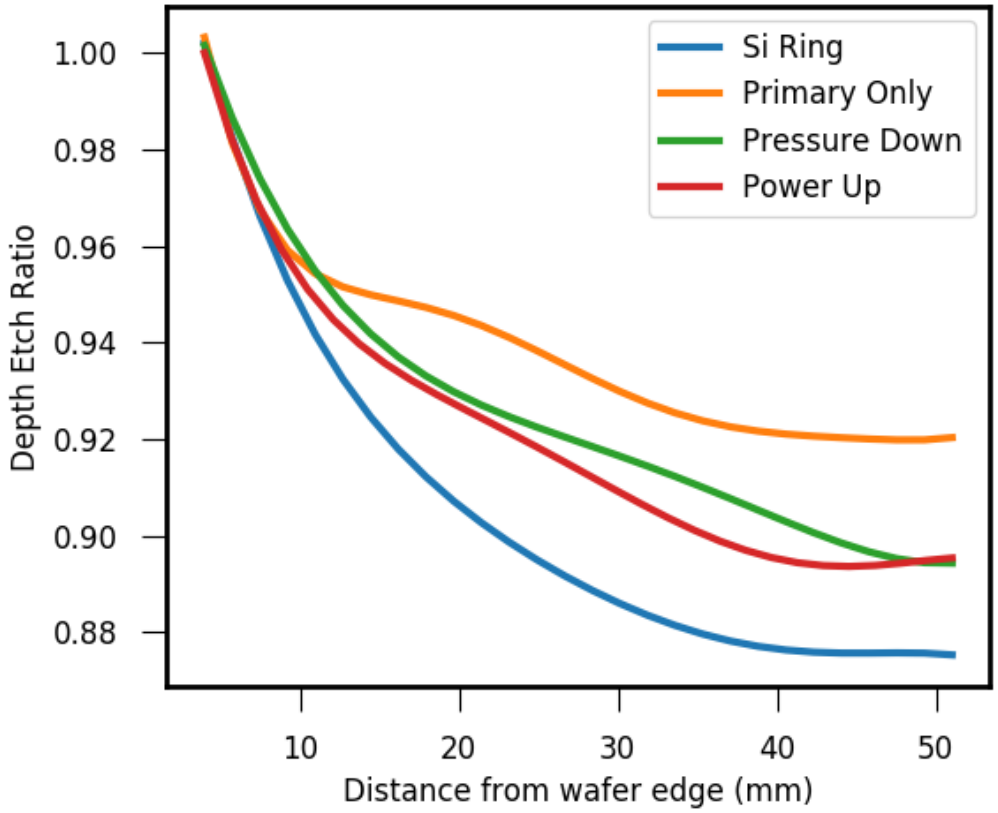

Figure 3.8. *Experimental data showing the effect of various process changes on the etching process. Si ring data has been provided before, but is also included here as a comparative baseline. Increasing source RF power and decreasing pressure both had benefits vs the baseline Si ring process, but the use of only primary source RF power had the most effect.*

As all changes improved the process, further tests were carried out to investigate the result of combining these parameter changes. The secondary RF power remained at 0W, as

this provided the best known non-uniformity, and the lower pressure/higher RF power regimes were tested individually in combination with the removal of secondary power. Results can be seen in Table 3.4 and Figure 3.9, with lower pressure having no effect on the overall non-uniformity of this regime. However, the increase of primary RF power by 25% helped the non-uniformity, with a decrease from ±4.23% to ±3.83%. This was a significant improvement from the ±11.45% seen before hardware and process optimisation, and within the generally accepted band of ±5% that constitutes good non-uniformity for plasma etching of silicon, especially given the open etching area of >45% which consumes etchant F radicals and increases non-uniformity more drastically than a pattern with lower open area.

Distance from Wafer Edge (mm)	4.2	7.6	12.8	19.6	28.2	36.8	45.4	50.5	**Non-Uniformity (±%)**
Si Ring	1	0.963	0.934	0.906	0.889	0.878	0.876	0.876	**6.80**
Primary Source Only (PSO)	1	0.966	0.952	0.946	0.933	0.923	0.920	0.920	**4.23**
PSO + Pressure Down	1	0.960	0.944	0.935	0.925	0.920	0.920	0.922	**4.23**
PSO + Power Up	1	0.973	0.955	0.946	0.932	0.927	0.927	0.927	**3.83**

Table 3.4. *Depth Etch Ratio results from the process change combinations to test non-uniformity. Si ring and Primary Source Only (PSO) data is included as a comparison to discern the effect of individual process changes.*

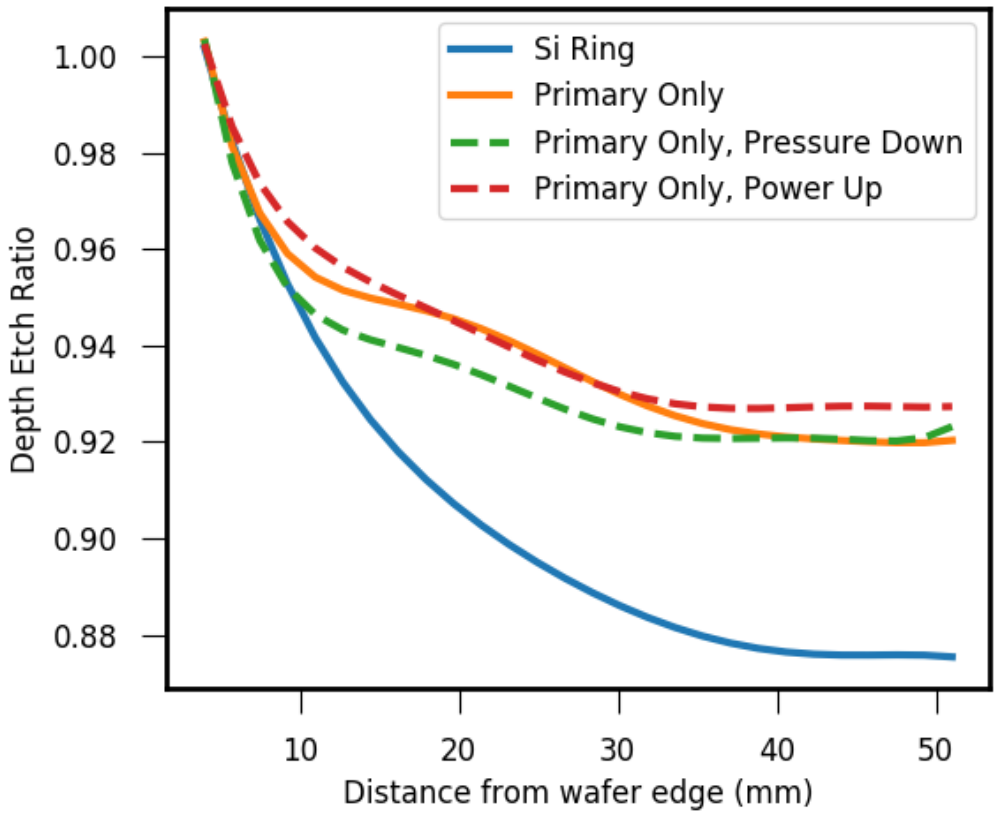

Figure 3.9. *Experimental data showing the effect of various process changes in combination with a primary source only configuration on the etching process. Si ring and primary only data have been provided before, but are also included here as comparative baselines.*

3.3.5 Process Chamber Transfer: Rapier™ to DSi-v™

As described in Chapter 2 Section 2.4.2, the Rapier™ chamber differs from the DSi-v™ due to the presence of the secondary ICP coil around the chamber, which can assist with non-uniformity or trench tilt improvements for some applications. However, in this case the bevel etch non-uniformity is shown to be negatively affected by the generation of secondary ions, and it was thought therefore that the DSi-v™ may provide a better hardware base for the current process regime.

The optimal process developed on the Rapier™ was transferred to the DSi-v™, and retested with the same conditions. The non-uniformity was maintained (Rapier™ ±3.83%, DSi-v™ ±4.00%), but a small increase in depth etch rate was observed from 8.11µm/min in

the Rapier™ to 8.83µm/min in the DSi-v™, although the depth etch rate of this step was not important. The key difference in results between the two chambers was revealed when analysing the lateral etch rate of silicon at the mask interface. This is not a typical metric used to assess a process in the semiconductor industry, but in the case of the bevel etch it is critical to the placement of the shaft pattern on the bevel surface. As can be seen in Figure 3.10, the maximum width of the top surface restricts the tip angle achievable at other points on the wafer; for this reason, the lateral etch of the silicon under the mask was a key indicator of yield from a whole wafer. If the lateral etch rate is consistent across the wafer, shown by a lower lateral etch non-uniformity, the microneedle tip angles across the wafer are similarly consistent.

As shown in Table 3.5 and Figure 3.11, the non-uniformity of the lateral etch rate was significantly improved on the DSi-v™ (±2.76%), compared to the identical process on the Rapier™ (±7.05%). As previously described, this means that the shaft lithography steps produce a more consistent tip angle for the microneedles across the wafer, beneficial in a mass production case.

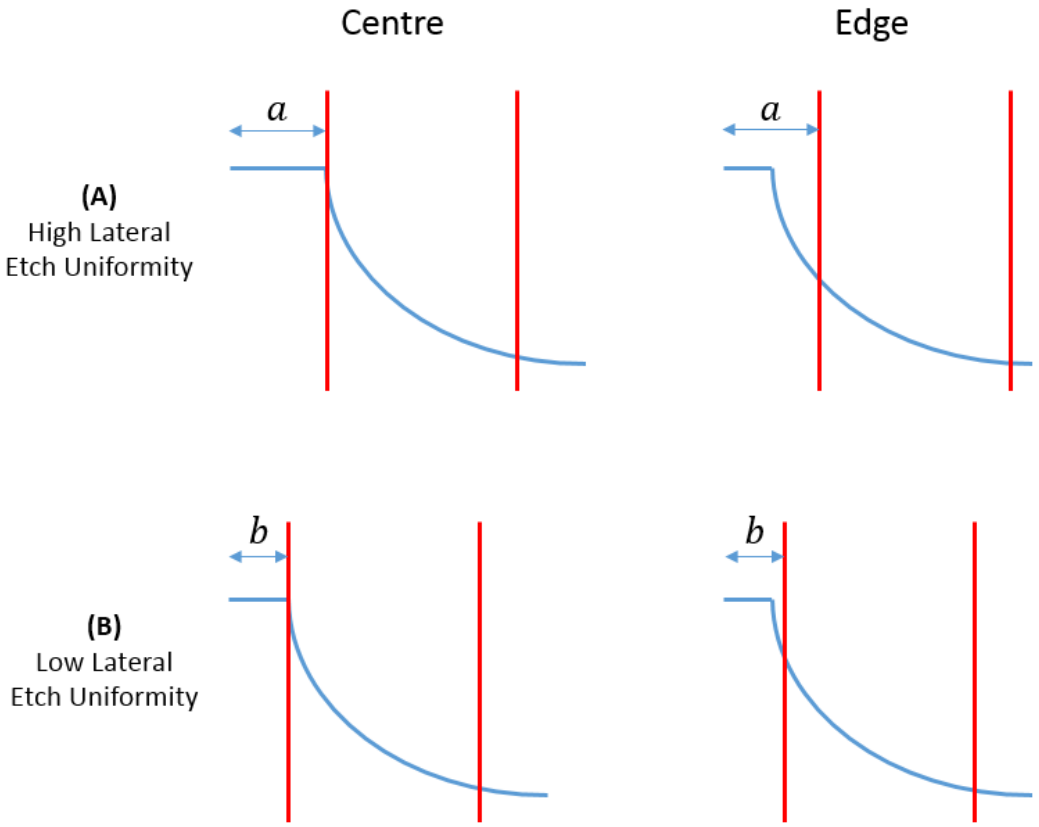

Figure 3.10. *An illustrated diagram to show the benefits of a low lateral etch non-uniformity for this application. Best-case MN placement on the bore is shown in red. In the high non-uniformity case (A), the difference in the width of the bevel tops forces the MN pattern further down the bore at the edge, as it must be displaced as far as the widest point* ***a*** *and results in a detrimental angle to the MN tip at the wafer edge. For the low non-uniformity case (B), the bevel top widths are more similar at the centre and edge meaning that the max width* ***b*** *does not force the patterning as far down the slope at the wafer edge, resulting in a sharper tip and more uniform MN across the wafer.*

	Centre (µm/min)	**Edge** (µm/min)	**Non-Uniformity** (±%)
Rapier™	4.35	5.01	**7.05**
DSi-v™	5.20	5.50	**2.76**

Table 3.5. *Lateral etch rate and non-uniformity comparisons between SPTS DRIE chambers for the Bevel application. The DSi-v™ shows a higher lateral etch rate and significantly lower non-uniformity, making it the preferred chamber for MN production.*

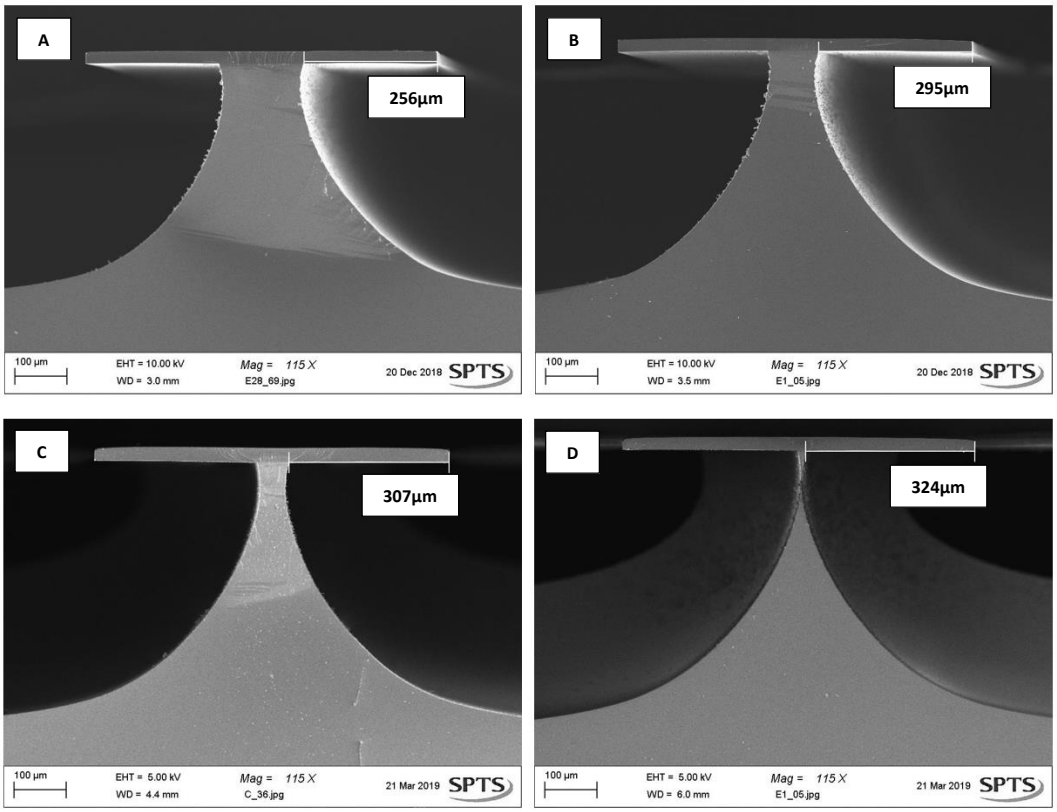

Figure 3.11. *SEM images of the same process performed on a Rapier™ and a DSi-v™, showing features at the wafer centre and edge. Rapier™ results are shown in images A (centre) and B (edge), while results for the DSi-v™ are shown in images C (centre) and D (edge) The DSi-v™ exhibits a much better lateral etch non-uniformity, demonstrated by the smaller differences between the centre and edge undercuts compared to the Rapier™.*

3.3.6 Continued Development

With the depth and lateral uniformities significantly improved, development was continued to refine the etch for implementation in the process flow. As the previous work has focussed on the etch shape of the bevel itself, both in terms of individual trenches and consistency across a wafer, the next step of integration to the process flow is ease of combination with later etch steps. The main consideration for the bevel etch is the shaft etch step; the shaft pattern will have to be completed on the bevel surface later in the process flow.

Similar to the benefits of low lateral etch non-uniformity described above, consistent shaft patterning can also be achieved by totally undercutting the mask during the bevel etch to form a point on all trenches across the wafer. As the two sides of the bevel etch meet in the middle under the mask at all sites on the wafer, the shaft positioning when patterning becomes truly consistent in terms of placement on the bevel surface.

The lateral etch non-uniformity was still important when totally undercutting the mask, as too much overetch at any site will introduce the possibility of the mask losing rigidity with nothing to support it, and 'fall over' – the effect of this is to mask areas of the wafer that were not intended, leading to issues such as particle formation. The etch depth non-uniformity remained the same – although the depth is also increased with the time adjustment needed to undercut the mask in all locations, the vertical etch rate was not affected.

The total mask undercut was achieved simply by increasing the etch time until the feature with the lowest lateral etch rate had undercut the mask at that site, and results in a bevel shape that can be seen in Figure 3.12. Additional analysis of the bevel across the wafer shows a consistent angle, both at the tip (21.8±2.9°) and at half-depth (36.5±3.6°), as shown in Figure 3.13. This process produces sufficient quality of both depth, lateral undercut, and bevel angle to continue to the process flow with this as the final bevel etch result. It provides the angled surface required for facile insertion [73, 151], while the total undercut ensures consistent shaft patterning later in the manufacturing sequence. Parameters and results for the final etch can be seen in Tables 3.6 and 3.7 respectively.

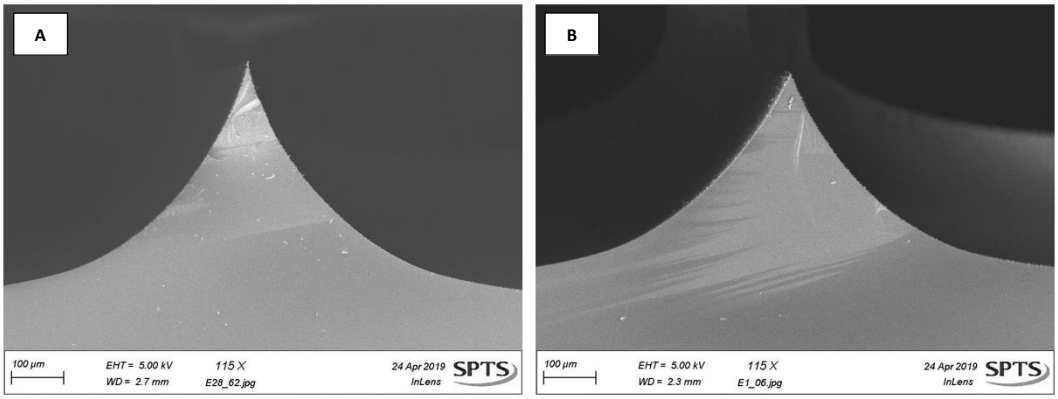

Figure 3.12. *SEM images of the final form of the bevel etch at the wafer centre (A) and edge (B). There is still a slight variation in tip angle due to depth/lateral etch uniformities affecting the propagation of the etch, but by etching both sites to a point the reliability of mask patterning for subsequent steps is greatly improved.*

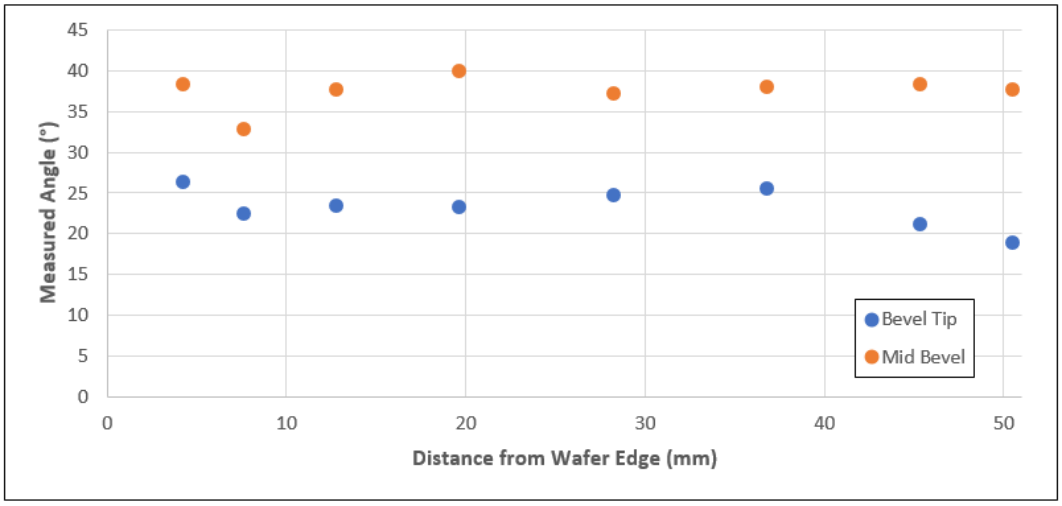

Figure 3.13. *Chart showing plotted values of the angle at the tip (blue) and mid-point (orange) of the bevel by the distance of the measured feature from the wafer edge. The results show good consistency, with angles of 21.8±2.9° and 36.5±3.6° for the tip and mid-point respectively.*

Parameter (Units)	Final Process
{ REDACTED }	

Table 3.6. *DSi-v™ process parameters for the final etch.*

Parameter (Units)	Final Process
Depth (µm)	500
Etch Rate (µm/min)	8.5
Tip Profile (°)	~20
Selectivity (Si:PR)	90
Depth Non-Uniformity (±%)	4.0
Lateral Non-Uniformity (±%)	2.8

Table 3.7. *Etch process results from the final DSi-v™ process. The bevel has a sharp tip and good uniformity, both in terms of depth and lateral etching.*

3.4 Conclusions

To summarise the work described in this chapter, the process required for the first stage of microneedle production has been transferred to and optimised for a state-of-the-art DRIE process chamber. Initial development focussed on the implementation of the bevel etch with

a Rapier™ process module, however high depth non-uniformity of ±11.3% required further investigation.

A link between local open area and etch rate was tested by artificially reducing the open area of the device wafer with tape to prevent etching during process, with the tape having the expected effect on the uniformity shape but leaving the overall non-uniformity unaffected (±11.2%), confirming that the local open area does affect the etch depth for a given feature.

In order to model the effect, the local open area A within a radius r_2 was plotted against the trench displacement from the wafer centre d, for five values of r_2 using the wafer pattern map from the taped case. Although there was a discrepancy in magnitude of the expected effect from area modelling and the measured results, these graphs exhibited a very similar shape to actual etch results and significant work would have to be undertaken to investigate the countless other effects that could impact non-uniformity of a plasma etched wafer. Such work is beyond the scope of this investigation, and the approximate value of $r_2 = 20$mm obtained by this simple modelling again confirms that local open area is a major driver for the etch depth at a specific site on the wafer.

Applying this knowledge to the bevel etch non-uniformity, extending the available Si beyond the wafer pattern reduced the difference in local open area between the centre of the wafer and the edge. Bonding Si pieces around the edge of the device wafer before the bevel etch significantly reduced the depth non-uniformity to ±6.8%. Process changes were also investigated in the Rapier™ chamber to improve the non-uniformity with the best result of ±3.8% obtained when there was no secondary source power but increased primary source power was used in the chamber.

As the secondary source provided no benefit in this case, the DSi-v™ chamber was also used to test the process, and depth non-uniformity remained stable (±4.0%), but lateral etch non-uniformity reduced (±7.1% Rapier™ versus ±2.8% DSi-v™). This will provide benefits for the shaft etch later in the process flow, so the DSi-v™ is the preferred module for the bevel application. In order to further improve patterning for later steps, the bevel etch was developed to produce a pointed shape rather than a flat top. As described, this will increase the consistency with which the shaft pattern can be placed, benefitting ease of alignment in production and the device yield of each wafer.

Wafers for device production are processed using the final recipe described above, before continuing to further steps in the production flow.

Chapter 4

Bore Etch Development and Integration

This chapter will detail the development and implementation of the second dry etch process step in the microneedle fabrication flow, including concept, optimisation, and results.

4.1 Introduction to Bore Etch

In order to facilitate fluid movement through the microneedle a pathway must be created to allow the flow of substance from the backside of the needle, through a channel and exit out of the bevelled surface of the MN. This hollow silicon MN structure permits the transport of fluids through the microneedle and into the skin when the MN is *in-situ*. Conversely, microneedles without a bore rely on the perforation of the *stratum corneum* and subsequent removal of the microneedle to provide enough of an opening to then passively diffuse fluid into the skin [123, 173] in a 'poke and patch' approach. This passive diffusion method significantly reduces the accuracy of delivery volume; a particular issue for medical applications in which doses must be carefully controlled (e.g. diabetes, vaccines [50, 123, 139, 174]). Therefore, the inclusion of the bore in the MN design could be critical to a large number of applications for microneedles, where controlled release is required.

The bore etch itself is completed on the wafer backside (the opposite side of the wafer to the already completed bevel etch step described in Chapter 3). It is completed in this way to avoid any negative effects of processing on the angled bevel surface, where the topography could reduce the quality of the bore etch result.

Semiconductor terminology refers to this type of etch application as a backside Through-Silicon Via (TSV), as it is performed on the bottom or backside surface of the device wafer and provides a channel through the substrate. Typical TSV's are 100-500µm deep, and used for 3D packaging applications where the TSV is lined with an electrical insulating layer and subsequently filled with a metal to provide an electrical pathway through the substrate to another layer of an integrated chip [5, 15, 175].

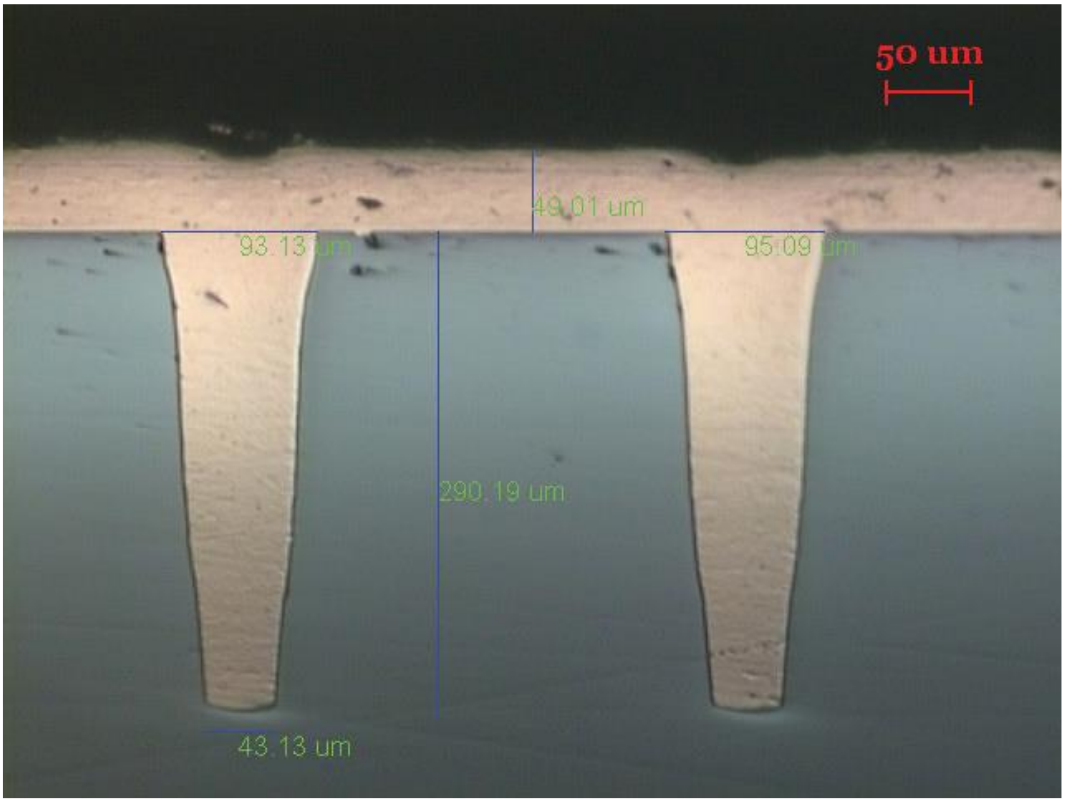

Figure 4.1. *Image of a TSV from literature exhibiting typical etch dimensions with a CD of 95µm etched to a depth of 290µm. An insulating SiO_2 layer separates the copper filled via and silicon substrate [5].*

Unlike standard TSVs, microneedles are fabricated using much thicker wafers. The wafers used for MN production are 1.4mm thick. Subtracting the 500µm depth of the bevel etch described in Chapter 3 leaves a minimum depth requirement of 900µm, and the ability to increase this depth is preferable to allow for deeper MN if needed for certain applications e.g. systemic drug delivery [48]. Etching to the minimum requirement for depth is a challenging task. Processes previously labelled Ultra-Deep Reactive Ion Etching (UDRIE) have achieved results up to 766µm in trenches with 100µm CD [176], which are much easier than vias to etch to such depths. This is due to the increased surface area of the feature opening afforded by a trench rather than more confined circle, allowing increased transport of both etch and deposition species to the feature base at the etch front. Typically a trench with fixed width x will etch ~30% deeper than a circular via with diameter x using the same etch process [176].

This chapter describes the wafer preparation before defining the targets for the etch result. The development of the process is initially performed on new flat test wafers, this is done to isolate the etch process from any effects derived from processing on the bevelled device wafers. Difficulties and challenges of DRIE are discussed and causes/solutions presented. Following process optimisation on test wafers, the process was transferred to the device wafers with the process integration issues presented.

4.2 Bore Etch Method and Metrology

4.2.1 Wafer Preparation and Photolithography

Lithography steps were completed at Swansea University by Olivia Howells. To remove remaining PR from the bevel etch, wafers were cleaned before the bore etch by submersion in TechniStrip P1316. The solution was heated to 70°C and the wafer was agitated until clean, providing a good surface for the bore lithography

To mask the wafer backside with the bore pattern, the wafer was placed front side down on a vacuum sealed chuck so that the wafer back side is facing up. A Laurell WS-650 spin coater was used to apply a layer of AZ125 NXT photoresist onto the wafers, which were then baked on a hotplate set at 130°C for 10 minutes to harden the PR. The wafers were cooled before being transferred to a SUSS MicroTec MA8 for UV exposure of the mask pattern. When immersed in AZ726 developer, the negative tone photoresist exposed to UV remained in place and any portions of the PR that were not exposed were dissolved, to develop the PR pattern on the wafer. To remove excess developer the wafers were washed with DI water and subsequently left to dry in air before use in the production process flow.

Device wafers were bonded to 150mm carriers using 555-HMP Crystalbond adhesive. A hot plate was used to apply the adhesive to the bevelled front side of the 100mm wafer

before it was placed on the 150mm PR coated carrier – PR is used in this case as the device pattern features <1% open area so a photoresist carrier provides open area continuity to the edge of the wafer.

4.2.2 Etch Targets

As described in Section 4.1, the depth of the etch is both the primary target and challenge. The bore is required to extend from the wafer backside to the bevelled surface. A nominal minimum target etch depth of 900µm was set. If possible, >1000µm would allow proof of concept for increased depth, although any increase in this range provides additional challenges as this is already significantly deeper than previous developments in ultra-deep via etching [176, 177].

Sidewall roughness and overall quality are also paramount, as one possible application for the MN is live-cell delivery [38]. Excessive sidewall roughness would affect the viability of cells when transported through the bore, reducing the effectiveness and viability of a given dose. Further to this, roughness and defects affect the flow of fluid through the bore introducing vortices that could inhibit the amount of fluid to be administered. A <3µm roughness target is set to reduce these effects.

The PR pattern for the bore is circular with diameter 100µm, and keeping this CD for the full depth of the bore provides a straight profile which is important to maintain a steady, unrestricted flow of fluid. A tapered profile slows the fluid transit by effectively reducing the aperture through which liquid can be moved to the smallest diameter in the bore. Due to physical restrictions on ion directionality when etching, it is often not possible to maintain a perfect profile of 90°; it is preferable to achieve as close to 90° as possible, but a profile of 90±1° is an acceptable result.

In order to contact the bevel in the correct position, the tilt must be controlled. Tilt is a measure of the verticality of the etch, independent of profile. A Tilt of 0° indicates that the etch is propagating exactly vertically, perpendicular to the wafer surface. If the bore is tilted and meets the bevel in the wrong position when the shaft etch is carried out, there are three possible outcomes:

1. The bore could either be in entirely the wrong place, in which case the bore is in the base plate rather than being central in the microneedle. This would eject fluid onto the skin surface rather than under the skin.
2. The bore could be overlapping with the shaft wall, in which case the bore would extend all the way up the shaft wall; this is functionally the same as case 1 in that any fluid that was injected through the bore would be ejected at the surface of the skin.
3. The bore could be contained within the shaft pattern, but offset in such a way that the shaft wall is thin. In this case, the MN would function as intended but it would be weakened and potentially susceptible to breakage/fracture.

In the ideal case, the bore is central and straight (no tilt) to provide the best possible rigidity. These possibilities are illustrated in Figure 4.2.

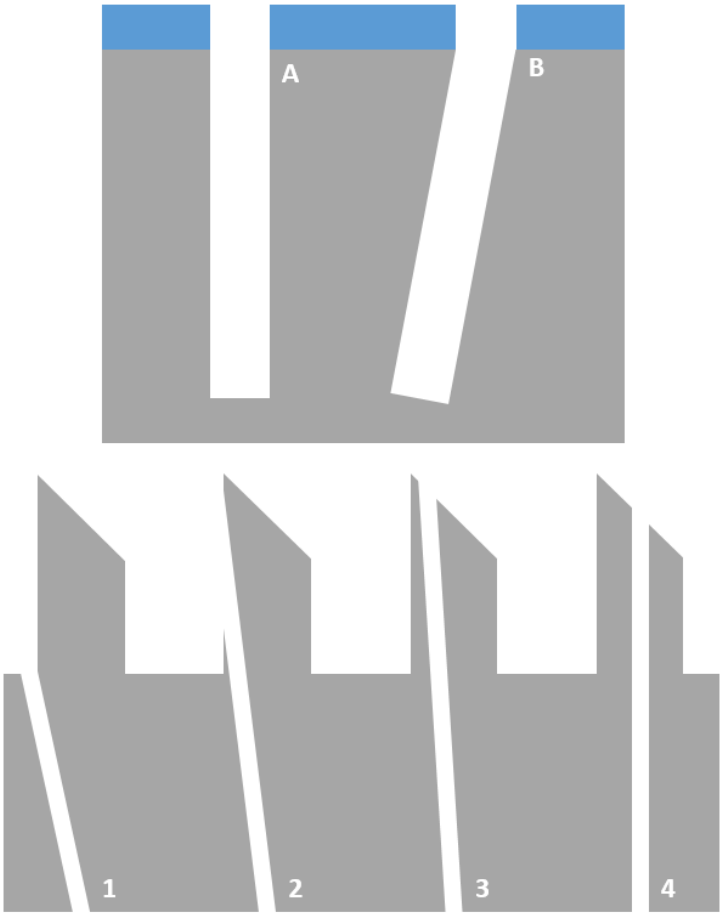

Figure 4.2. *Top; illustration of a feature with no tilt (A) and significant tilt (B). Bottom, illustration of possible effects of tilt on final device showing the bore exiting the baseplate (1), exiting the side of the MN (2), exiting the top of the MN but leaving a thin sidewall (3), and straight with no tilt exiting the top of the MN (4).*

4.2.3 Metrology and Analysis

Analysis of bore etch runs was carried out by cleaving device wafers along their Si crystal plane using a diamond-tipped scribe. The size and shape of the features (100µm diameter vias) makes manual cleaving difficult but because of the wafer thicknesses involved (1.2-1.4mm), it is the only feasible method of directed wafer breakage. Broken wafer pieces were imaged in a Zeiss SEM using the integrated metrology capabilities to provide quantitative analysis. Optical imaging in this feature does not provide significant insight into etch results as the feature is small and optical analysis only provides information on the wafer top surface.

4.3 Bore Etch Development and Results

4.3.1 Etch Module and Initial Results

The etch system used for the bore etch was the SPTS Technologies Rapier™ system. As previously described, the presence of both primary and secondary source RF power and gas flow provides a wider process window to optimise the resulting etch [164]. Etching the via to the required depth is challenging, and the presence of additional options to tune the process increases the likelihood of achieving the target depth with an acceptable profile and sidewall roughness to facilitate fluid flow with the required cell viability [38].

In addition to recipe parameters, a key element of the process control afforded in any SPTS tool for deep via etching is the MORFLEX software [178], which allows the gradual changing of parameters over repeated loops with the process recipe. This allows the etch rate and verticality of the etch to be maintained when used properly. Typically, in a static process the etch rate will drop and the profile closes over the course of a deep via etch as the aspect ratio of the etched feature changes. This is due to the physical difficulty of transporting etch or deposition species to the feature base causing less etching as the process progresses. MORFLEX allows parameters to be 'ramped' to counter these effects, for example step time might be increased toward the end of the process to allow more etching, though other parameters such as gas flows, source/platen powers, and pressures can all be changed to affect the process result [179]. Although the changing of values over time can lead to finer process control especially in features that are historically difficult to etch, the additional complication of ramping values can quickly cause unforeseen adverse effects, particularly when ramping two or more parameters individually.

A switched process was used, the basics of which are described in Chapter 2 Section 2.5.4. [redacted] **{ REDACTED }** [redacted]. SEM images of the initial etch result is shown in Figure 4.3.

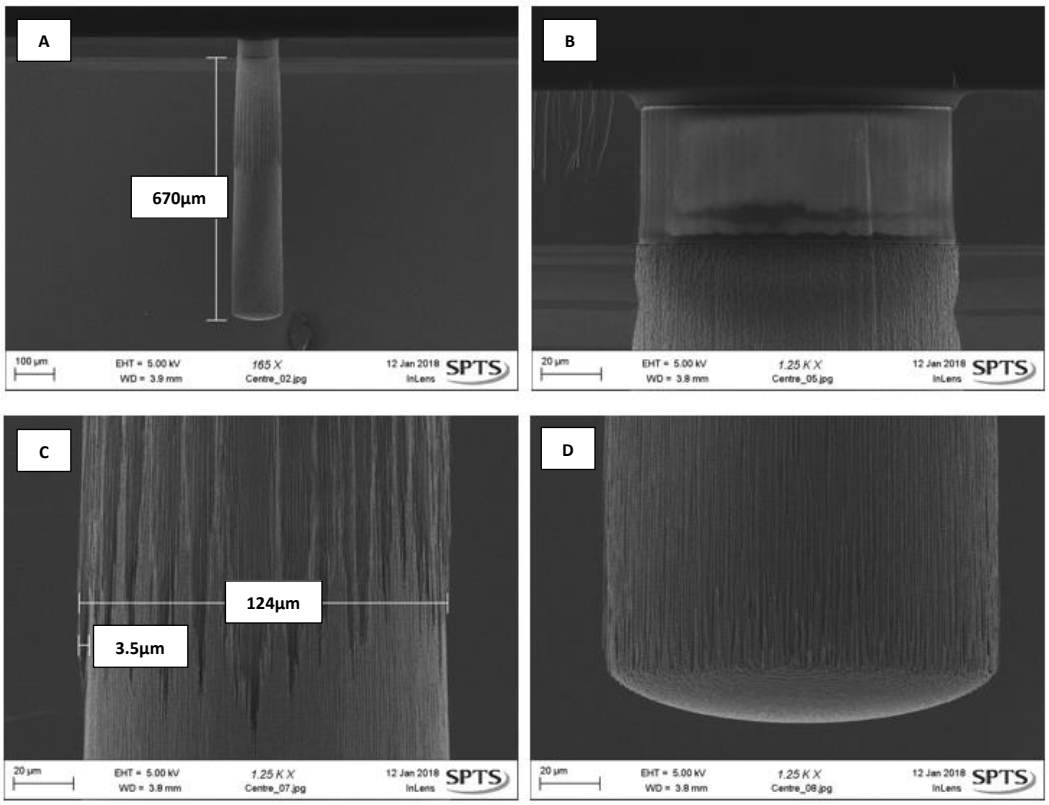

Figure 4.3. *SEM images of the startpoint process in the Rapier™ chamber. Sidewall damage extends down a significant portion of the feature as can be seen in images A and B, and the profile widens towards the base, shown by the increase in CD from the top (B) to base (D) of the feature.*

The initial results were not of the required quality or depth. This was in part due to the uniqueness of the application, but also having the 100mm device wafer carried on a 150mm Si substrate has the effect of removing the device wafer from the cooling effects of the

Electrostatic Chuck (ESC) [15, 17, 18]. A comparison of numerical results to their targets can be seen in Table 4.1. A lack of wafer cooling when etching a TSV often leads to a widening profile, as the deposition laid down to protect the sidewalls is temperature sensitive and less is deposited at higher wafer temperatures. This leads to a wider profile at the base and damage in the sidewalls.

Parameter (Units)	Target	Test 1
Depth (µm)	>900	670
Etch Rate (µm/min)	None	9.9
Profile (°)	90±1	91
Depth Non-Uniformity (±%)	<5	<1
Roughness (µm)	<3	3.5

Table 4.1. *Numerical process results from the startpoint Bore etch in the Rapier™ chamber. Target depth has not been reached, profile is right on the limit, and the level of roughness is not good.*

Initially, to try to control the profile and etch quality the platen temperature was reduced by 10°C in Test 2 to combat the wafer heating effect that reduces the amount of deposition. This produced a significant improvement in the etched result shown in Figure 4.4 and Table 4.2, but due to the limitations of running with carried wafers the heating effect still dominates the profile and quality of the feature which showed a flared profile with damaged sidewalls. In order to fully counter these effects in this method of running, it was necessary to change the process. Figure 4.5 shows the result of Test 3 with the addition of **{REDACTED}** secondary C_4F_8 gas in the deposition step. The result shown in Test 3 shows a significant breakthrough for the process modifications, with near-perfect etch quality and profile at approximately 97% of the minimum depth target. Numerical etch results can be seen in Table 4.2 to compare etch development runs with the target values.

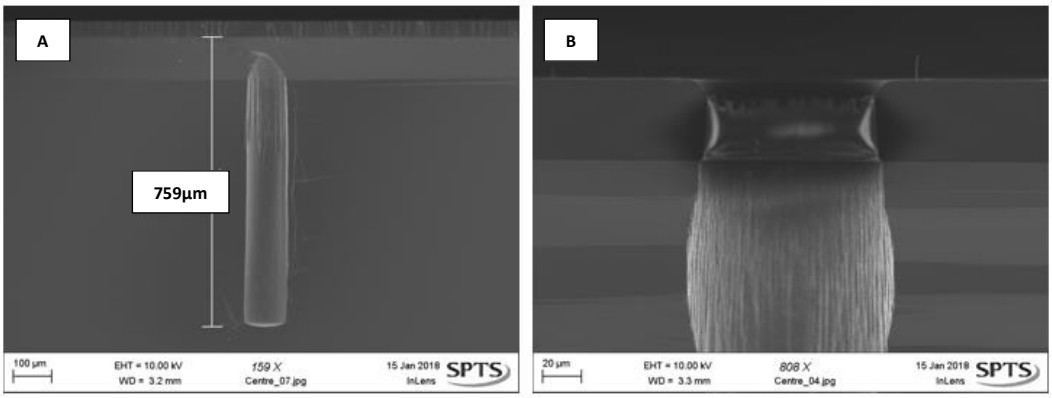

Figure 4.4. *SEM images of Test 2 in the Rapier™ chamber. The etch profile is still too flared, and the sidewall damage still exists as can be seen in the top of the feature in image A – though it has responded to the 10°C platen temperature change, and the sidewall roughness in image B is not as extensive as the previous run. Also given the increase in depth to 759µm, this is an improvement to the etch result.*

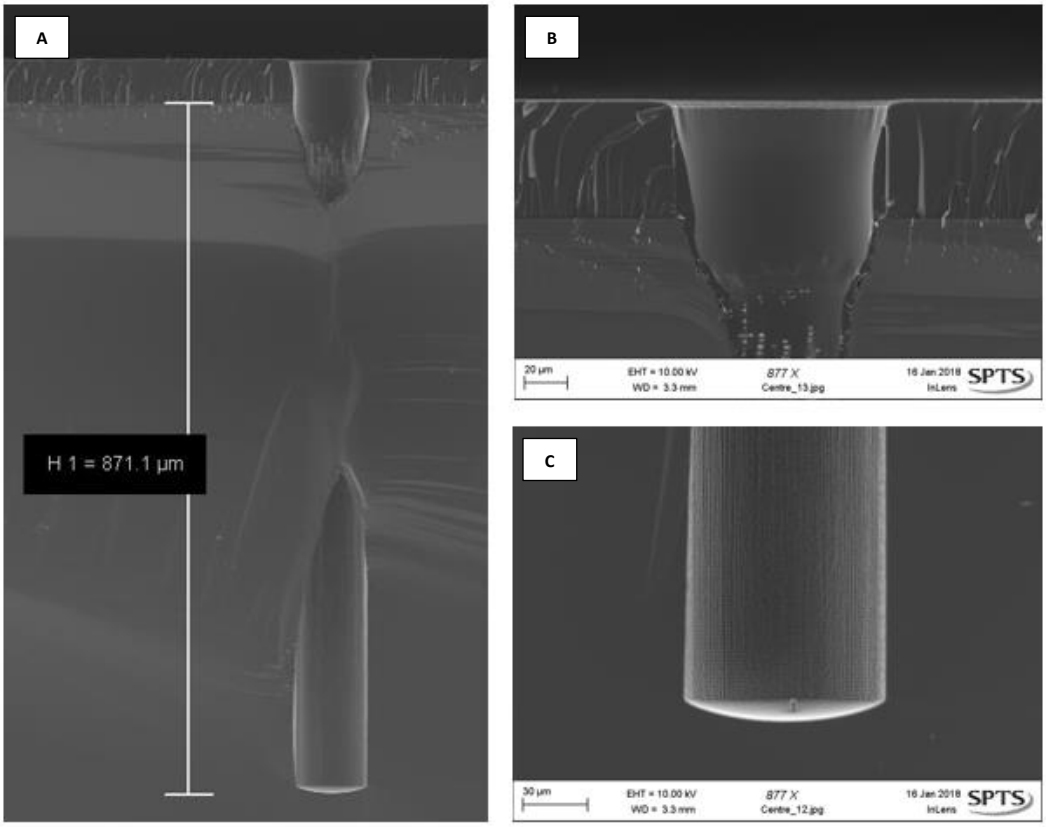

Figure 4.5. *SEM images of Test 3 in the Rapier™ chamber. The process gas alteration made a huge difference to the result, nearly reaching the initial target depth with excellent profile and sidewall quality. The via appears partially covered in image A due to cleaving effects, where the manual breaking of the Si substrate doesn't propagate entirely in the plane of the feature, but this is not an etching effect. The cleave is still good enough to analyse the top (B) and base (C) of the feature.*

Parameter (Units)	Target	Test 2	Test 3
Depth (µm)	>900	759	871
Etch Rate (µm/min)	None	9.7	10.6
Profile (°)	90±1	91.1	89.8
Depth Non-Uniformity (±%)	<5	<1	<2
Roughness (µm)	<3	2.5	2

Table 4.2. *Numerical process results from the initial Bore etch trials in the Rapier™ chamber. Progression is clear across the results, and Test 3 shows a promising path forward for this application.*

To reach the target depth, the etch time of the previous run was increased (along with the end values of any ramped parameters); usually this represents a new baseline result which can then be tuned to meet specifications depending on the quality. However, in this case the etch proved to be stable, reaching a depth of 1157µm deep with a 100µm diameter circular via. No breakdown or damage was observed in the sidewalls, and with small scallops and close to 90° profile all necessary requirements for this etch have been met. SEM images of the results can be seen in Figure 4.6, with numerical results in Table 4.3.

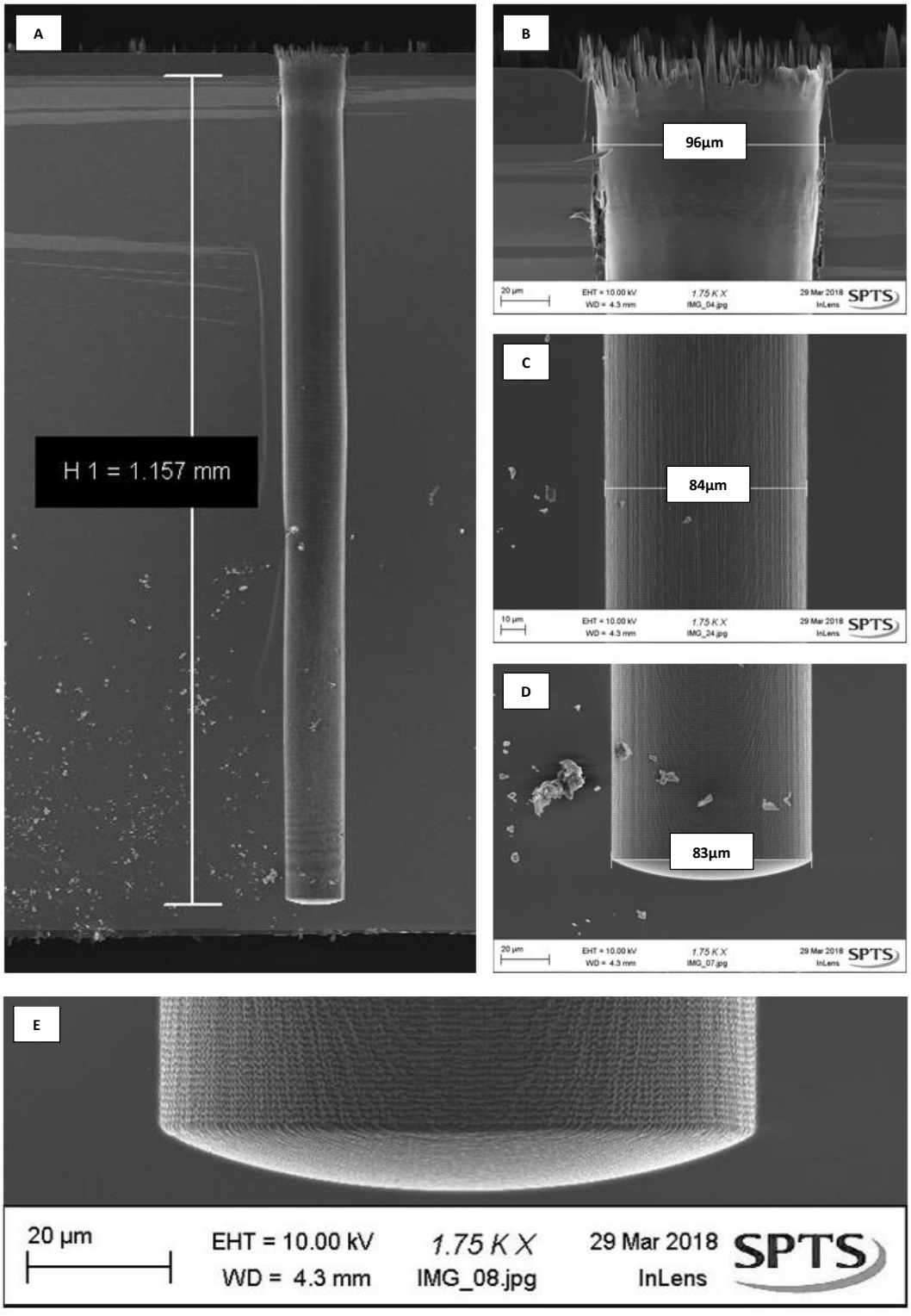

Figure 4.6. *SEM images of Test 4 in the Rapier™ chamber. The feature has significantly exceeded target depth with excellent quality and profile. Image A shows the full feature to a depth of 1157µm. Images B, C, and D show the via widths at the top, middle, and base of the feature respectively. Image E shows a larger image of the feature base with a very clean, high quality etch front and well-defined scalloping.*

Parameter (Units)	Target	Test 4
Depth (µm)	>900	1157
Etch Rate (µm/min)	None	8.1
Profile (°)	90±1	89.7
Depth Non-Uniformity (±%)	<5	<1.5
Roughness (µm)	<3	2

Table 4.3. *Numerical process results from Test 4 in the Rapier™ chamber. Target depth exceeded, with all other parameters also meeting targets.*

The depth achieved with this etch was not only a significant increase on UDRIE via etching, which has been demonstrated in literature to ~520µm [176, 177], but was also deeper than UDRIE etching in trenches shown in the same research. The difficulty of achieving this depth with a reasonable quality cannot be easily overstated, and is only made possible by the selection of a good starting process and extensive knowledge and experience with both SPTS Technologies machinery and cutting-edge plasma etch process developments.

The initial etch result in the development exhibited a poor profile and sidewall roughness, probably caused by insufficient deposition coverage. To test this, the platen temperature was decreased which did improve the result, showing that the lack of deposition was the cause of the roughness and flared profile. The largest improvement came with the addition of secondary C_4F_8 gas flow to the deposition step, which significantly improved the etch quality and allowed the depth to be increased to 1157µm.

The deepest UDRIE etch from the work by Y. Tang *et al* in 2017 was shown to reach 766µm with a 100µm trench CD [176]. The etch demonstrated here on a 100µm circular via to 1157µm was therefore not only 50% deeper than another ‘Ultra Deep’ application, but

was also executed in a feature type that is considerably (~30%) harder to etch. Y. Tang *et al* noted:

> "Comparison of trench and circular hole etch indicate that the in-plane aspect-ratio (length /width, L/W) of the features being etched play an important role on the etch depth and etch rate. 15µm wide trenches reach a depth of more than 520µm whereas the 15µm diameter circular holes only reach a depth of >400µm" [176].

With a thicker wafer, further depth increases may be possible as the etch shows no signs of depth related effects or worsening sidewalls. In terms of quality, no striations, damage, pitting, or profile variation are present, and the sidewall scalloping is well defined; all of these provide an excellent basis for unrestricted fluid flow through the bore.

4.3.2 Process Chamber Transfer: Rapier™ to DSi-v™

It is desirable to perform the bore etch in the same chamber as the bevel etch, the DSi-v™ chamber. This is to reduce the number of etch chambers that are necessary to produce full hollow MN using this process flow, beneficial for smaller institutes or Research and Development facilities who may not be able to fund multiple tool purchases, or do not have sufficient floor space to accommodate several systems. As described in the previous chapter, the DSi-v™ module has significant benefits for the bevel etch due to its lower chamber volume and single plasma source allowing better process control of high open area applications. However, for applications such as thinner trenches and TSV's the additional parameters available on the Rapier™ system usually provide much better control of CD and depth non-uniformity. This is because the position of ion generation can be controlled using the primary and secondary gas/power inputs, and can even be differed between Dep/E1/E2 steps when required for maximum control.

Consequently, the challenge with moving to the DSi-v™ for the Bore etch is controlling the etch to the same high standards present in the Rapier™ chamber for this application. This in non-trivial, and the limitations of the DSi-v™ may have detrimental effects on the etch quality. If this is the case then despite cost benefits for research or production facilities, the quality of the MN would have to remain the overriding priority.

With this in mind, the development of a DSi-v™ Bore etch process began with the same criteria as the Rapier™ development, described in Section 4.2.2. In other (more common or less complex) cases, a Process of Record (POR) may exist on the required tool type which can be used as a startpoint. As this application is unique in terms of depth requirements, it was easier to begin development with the existing processes from the Rapier™ and modify them. As the DSi-v™ and Rapier™ are somewhat similar, the first DSi-v™ recipe is determined by removing the secondary coil power from the Rapier™ recipe (as the DSi-v™ has no secondary coil), and slightly increasing the primary source power to compensate. The number of loops is also reduced, though only to stop the etch propagating too far; an etch rate increase is expected between chambers.

Initial results (Test 5) from the DSi-v™ transfer show similar quality to the Rapier™ etch and numerical results can be seen in Table 4.4, with SEM images in Figure 4.7, though at a reduced depth of 823µm. This depth can be taken as a positive, as it was close to the pre-determined target depth and no signs of the expected DSi-v™ specific Aspect Ratio (AR) dependent effects from the lack of secondary ion generation have been observed. The base width of the feature is slightly larger than the top width, meaning that the overall profile is >90°. In this sort of feature, negative profile can be an indicator that there is too much platen power. As this is a small manifestation of this effect there isn't a need for a huge correction to the process, but along with increasing the time to reach the target depth, future runs had the platen power reduced to control the profile and balance the process.

Parameter (Units)	Target	Test 3 Rapier™	Test 5 DSi-v™
Depth (µm)	>900	871	823
Etch Rate (µm/min)	None	10.6	10.9
Profile (°)	90±1	89.8	90.1
Depth Non-Uniformity (±%)	<5	<2	-
Roughness (µm)	<3	2	1

Table 4.4. *Numerical process results from the first result in the DSi-v™, Test 5. A similar depth result from the Rapier™ is shown for comparison, Test 3.*

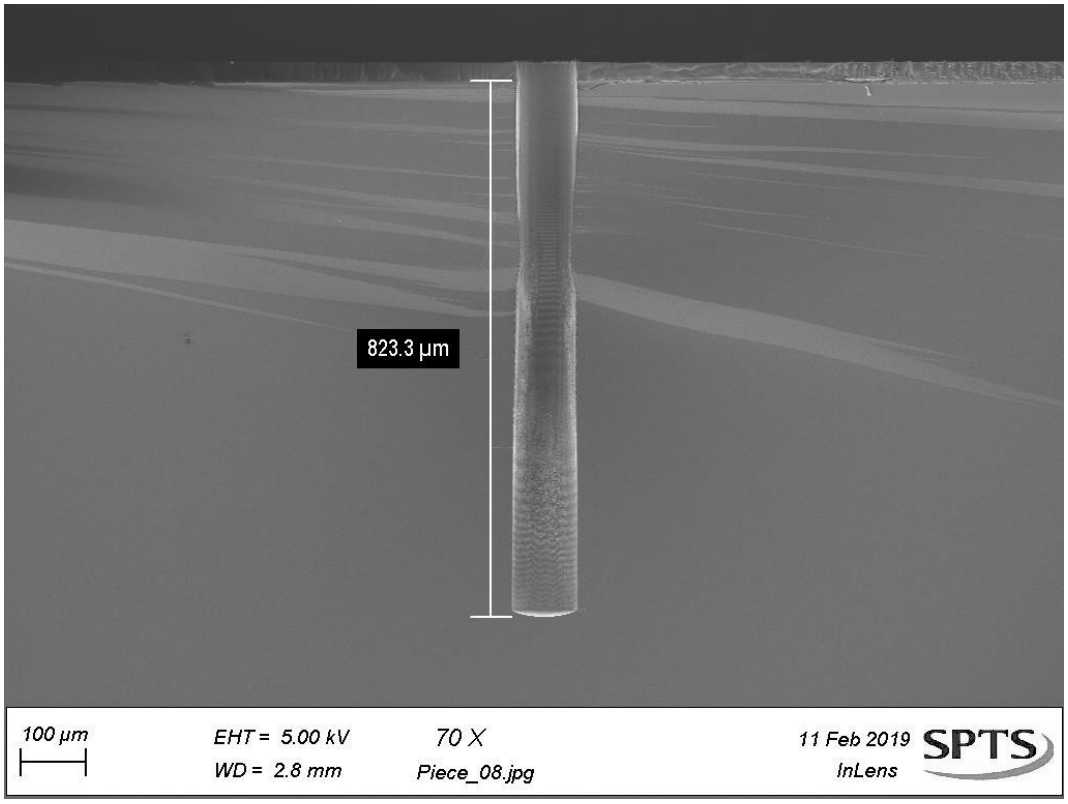

Figure 4.7. *SEM image of Test 5, the first result processed in the DSi-v™ chamber. The middle CD is artificially pinched by a cleave effect, with top and base CD's measuring 98µm and 100µm respectively.*

Figure 4.8 shows the result of multiple process changes in Test 6, specifically to address the profile and increase the depth with an increased source RF power and reduced time for the deposition step. Target depth had been achieved with a good profile from the changes

to the process parameters. Source power was increased in Dep and E1 to increase the number of ions and radicals in the plasma, and the deposition time was reduced to limit some of the build-up at the top of the feature as this can constrict the entrance to the via, exacerbating AR effects by reducing the access aperture for etch species which artificially makes the CD smaller. In this case, the change has reduced the deposition too much leaving a small portion of the top of the feature open to etching which has resulted in pitting. Pitting is a form of undesirable damage caused by a tiny opening in the sidewall protection allowing small amounts of isotropic etching in the Si sidewall, as can be seen in Figure 4.8 with the rest of the SEM images from this run. The deposition time must be balanced between protecting the sidewall from pitting, and excessive deposition build up constricting the via CD.

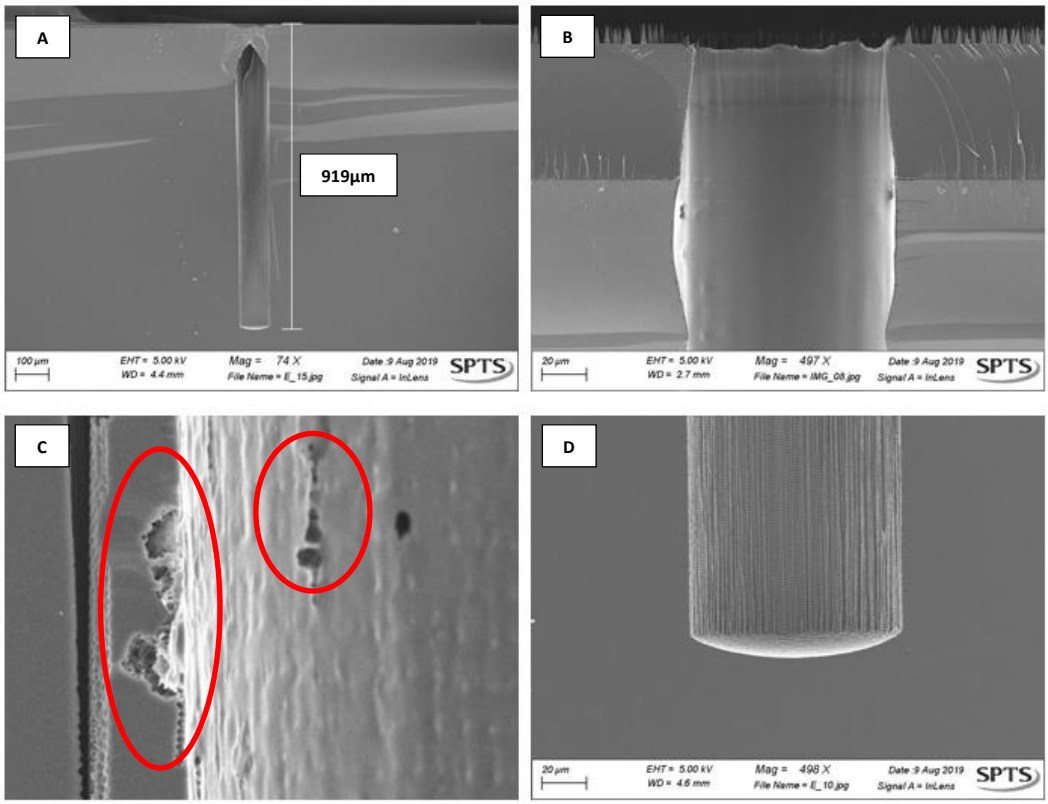

Figure 4.8. *SEM images of Test 6 in the DSi-v™ chamber. Although the top of the feature in image A has been covered by a cleave effect, it does show that target depth has been reached with generally good etch quality, as seen in images B and D. An example of pitting damage is shown in image C, with the undesirable effects highlighted in the red ellipses.*

A slight increase to the deposition step times to address the pitting damage was combined with extending the process depth in Test 7, the result of which can be seen in Figure 4.9. The top of the feature is near perfect, with defined scalloping, conformal deposition and no damage. This quality extends to a significant portion of the full depth of the feature, before AR effects take hold and start constricting the profile towards the base, with some damage being introduced. It is possible to improve AR effects in shallower TSVs, as demonstrated by SPTS Technologies Ltd in Figure 4.10 which shows the improvement of roughness and profile in a 10x100µm via over the course of a development, also processed in the DSi-v™ chamber. The aspect ratio is in line with that of the bore (10:1 vs 13:1), showing that reducing AR effects is a possibility in features of this type. However, the bore depth of 1365µm is a significant achievement with a single source DRIE machine at over twice the depth of a standard thickness wafer – it may be possible to reduce some of the negative effects but it would require an extensive, costly, and time-consuming investigation. Given the requirements for this application, this was not necessary as the etch quality in this feature to ~950µm is sufficient to allow live cell delivery [38].

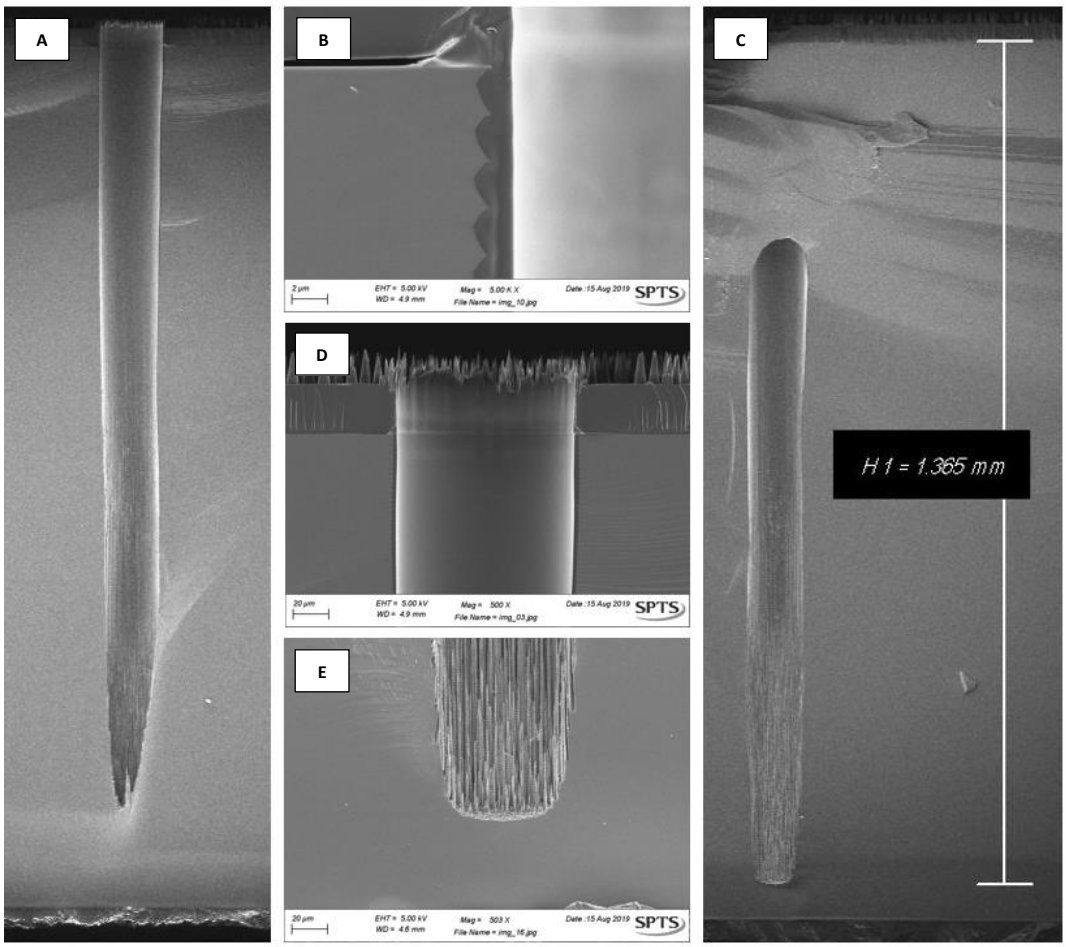

Figure 4.9. *SEM images of Test 7 in the DSi-v™ chamber. The deepest etch in the development; the top is as good as can be expected for any via application. Striations and damage start to form at about 950µm depth, closing the profile towards the base. Cleave effects have prevented capturing of the whole via in one image. Image A and C show the top and bottom portions of the via respectively, with Image C also giving the depth measurement of 1365µm. Image B shows the excellent scalloping at the top of the feature, with images D and E showing the difference in quality at the top and base of the via. Spikes on the mask in image D are from localised spots of excessively hardened mask and do not affect the etch.*

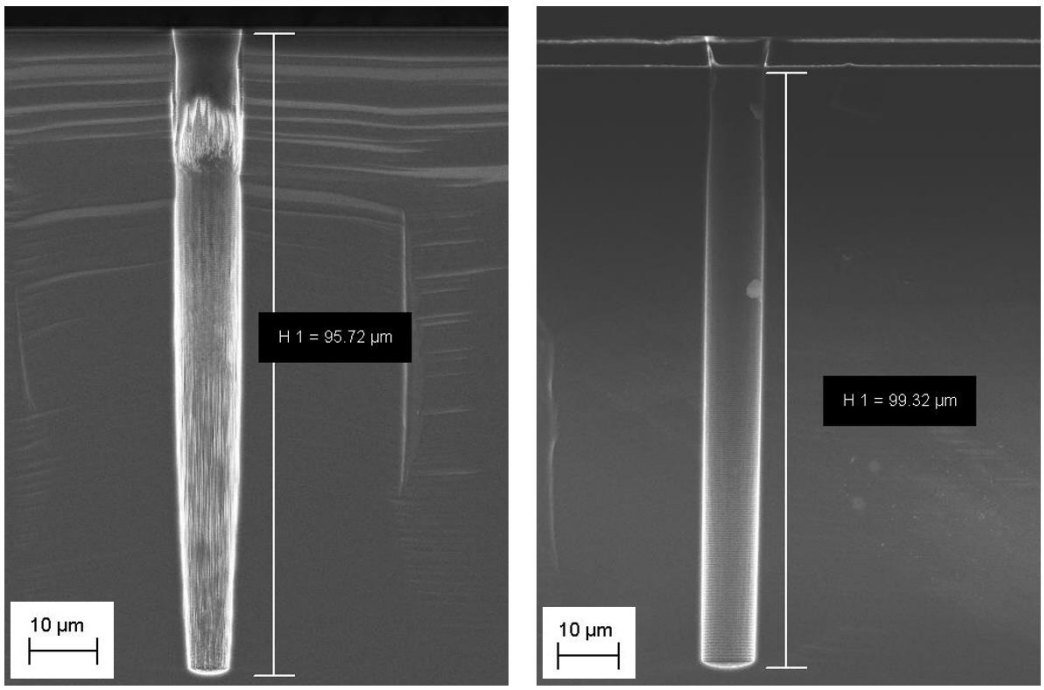

Figure 4.10. *SEM images of 10x100µm TSVs processed in the DSi-v™ chamber by SPTS Technologies Ltd. Left; early in development, exhibiting significant sidewall roughness and profile tapering near the feature base. Right; result after several optimisations showing a near vertical profile and no roughness, overcoming the AR effects.*

In future developments, if >1000µm depth is required for the bore etch then a Rapier™ etch module would be recommended to maintain etch quality. However, for the current design of MN the DSi-v™ meets requirements for the bore etch and is also beneficial from a commercial perspective.

4.3.3 Notching

Notching refers to a specific type of sidewall damage observed when an etch is terminated on an insulating or semi-insulating stop layer. To analyse this characteristic, Test 7 was etched on a flat wafer setup with a photoresist stop layer. The aims were:

a) to make sure that the notching effect was present, pronounced, and measurable; and

b) to provide a repeatable platform for analysis.

Notching and its causal mechanisms have been extensively studied [18, 180, 181], and is considered an undesirable side effect presented when stop layers are used in design, because it increases the base CD of the feature and can introduce structural weaknesses under stress loads, decreasing durability and reliability. In general, notching is the result of ion deflection, with the stop layer becoming charged and repelling the incident ions into the bottom interface of Si to the stop layer, causing issues such as CD expansion and severe sidewall damage. Figure 4.11 shows various illustrations of the possible manifestations of notching.

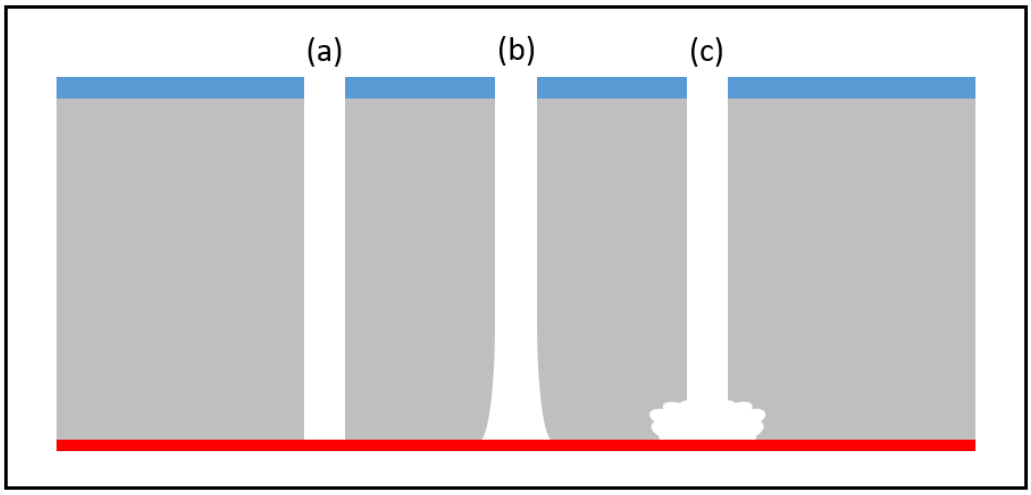

Figure 4.11. *Diagram showing manifestations of notching. No notch is visible in feature (a), and moderate notching is seen in (b) with the CD flaring outwards towards the feature base due to mild ion deflection altering the trajectory of incoming etchant species. Feature (c) shows extreme notching, where severe ion deflection causes uncontrolled damage at the stop layer interface.*

As stated, to test the notching for the Bore etch, the process was performed on a test wafer with PR stop layer, as described above. SEM images can be seen in Figure 4.12, and show the magnitude of the notch. The CD increase of 42% is significant, with additional undesirable damage in the notch. With a large notch of 21µm per edge for the bore etch the microneedle is at risk of physical weakness from the damage to the bore opening, and irregular fluid flow which could disrupt the effectiveness of delivery.

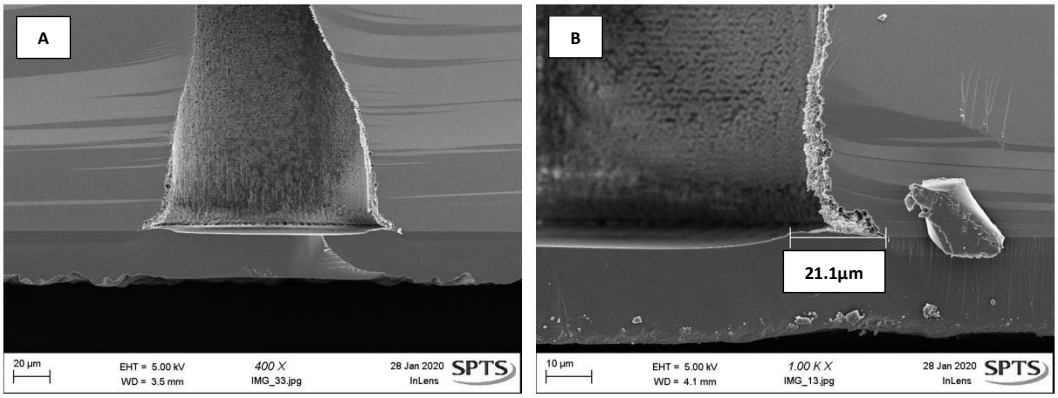

Figure 4.12. *SEM images to demonstrate typical notch formation, prior to development. Image A shows the whole base with the notching present on both sides, while image B focusses on one side of the feature. The 21µm notch has increased the base CD by 42%, with damage present in the notch itself.*

In SPTS DRIE process chambers there are two hardware options available for platen RF power delivery, namely High Frequency (HFr) and Low Frequency (LFr). The difference between these options, as the names would suggest, is the frequency of the AC power delivery; HFr generators deliver the platen power at 13.56MHz (RF), while LFr generators deliver power at 375kHz. Although HFr is the standard equipment for platen power delivery, LFr can have a positive impact on notching. In theory this is partially due to the 'off' period for the LFr being longer due to its lower frequency, allowing the stop layer to discharge reducing the force with which incoming ions are deflected [182]. Another reason for reduced notching with LFr is the lower frequency allows generated ions to respond to the changes in RF potential, more so than with HFr platen RF delivery. This increases the number of low energy ions, which have a lower directionality and increased charge dissipation properties [183]. However, the mechanics of LFr and notch control are not well understood due to the number of variables at the etch front.

Platen pulsing is a process parameter that switches the demand platen RF power on/off during the step [18, 183]. Control of the platen pulsing is achieved through two parameters – frequency and Duty Cycle (DC). The platen frequency controls the number of cycles per

second measured in Hz, and the duty cycle controls the amount of cycles that have the recipe power applied for, measured as a percentage. Duty cycle is one of the keys for notching. Similarly to LFr, the 'off' period of the pulsing allows the stop layer to discharge, preventing ion deflection. The lower the duty cycle, the longer the power is 'off' and the longer the stop layer has to discharge. LFr power can be pulsed, compounding the benefits for notching [183].

In order to maintain an average delivered power, the recipe requested (peak) power must be adjusted in conjunction with the platen pulsing DC. For example, 100W @40% DC is approximately equivalent to 200W @20% DC as the average delivered power over the whole step would be the same. A conversion for various duty cycles can be seen in Table 4.5 for a fixed average platen RF power. Lower platen DC is preferable for the control of notching, however the lower bound for DC is limited by this relationship as the peak power delivery is affected by both matching and max generator output capability. In practice, this limits the DC to a lowest level of around 10%, or 5% in extreme cases, for typical RF generator ranges of **{ REDACTED }**.

Demand Platen RF Power	Duty Cycle (DC)	Average Delivered Platen RF Power
x W	100 %	x W
$1.33\dot{3}x$ W	75 %	x W
$2x$ W	50 %	x W
$4x$ W	25 %	x W
$10x$ W	10 %	x W

Table 4.5. *Comparison of required demand platen RF powers to achieve xW average delivered at varying levels of DC.*

With DC reduced to the minimum level with the required platen power, trials of HFr vs LFr platen delivery on test wafers showed that notch is significantly reduced in the LFr case, as can be seen in Figure 4.13 with a numerical comparison of results shown in Table 4.6. The notch can no longer be measured, a massive improvement from the HFr result. This is theorised to be due to the inherent characteristic of LFr, that the stop layer has a long time between peaks to discharge and reduce the damage-inducing ion deflection. With the exception of a simple comparison between HFr and LFr notches with this specific process, a detailed investigation into LFr benefits for all notches is not possible due to the almost infinite applications and process conditions. Instead, it can only be said that LFr is definitely beneficial in this case.

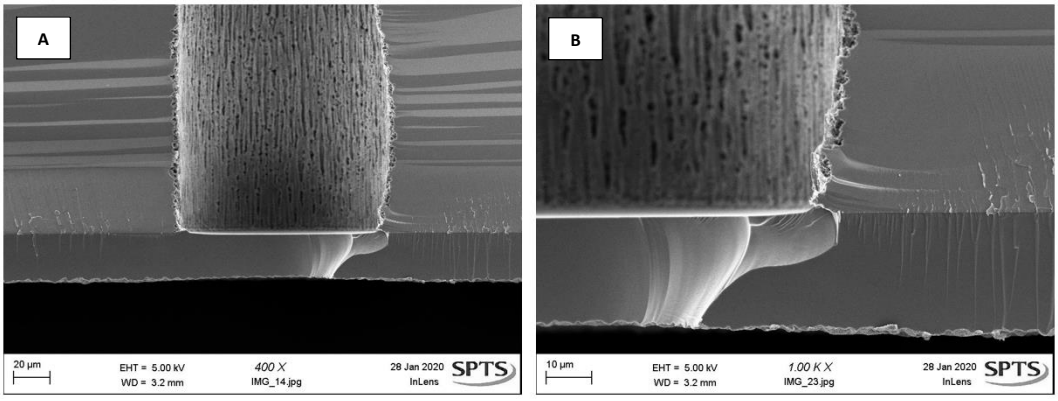

Figure 4.13. *SEM images showing the reduced notch using LFr platen delivery and reduced DC. Image A shows the whole trench base, with B showing a higher magnification of the via interface with the stop layer. Minimal CD loss is present, beneficial for MN applications.*

	Measured Notch (µm)	**Bottom CD (µm)**
HFr Platen RF 50% DC	21.1	143.5
LFr Platen RF 25% DC	None	106.6

Table 4.6. *Numerical results of the measured notch and bottom CD with HFr platen RF power at 50% duty cycle compared to the results when processed with LFr platen RF power at 25% duty cycle.*

4.4 Process Integration: Bevel and Bore

With a satisfactory process developed for both the bevel and bore etches, the next step was to test how well they can be integrated. This is essential for manufacturing, if process combination is hard or requires significant work between steps then it would have severe knock-on effects for scalability of production.

Bevelled wafers were produced using the process described in Chapter 3, and prepared for the bore etch as per Section 4.2.1. In addition to the masking steps previously described for flat test wafers, blue tape was applied across the bevelled device surface to allow vacuum sealing on the PR spinner chuck. The wafer was placed front side (tape) down on the chuck so that the flat wafer back side is facing up, illustrated in Figure 4.14. The method of PR application was the same between test and device wafers.

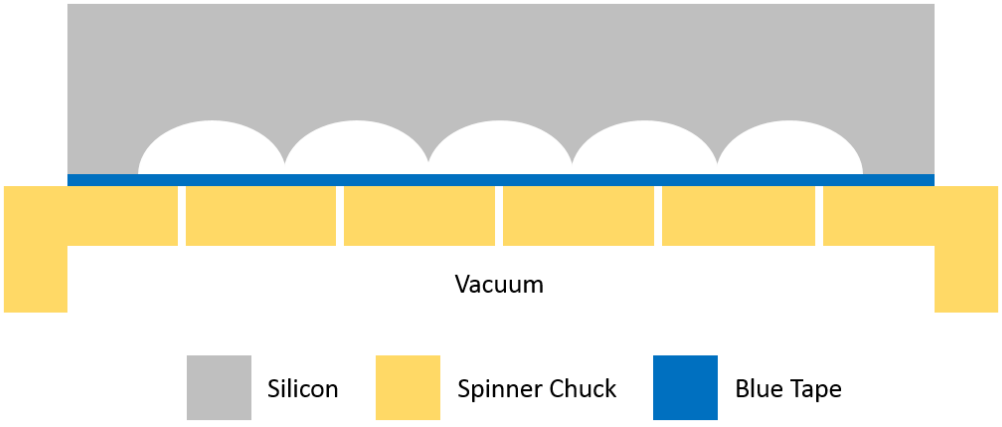

Figure 4.14. *Illustration of the taping method allowing vacuum sealing of the inverted device wafer on the PR spinner chuck.*

During the bore etch process, the non-planar device surface on the bevelled wafer front side needs to be covered to provide a stop layer to prevent unwanted etching. This was achieved using a SUSS MicroTec AS8 spray coater to lay AZnLof2070 photoresist in the bevel

trenches, with acetone used as a thinning agent for the resist. The acetone facilitates the spraying of resist onto the surface, but evaporates after application to wafer as the AS8 has a heated chuck. Sprayed resist must be used in this case due to the topography of the wafer surface.

The key step within the preparation of production wafers was the application of PR to the bevelled surface. This had two notable effects; firstly it prevents the etching of the carrier wafer beneath the device wafer, and secondly it prevents the Crystalbond 555-HMP adhesive from entering the bore hole. The adhesive is very problematic to remove from the bore and can travel up the bore during process to flow out the top causing a messy, unusable wafer. The PR coating on the bevel prevents this by forming a 'stop layer', a layer in a semiconductor device, which is typically only present to provide a stopping point for the process to prevent further etching.

When combining the information from the previous test development, a 'best guess' bore process was performed on a bevelled device wafer. Etching to an angled surface, such as is necessary in the case of the bevelled device wafers, is extremely uncommon and therefore provides a unique challenge in terms of notch control. The chosen etch process conditions used both LFr and the lowest DC possible before reaching the limit of power from hardware components. The notch present on the device wafers can be seen in Figure 4.15, and justifies the previous efforts to control the notching. While the overall notching was at an acceptable level it is asymmetric.

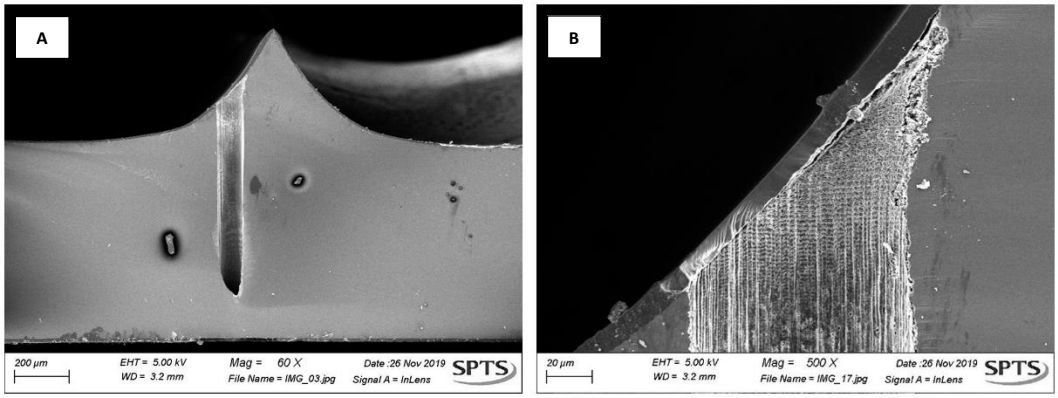

Figure 4.15. *SEM images showing notching of the bore process when performed on a bevelled device wafer. Image A shows the full via etched to a depth of 960µm and making contact with the angled stop layer on the bevel, but cleave effects have obscured the via opening at the bottom of the picture. A higher magnification image can be seen in B, showing the interface of the via with the angled stop layer. The notch effect is only present on one side of the feature.*

This asymmetric notch is interesting, and probably the result of the properties of a charged, angled layer [184]. Essentially the incoming ions are no longer deflected to both sides equally, but follow the existing topography of the stop layer. This hypothesis is illustrated in Figure 4.16. Due to the rarity of processing to an angled stop layer, the manifestation of asymmetric notching was not foreseen before the process was tested on bevelled device wafers. Due to the scarcity of device wafers during the development phase of the manufacture process, a full-scale investigation was not possible to mitigate what is a minor negative effect. Future investigations could be considered to reduce the angled notching phenomenon, including simulations of incident ions on charged angular surfaces.

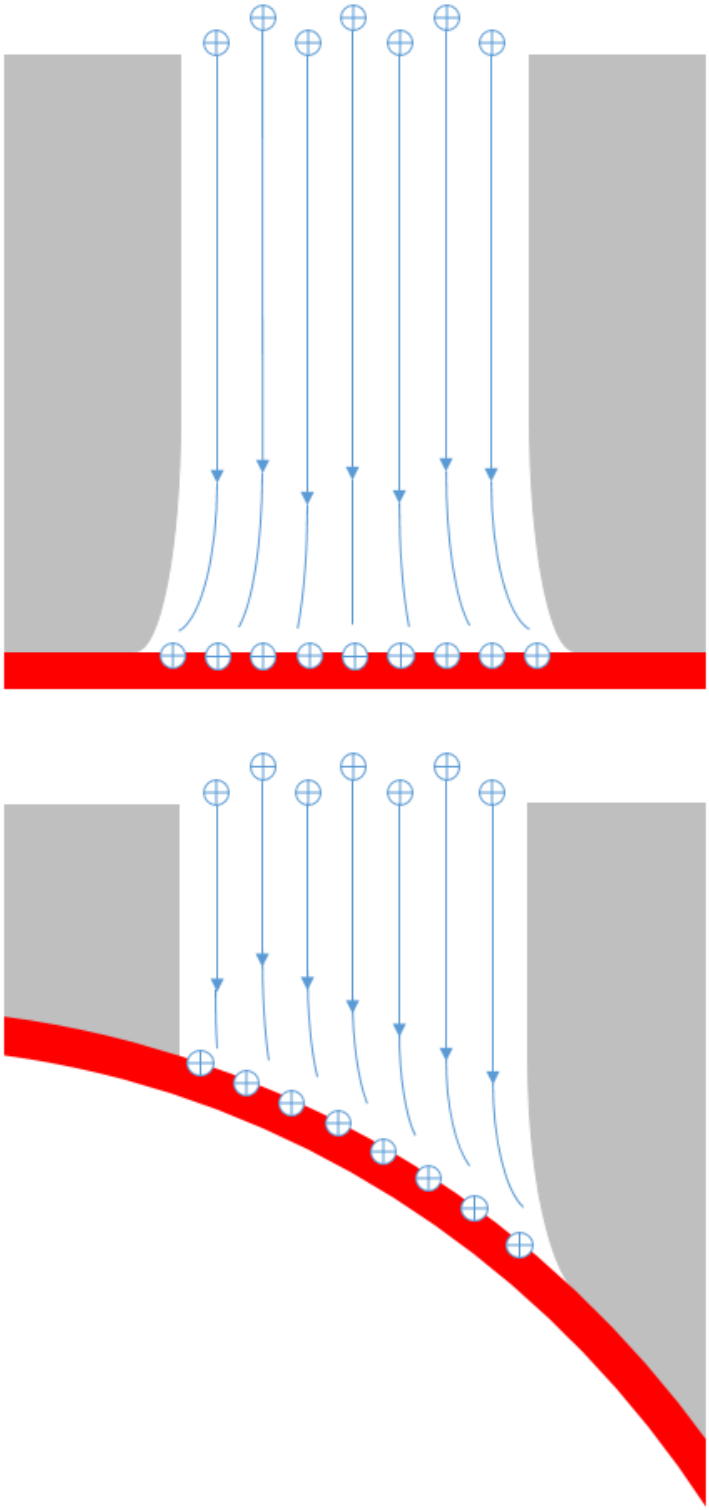

Figure 4.16. *Diagram showing the unique characteristics of notching on a bevelled surface. Silicon wafers are shown in grey and stop layers are shown in red. Positive ions are seen in blue, either as part of a charged layer or as an etchant plasma species. In the latter case, the direction and deflection are shown by blue arrows and lines respectively. The top diagram shows notching on a flat surface, while the bottom image shows the same effects on a bevelled surface.*

In addition to the angled notching, an effect specific to etching on a bevelled wafer was the limited thermal contact between device and carrier wafer. A comparative illustration can be seen in Figure 4.17, showing the reduction of heat transport. The practical effect of this was the lowered etch quality towards the feature base as seen previously in Figure 4.15. DRIE processes tend to be sensitive to thermal effects, with an increase in wafer temperature leading to less deposition to protect the sidewalls. Increased etch times exacerbate this effect, and the depth of the bore increases the risk of thermal-related damage during the etch. The quality of the etch had not been reduced to an unacceptable level; given future plans for a carrier-less process flow which would limit thermal based effects of etching, it was not deemed a reasonable use of time or material to try to improve the limited striations presented on the bevelled wafers. The final device wafers are processed with the result seen in Figure 4.15. When backlit, light can be seen through the wafer as shown in Figure 4.18. This demonstrates that the TSV has etched to the required depth without need for destructive analysis.

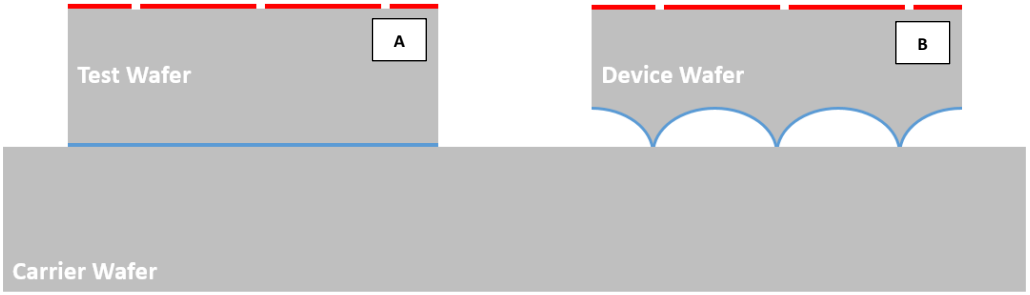

Figure 4.17. *Methods of bonding wafers for etching. The flat 'Test Wafer' (A) has full contact with the carrier, where the 'Device Wafer' (B) has limited interface between the wafer to be etched and the carrier wafer. The cavities severely diminish thermal transport between the two, allowing the device wafer to overheat.*

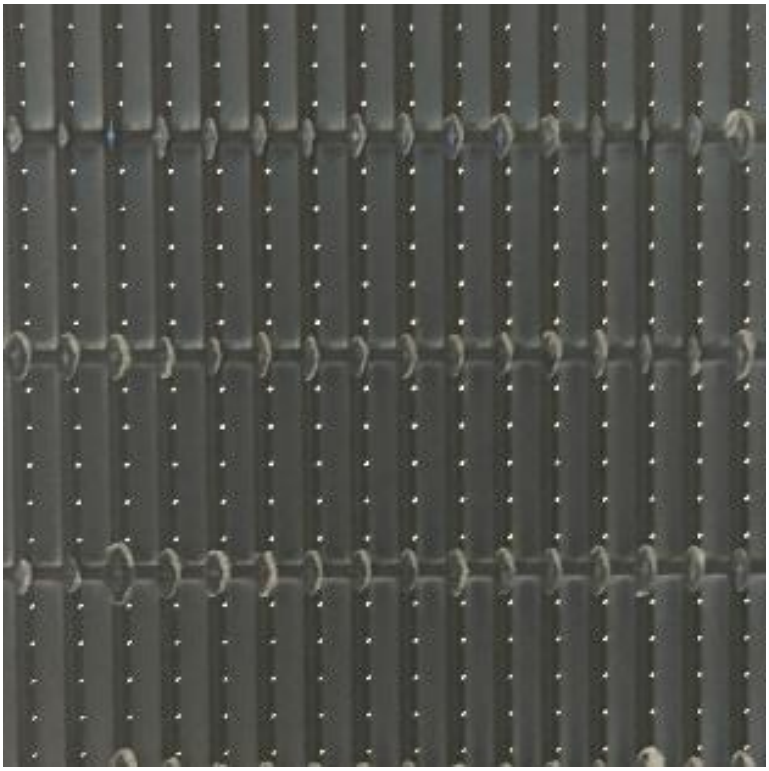

Figure 4.18. *Optical image of device wafer, processed with bevel and bore etches. The material at the die corners is the Crystalbond 555-HMP and demonstrates the very limited surface area available for thermal transport between carrier and device wafers. The light visible through the TSV shows that the bore etch has been completed to the correct depth for hollow microneedles.*

4.5 Conclusions

The bore etch has been successfully developed to facilitate fluid flow through the Silicon microneedles – one of the key benefits to this novel production flow. This was achieved by conceptualising and optimising an extremely deep TSV etch on current generation DRIE machine.

Challenges presented by this application included the significant depth, targeting twice the depth of similar etch types in these features was the primary concern as depth increases are non-trivial. In tandem with the depth, the avoidance of AR related damage and potential limitations was key including the control of the etch profile. Ramping was used during the

process to increase the depth while minimising damage and maintaining straight sidewalls, but introduced complicated interdependent parameters with step times, chamber pressure, and platen power all varied across the process length. Reduction of the notch was first developed on test wafers to preserve device material, and transferred once an acceptable level of notch was achieved. The challenge presented by wafer heating effects is possibly the only one that was not controlled, but rather accepted as an unfortunate consequence of the current carrier wafer regime. In future it will be possible to eliminate carrier wafers and control the device wafer temperature directly. However, the damage was not excessive, and the time and wafers that would be needed to fully develop a carrier-less process flow does not fit into the conception and optimisation development stage that this project currently occupies.

The difficulties with this depth in the 'Via' feature type are many and well documented, which highlights and showcases the results achieved here with excellent sidewall quality. As a standalone etch on a flat patterned test wafer, the depth far exceeds the etch depth presented by previous 'Ultra Deep' (UDRIE) applications. The Rapier™ module results were in line with expectation and DSi-v™ results were comparable. The maximum depth achieved on the DSi-v™ was 1365µm, but showed some breakdown towards the feature base. The best results on the Rapier™ exceeded 1150µm with extremely clean sidewalls. The depth was limited by the 1.2mm wafer thickness and further increases to this may be possible if required. For this development, the benefits to factory footprint and tool purchase cost overrides the superior etch quality, and the DSi-v™ was chosen as the correct module type going forward. However, it must be stressed that this is primarily because the etch results were satisfactory with the DSi-v™, and cost reduction for manufacturing was secondary to overall etch quality. For future developments of the Bore etch process as a standalone application, a Rapier™ chamber would be recommended.

Evaluation of the bore process etching down to a stop layer was completed on flat test wafers. The result exhibited notching on the PR stop layer, due to charging of the layer and subsequent deflection of etchant ions. The issue was resolved by the use of LFr platen power as opposed to HFr, and the reduction of the platen Duty Cycle, both of which allow the charge on the stop layer to dissipate and reduce the deflection of incoming ions. The combination of these two process changes reduced the notch from 21μm to a negligible size.

Further to this, integration between the bevel and bore etches was completed. The notching that was eliminated on a flat stop layer returned on the bevel stop layer, due to the physical properties of charge accumulation on the angled surface. Though visible, the notching was not device-critical at the level observed because of the investigation and optimisation carried out on the flat stop layer test wafers. With the bore successfully processed on the bevelled device wafers, the latest step in the production flow that allows the creation of hollow silicon microneedles manufactured using only plasma etch processes is demonstrated. Device production wafers are processed using the final bore conditions in the previous section, and are then prepared for the next step in the production flow, the Shaft etch.

Chapter 5

Shaft Etch Development and Integration

This chapter will discuss the development of the final silicon etch process in the microneedle fabrication process, including test wafers and integration with previous steps. Examples of solid and hollow microneedles will be presented.

5.1 Introduction to Shaft Etch

The shaft etch is the final step performed in the fabrication of microneedles, and provides the vertical height to the MN. In other examples of microneedles, the most common forms consist of either a sharp top surface to enter the skin but no shaft [14, 74, 75, 110, 144], or only a shaft (with or without a sharp 'rim') [72, 73] which provides a usable length but has potential issues with initial insertion. In some cases, efforts have been made to sharpen existing MN [73], but the work undertaken in this project results in a sharp microneedle with an integral shaft using only dry etch processing [6, 149]. The height of the shaft etch controls the insertion depth for the final MN. If the penetration height of the microneedle is too short, it will not be able to break through the *stratum corneum* and will therefore be incapable of transdermal injection.

The main challenge for this application is maintaining a relatively straight profile at the significant depths required (>700µm). This is important as a profile that leads to a reduced base width would introduce mechanical weakness and a possible fracture point in the structure [151], especially given the decreased wall thickness associated with the hollow architecture. Additionally, having a larger pillar thickness at the top of the feature would result in an overall shape resembling an arrowhead, leading to a higher possibility of the microneedle becoming lodged in the skin.

In this chapter, wafer preparation will be described and etch targets defined. Initial process tests on flat wafers enable study of the etch results independent of effects from the bevelled surface. Once optimised, the process is transferred to bevelled device wafers. The shaft etch is processed in combination with the bevel etch to form solid MN, and bevel & bore etches to form hollow MN.

5.2 Shaft Etch Method and Metrology

5.2.1 Wafer Preparation and Photolithography

Lithography steps were completed at Swansea University by Olivia Howells. To prepare for shaft patterning, wafers are placed in a bath of TECHNISTRIP P1316 heated to 70°C, and agitated until clean.

Photoresist was applied to the wafer frontside using a SUSS MicroTec AS8 spray coater. A solution of acetone and AZnLof2070 photoresist was used for spraying, with the acetone acting as a thinning agent and subsequently evaporating from the wafer surface due to the heated chuck in the AS8. PR was baked at 130°C for 10mins on a hotplate before being transferred to a SUSS MicroTec MA8 for UV mask patterning. Excess resist was removed using AZ276 developer. Sprayed resist must be used in this case due to the topography of the wafer surface.

Crystalbond 555-HMP adhesive was used to bond 100mm test wafers to 150mm carriers. The adhesive has a thermal flow point of 66°C which is achieved by placing wafers on a hotplate and applying the Crystalbond to the wafer backside, before being placed onto the carrier wafer and cooled ready for processing.

It is important to note that this development was undertaken after the Bevel had been optimised, and as such benefited from the investigation detailed in Chapter 3 Section 3.3 to improve the non-uniformity of high open area etches. As the Shaft etch is also a high open area application, process testing was carried out using the sacrificial Si around the device wafer as described in Chapter 3 Section 3.3.3 to mimic the effects of a uniformity ring.

5.2.2 Etch Targets

A depth target of 700µm was set in order to breach the *stratum corneum* and place the central bore far enough into the skin to achieve transdermal injection. Although the *stratum*

corneum is typically <20µm thick [123, 124], the elasticity of the skin layers necessitates a much longer MN – ~400µm would be sufficient to enter the skin consistently with a solid MN. The depth target was increased here as the bore hole sits approximately halfway down the bevel. Because of this, the depth of the shaft must be larger to facilitate the penetration of the full bore opening beneath the *stratum corneum* allowing injection to a region that would permit full diffusion of the injected fluid.

To avoid the arrowhead shape described in Section 5.1 the etch profile must be controlled; in a model situation, a vertical profile is ideal. However, in practice a 90° profile is not possible. For shaft etches, the main driver of profile angle is the temperature of the device wafer. Silicon etching is an exothermic chemical reaction [15, 17, 18], and with the topography of the pillar providing little opportunity for heat dissipation this increases the device wafer temperature. At higher temperatures, the deposition step becomes less effective and tapers the profile. It was for this reason that the realistic minimum profile target of 88° was set.

General quality of post-etch wafers was also a key concern. The wafers must be of sufficient cleanliness to be used for medical applications, so it follows that the etch must be free from defects that may lead to particle formation. Smooth sidewalls with no striations or significant damage are required, and in addition to this a clean etch front is necessary which avoids the formation of 'silicon grass' [15, 16]. In this context, grass is micro- or nano-scale spikes that protrude from the feature base, illustrated in Figure 5.1. Formation of grass is usually the result of micromasking, insufficient deposition clearing, or ineffective chemical etch. It is particularly common in this type of high open area, large feature application; the abundance of Si to be etched by limited available etchant can lead to grass formation.

Figure 5.1. *Illustration of features, showing (A) a cleanly etched feature with a smooth base; and (B) a feature exhibiting a typical manifestation of grass.*

5.2.3 Metrology and Analysis

Shaft etch wafers were primarily analysed by cross-sectional imaging in a Zeiss SEM. Wafers were cleaved along the silicon crystal plane, and loaded into the SEM for imaging and measurements using the integrated metrology available on the Zeiss SEM. Analysis in this manner provides both qualitative and quantitative results. Optical images were limited in their use for this structure but can provide a reasonable way to image at lower magnifications. They are also beneficial in that optical imaging is not destructive, so can show qualitative results without sacrificing a device wafer.

5.3 Shaft Etch Development and Results

5.3.1 Etch Module and Initial Results

A SPTS Technologies Rapier™ module was chosen to start the shaft etch development. This was due to key requirement of profile control, as the secondary source RF power and secondary gas flows on the Rapier™ provide additional process control over single source etch modules which may help in tuning the profile [164].

Initial tests for the shaft etch were performed on flat test wafers, which saves device wafers from being consumed in development and also separates results of the etch process from the effects of combining processes in the production flow. 100mm test wafers were patterned as described in Section 5.2.1, and mounted to a 150mm carrier with sacrificial silicon around the test wafer ready for process.

A switched process was used for the shaft, the basics of which are described in Chapter 2 Section 2.5.4. Use of the SPTS Technologies MORFLEX [178] software for parameter ramping could also provide benefits, particularly in relation to the profile control; the principles of MORFLEX's operation are explained in detail in Chapter 4 Section 4.3.1.

Images from Test 1 can be seen in Figure 5.2. For the initial tests, a shallower depth of 400µm was targeted to allow assessment and rectification of issues before attempting full depth etches of >700µm. As can be seen from the SEM images, the main problem for this first process was the formation of grass at the wafer edge. The roughness in the sidewall can also be a manifestation of the same root cause, i.e. insufficient deposition clearing causing micromasking, and both effects need to be tuned out. The feature at the wafer centre is etched cleanly to 400µm with well-defined scalloping and no damage; the challenge was to replicate the same quality at the wafer edge.

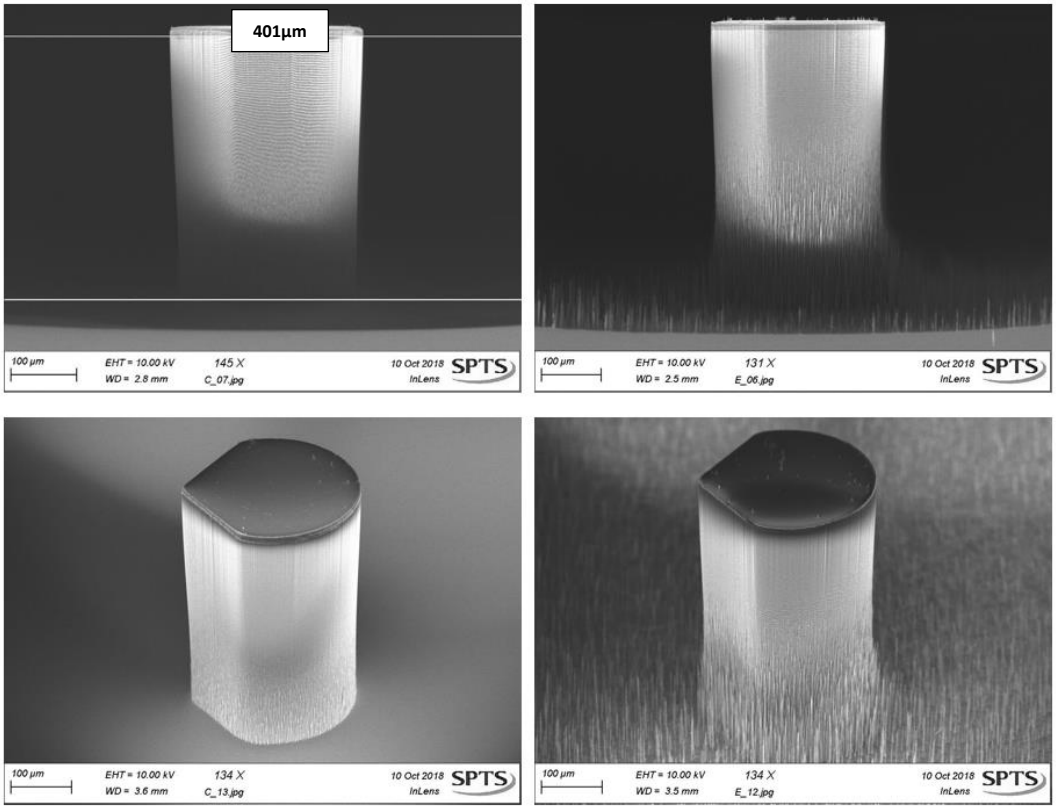

Figure 5.2. *SEM images of Test 1. The centre of the wafer is etched cleanly to 400µm. Grass is present at the wafer edge, and can clearly be seen in both the cross-sectional and oblique images.*

To counteract the effects that lead to grass, the E2 time was increased in Test 2. The intention with this process change was to provide a longer period of etching which would completely undercut any micromasking and effectively eliminate the grass. As can be seen in Figure 5.3, this had the desired effect on the grass, but the process is still on the edge of forming grass as evidenced by the striations in the sidewall at the edge.

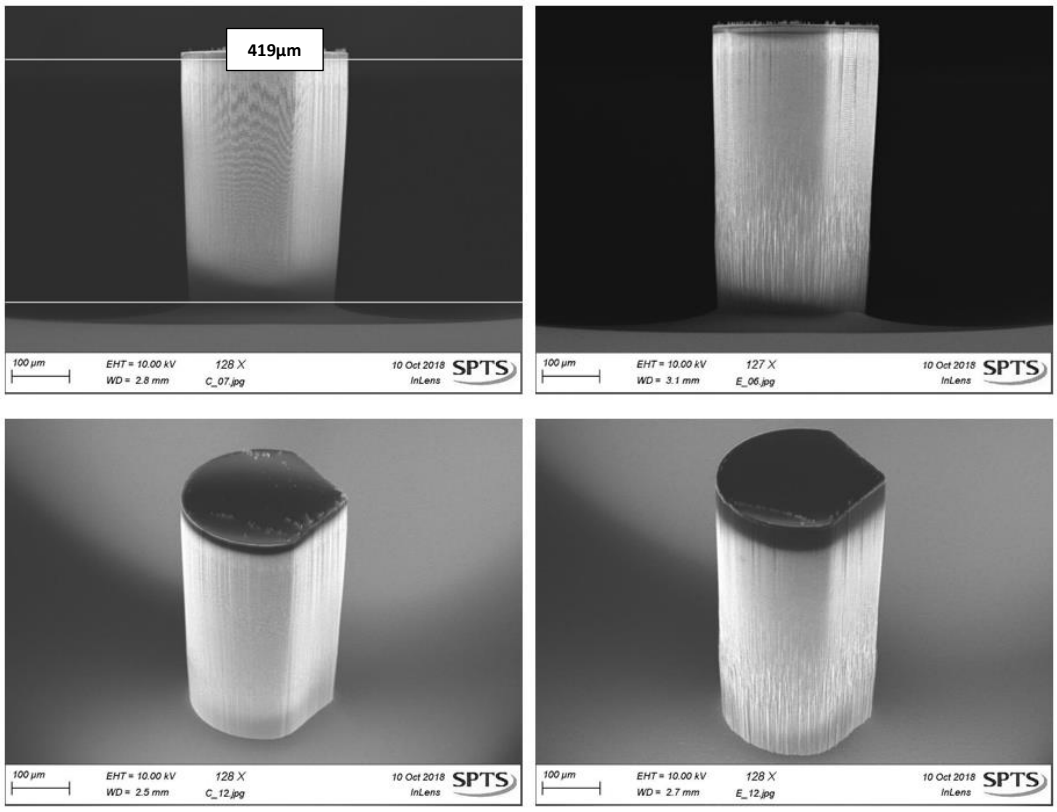

Figure 5.3. *SEM images of Test 2. The etch remains clean at the wafer centre, with the edge now exhibiting a clean etch front. However, striations can be seen towards the base of the shaft at the wafer edge.*

The loop number, and therefore total etch time for Test 2 was increased to push the depth closer to the target in Test 3. The resulting etch was shown in Figure 5.4 with numerical results in Table 5.1, and the most striking aspect of this result is the return of the grass around the feature at the wafer edge. The grass seems to be preceded by striations in the sidewall, which are also present towards the base of the shaft at the centre, implying that grass will form at that site if the etch is pushed to further depth. This is problematic for a potential device wafer, but equally from a development standpoint there are also a few issues with this process. Firstly, this result is 100µm short of the target depth; as mentioned, the grass would only get worse with the additional depth. Secondly, process tuning parameters to adjust this result have either already been explored (i.e. E2 time increase), or would cause

excessive tapering of the profile (i.e. platen power increase). Neither of these is good, and exploration of other process modules was warranted to see if the results could be improved.

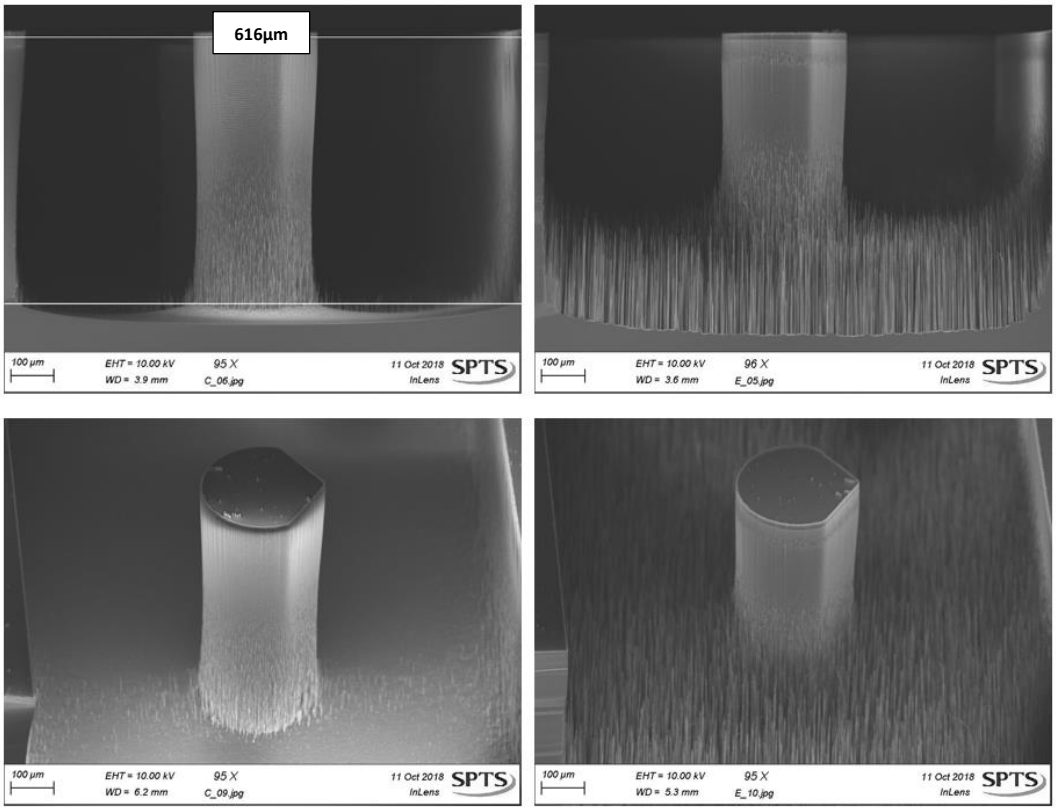

Figure 5.4. *SEM images of Test 3. Depth has increased to >600µm, but a large amount of grass formation is present at the wafer edge. The centre also shows the beginnings of grass formation.*

Parameter (Units)	Target	Test 1	Test 2	Test 3
Average Depth (µm)	>700	422	444	613
Etch Rate (µm/min)	None	4.8	4.9	4.6
Profile (°)	>88	88.8	87.9	89.2
Grass (µm)	0	48	0	273

Table 5.1. *Numerical process results from Tests 1-3 of the Shaft etch trials in the Rapier™ chamber. Etch step time was increased after Test 1 to address the grass formation, but resulted in a reduced profile in Test 2. Increasing the etch depth of Test 2 resulted in the return of significant grass in Test 3.*

5.3.2 Process Chamber Transfer: Rapier™ to DSi-v™

Due to the previous development of the Bevel and Bore etches, a logical route forward for the Shaft etch was to explore the DSi-v™ etch module. This decision was taken from a cost-of-ownership viewpoint. When etches in the process flow can be completed on the same module, then only owning one module provides a reasonable entry point for low-volume production.

To transfer the process to the DSi-v™, the starting point is taken from the recipe developed on the Rapier™. All parameters used were the same, with the exception of the secondary source power and gas flows which are not available on the DSi-v™ design. The result of this initial transfer, Test 4, can be seen in Figure 5.5 with numerical results in Table 5.2. With the same parameters as the Rapier™, the DSi-v™ has produced a much cleaner etch front, but tapers the shaft profile to a thinner base. While this in isolation is not a good result due to the poor profile, when compared to Test 3 the lack of grass is promising, and means that the developmental focus can be shifted towards profile control rather than cleanly achieving the required depth.

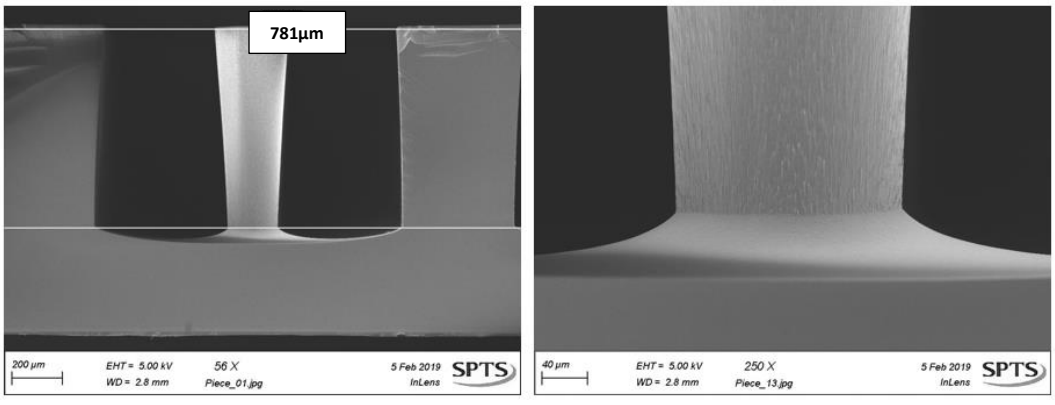

Figure 5.5. *SEM images of Test 4. The DSi-v™ shows a much cleaner etch to 780µm depth. The profile is very pinched towards the base, but the etch front is extremely clean.*

The DSi-v™ has a reduced chamber volume, and therefore a lower residence time. It takes less time to achieve the required etch pressure with the same gas flow as in the

Rapier™; this allows each step to reach the correct parameter values more quickly. This could explain the difference in the effectiveness of this process between the modules particularly given the high open area and associated loading effects as discussed in Chapter 3 Section 3.3.2, as the increased time spent at the correct pressure and flows for the etch step would be longer, reducing grass formation and enhancing the etch.

While it is possible that the grass could be tuned out in the Rapier™ process, the DSi-v™ provides a better result with the same parameters, and a wider process window. In combination with the previously mentioned benefits of using a single module type for all DRIE steps, development of the shaft etch was continued on the DSi-v™.

Subsequent tests focussed on the improvement of profile, with numerical results shown in Table 5.2 for Tests 4-7. Across these tests the platen power, E2 time, and SF_6 flow were all ramped down to achieve a profile of 87.5°. This was close to the target of 88° and demonstrated that the process is tuneable without the introduction of grass, as can be seen with the images from Test 7 shown in Figure 5.6.

Parameter (Units)	Target	Test 4	Test 5	Test 6	Test 7
Depth (µm)	>700	781	621	577	616
Etch Rate (µm/min)	None	6.9	7.1	6.8	7.0
Profile (°)	>88	86.6	86.7	87.2	87.5
Grass (µm)	0	0	0	0	0

Table 5.2. *Numerical process results from Tests 4-7 of the Shaft etch trials in the DSi-v™ chamber. Improvement of the profile is steady across the tests, but still short of the 88° target.*

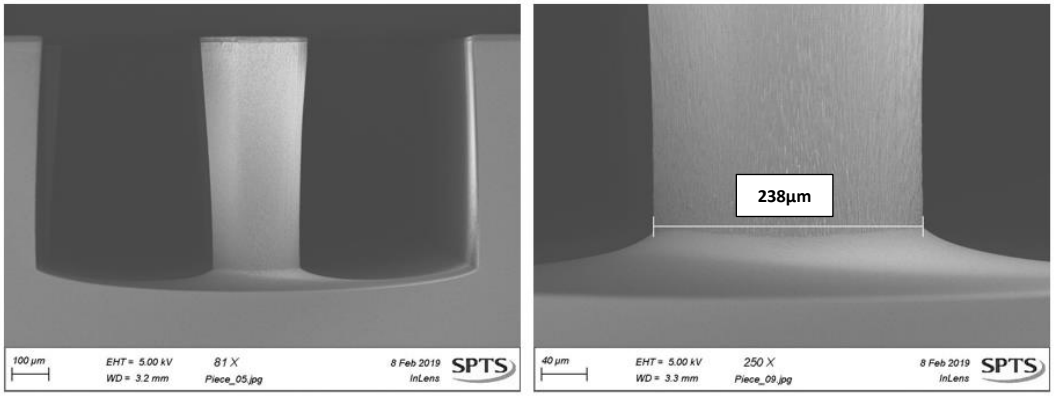

Figure 5.6. *SEM images of Test 7. Profile is improved from Test 4 and the base remains free of grass. Further improvements are necessary though, as well as increasing the depth.*

However, to achieve the target depth and profile more drastic process changes were considered for Test 8. With the E2 time ramped down, thermal build up in the substrate occurs at the start of the process more than the end. To combat this and the pinched profile that comes with excessive heat, the E2 time for Test 8 was fixed to the lowest level in the previous process. Removing ramping is not usually considered when tuning profile, but in this case controlling the wafer heat is the most important driving factor for profile. In addition to this, the loop number was increased to push the depth further and the ramps on platen power and SF_6 flow are changed to match the new loop number. The result of Test 8 can be seen in Figure 5.7, which shows a variable profile which is calculated using top and bottom CDs to be 89.8°; this is only because it narrows in the middle before widening again. The damage visible at the top of the feature is the result of mask recession, and is easily fixed by the use of a thicker mask.

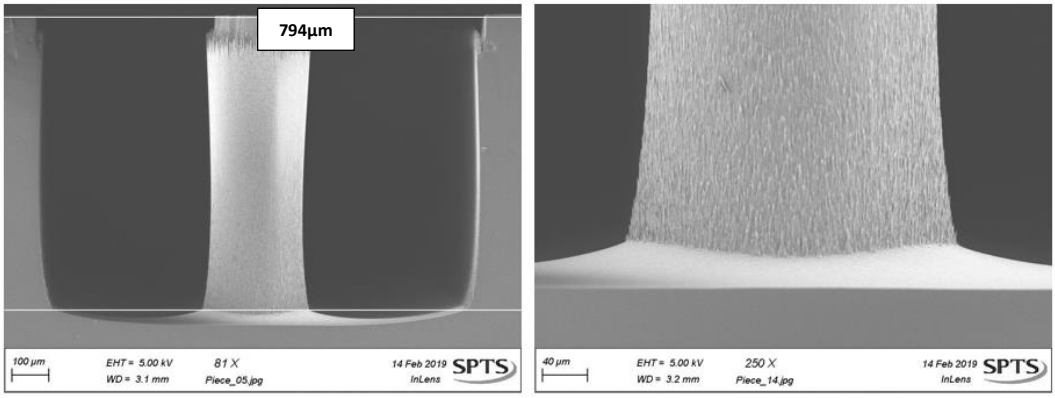

Figure 5.7. *SEM images of Test 8. Nominally a better profile, but this is due to the flaring at the base. Top damage is present, but only an artefact of mask recession rather than a process issue.*

Test 9 contained only minor changes from Test 8 aimed at giving a straight profile rather than the variation previously seen. The changes made to do this were to remove the ramping from the platen power and SF_6 flow; by ramping both down, at the end of Test 8 the process has neither enough platen power nor enough SF_6 to maintain a truly clean etch front, as evidenced by the formation of striations and widening profile at the base. The mid-way point of the Test 8 feature was both clean and has a relatively straight profile, so for this reason the mid-way values of the platen power and SF_6 ramps were chosen for Test 9. The numerical results can be seen in Table 5.3, with images shown in Figure 5.8. The changes had the desired effect, with the shaft exceeding the target depth and profile. Non-uniformity is excellent, and no grass is present at the feature base. This result was satisfactory to conclude development of this process on test wafers, and begin the transfer to device wafers.

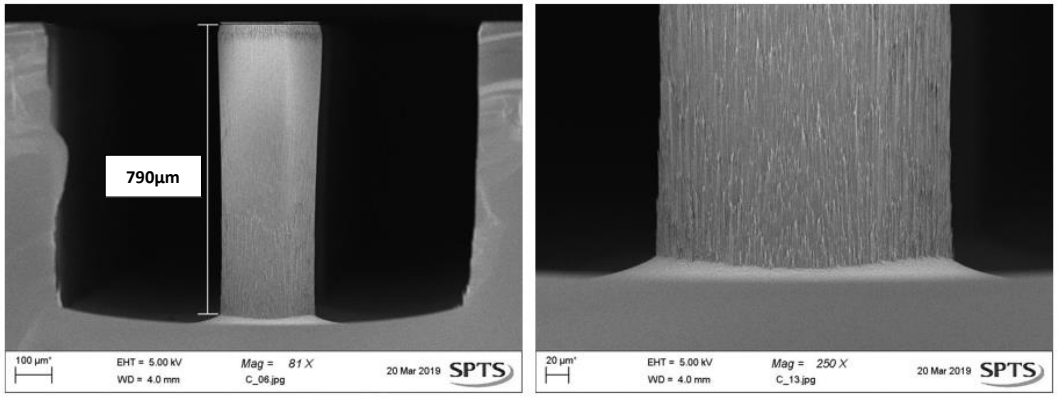

Figure 5.8. *SEM images of Test 9. The profile is near vertical, the base is free of grass, and the depth target of 700µm has been met and exceeded with a shaft height of 790µm.*

Parameter (Units)	Target	Test 7	Test 8	Test 9
Depth (µm)	>700	616	791	790
Etch Rate (µm/min)	None	7.0	6.2	6.2
Profile (°)	>88	87.5	89.7	89.0
Grass (µm)	0	0	0	0

{ REDACTED }

Table 5.3. *Numerical process results from Tests 7-9 of the Shaft etch trials in the DSi-v™ chamber, including key process changes. Depth has been increased to beyond the target, and process changes have had the intended effect on profile.*

5.4 Process Integration: Bevel and Shaft

5.4.1 Initial Combination Tests

The shaft etch for devices was completed on the bevelled wafer frontside, described in Chapter 3. To prepare bevelled device wafers for the shaft etch, any PR or etch residues were removed by submersion into a heated bath of TECHNISTRIP P1316. Coating of the photoresist was completed by the SUSS MicroTec AS8 spray coater, as described in Section 5.2.1. This

method of masking is preferential to spin coating in this case due to the significant topography present on the wafers; spin coating works well for planar surfaces, but would not provide a conformal layer over the bevel and could possibly leave large areas of the wafer totally unmasked. 100mm device wafers are bonded to 150mm carriers using Crystalbond 555-HMP in the same way as test wafers, described in Section 5.2.1. After completion of this, wafers are ready for process.

Due to the importance of material for biological testing as part of the wider project, each device wafer processed with the bevel etch becomes a valuable commodity. This is because the production of solid MN facilitates insertion testing, which can be completed without the bore and is required for the proof-of-concept experiments regarding skin penetration, essential to the final device effectiveness. As such, the material available for destructive testing (i.e. cross-sectional SEM images) was limited because barring a catastrophic wafer-level event the solid MN are still of use. This means that where possible, multiple process changes were combined using experience with plasma etching to achieve the best results; this had the unfortunate side effect of limiting the amount of data collection possible for the effect of individual parameters and trends as many occur simultaneously and runs cannot be directly compared.

Preliminary testing of the shaft etch on the bevelled surface was completed with an oxide mask. This was due to the increased selectivity given by hardmasks over photoresist for silicon DRIE applications. To achieve this, bevelled pieces were coated in a layer of Silicon Oxide (SiO_2) using a SPTS Technologies Ltd Plasma-Enhanced Chemical Vapour Deposition (PECVD) system. To open the oxide hardmask, PR was deposited on the wafer surface as described above and patterned with the shaft layout. An ICP chamber was then used to etch the oxide layer, before the pieces were mounted for shaft etch tests in the Rapier™, as the initial tests for this development occurred before the transfer of other processes to DSi-v™.

The best process available from the flat test wafer development was used to etch the structures, and the result can be seen in Figure 5.9. The open silicon was severely micromasked, and pre-etch SEM images of the surface show why – the oxide had not been fully cleared from the silicon surface, leaving mask on the surface. This was due to the ineffective etching of the oxide, because the ICP was not designed to etch oxide. In the absence of a dedicated option to open the hardmask layer, the decision was taken to begin development of the shaft etch using only a thick PR mask.

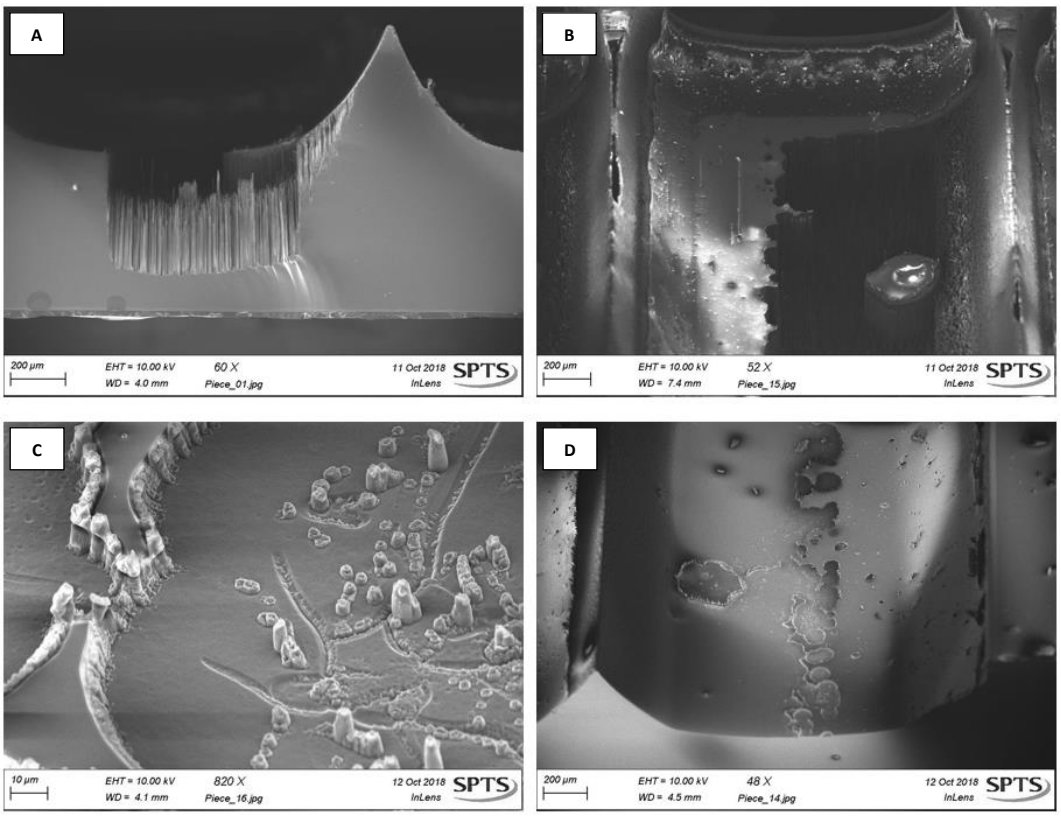

Figure 5.9. *(A) Etch test with a Silicon Oxide mask. (B) Angled view of the etched surface and remaining mask. (C) Pre-etch angled view of wafer top surface showing open silicon and Silicon Oxide mask. (D) Close-up view of wafer surface showing remaining material.*

Testing of the shaft etch with a PR mask on bevelled device wafers was completed using wafer pieces from the bevel development. This was for the same reasons as mentioned above, device wafers are scarce and valuable so any opportunity to test the process on used pieces is beneficial for initial investigations. In this case, the pieces used were from the

Rapier™ to DSi-v™ transfer of the bevel process, shown in Chapter 3 Section 3.3.5. As such, Test 10 was processed with the pre-etch 'flat top' topography seen in the left image of Figure 5.10. The result of etching the shaft on this type of bevel can be seen on the right of Figure 5.10, with good results but some obvious negative effects from the combination of processes. In general, this is a good starting point process that requires some tuning to address the issues. Before this development was continued, it was beneficial to analyse the different bevel topographies from the shaft perspective.

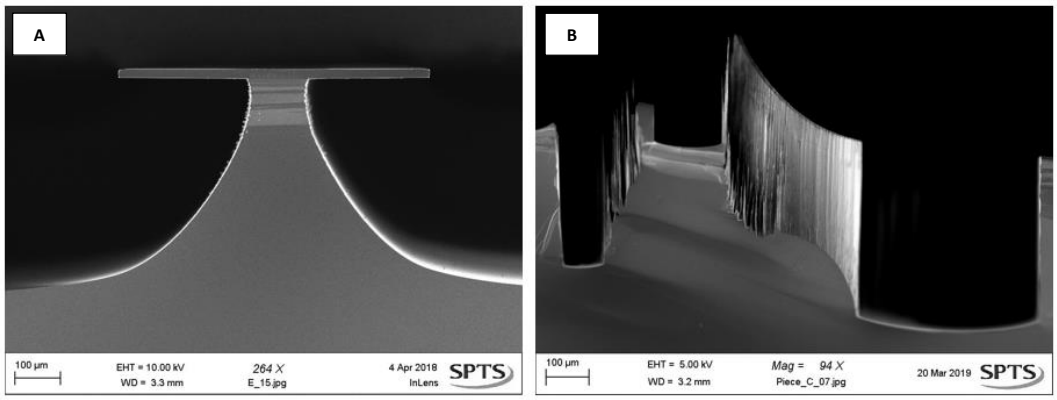

Figure 5.10. *(A) Flat top bevel used for initial combination tests. (B) The first result of the shaft etch performed on the bevel surface.*

In Chapter 3 Section 3.3.6, the pointed bevel shape was shown to have benefits for mask patterning. By etching the bevels to a pointed shape, the central point is in a consistent place for the whole of the wafer, as shown in Figure 5.11. This design mitigates for variations in lateral etch; although this metric had been significantly improved, it still has an effect on the fabrication of the MN, which was minimised by totally undercutting the mask to create a pointed bevel. As well as improving the patterning yield, the pointed bevel also has theoretical benefits when compared to the flat top after the shaft etch. Figure 5.12 illustrates a comparison of the two bevel topographies when processing the shaft etch, and with the flat top shape to the bevel the usable height of the MN is reduced. With this established, the shaft etch development continued by using pieces from a wafer with a pointed bevel.

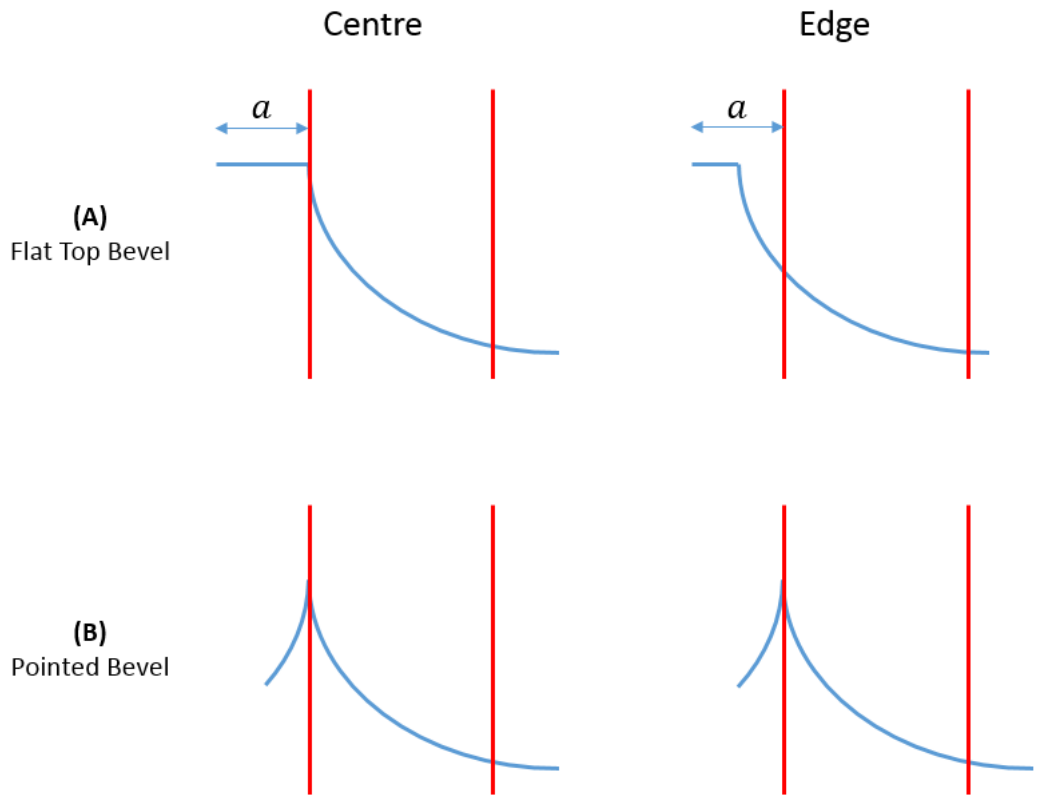

Figure 5.11. *Comparison of shaft patterning regions (red lines) between the flat top bevel (A) and pointed bevel (B). The pointed bevel provides a more consistent placement of the shaft on the bevel across the wafer.*

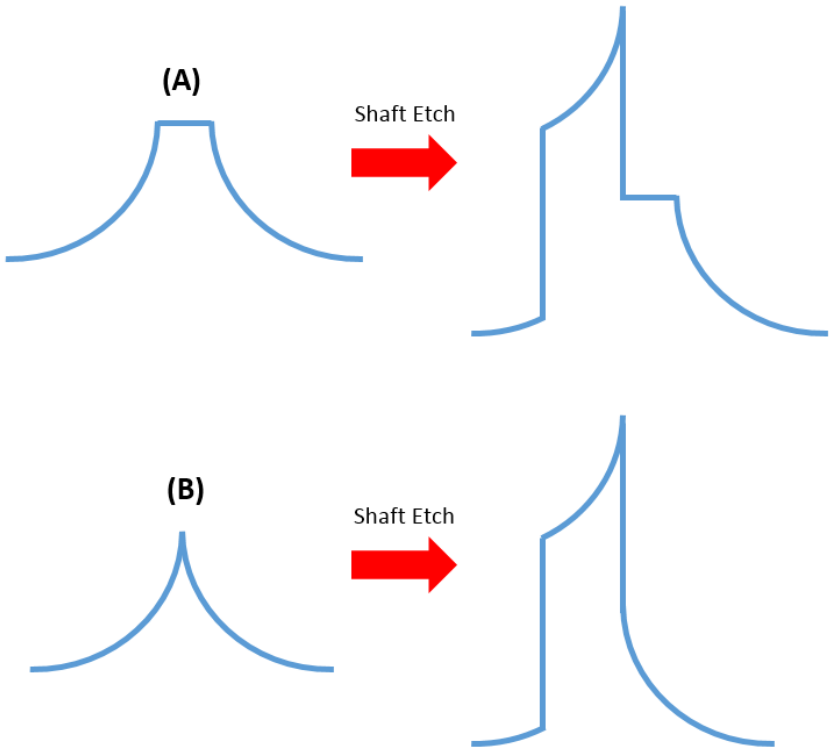

Figure 5.12. *A graphical representation of the expected difference between etching the shaft on bevels with flat (A) and pointed (B) topographies.*

To transfer the shaft etch to the pointed bevel, pieces from the bevel development in Chapter 3 Section 3.3.6 were coated with the shaft pattern as described above. For initial testing, a 400µm depth was targeted to analyse the etch independently of depth related issues. The result of this, Test 11, can be seen in Figure 5.13 and showed very good results. The shaft profile is straight and the etch front is clean, with the exception of some minor grass formation on the steeper portions of the bevelled surface. The result here shows a reasonable representation of the aims for the final form of the microneedle, albeit at half depth with no central bore.

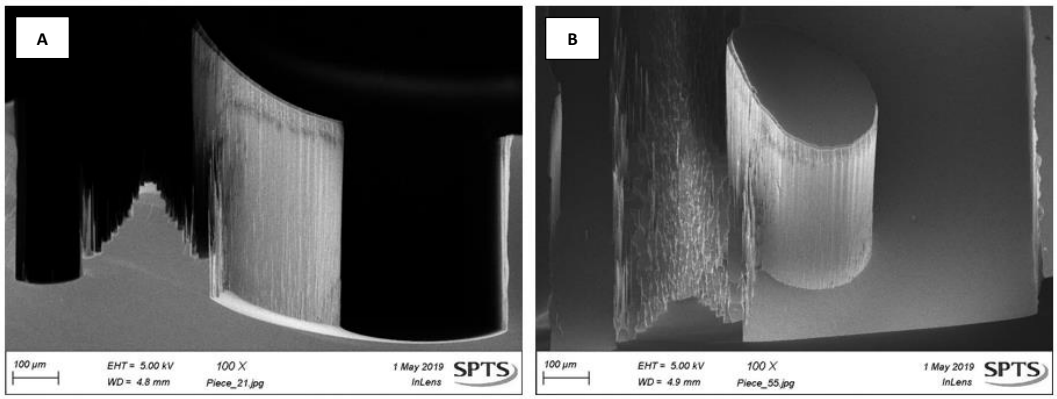

Figure 5.13. *Shaft etch processed on a pointed bevel. Image A shows the cross section used for analysis, with the half-depth etch showing a clean etch front and good profile of 89° at 445µm depth. Some minor grass is present on the angled bevel as can be seen on the left of image B.*

Following on from this half depth test, the next logical step is to increase the etch depth. Another bevelled wafer piece was prepared in the same way as Test 11, and processed with more loops to target >700µm depth. SEM images from Test 12 are shown in Figure 5.14, and immediately it can be seen that there is a micromasking problem that was not present in the previous test. As the roughness extends above the level seen in Test 11, it can be reasonably assumed to be an effect independent of the etch process, and instead stems from some variation in the surface or patterning between the tests. To identify the root cause(s), further investigations were devised.

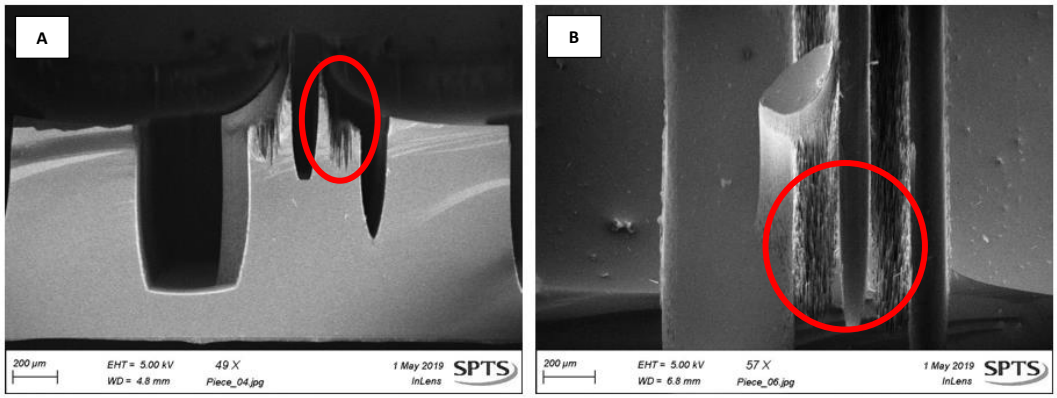

Figure 5.14. *Result from the extended Shaft etch time in Test 12. Images show the cross section (A) and angled view (B). Significant micromasking is present and highlighted in the red ellipses, indicating a pre-etch masking issue.*

5.4.2 Investigation of Result Variations

Initial investigations into the cause of the grass and process result variation centred on the pre-etch masking quality. During the development of processes, this is the first possible cause that requires investigation when faced with unexplained process results, due to the variation that can be present with the masking quality. Like etching, photoresist masking steps require optimisation to provide a quality coating both in terms of total removal from areas intended to be open, and profile/thickness of masked areas. Figure 5.15 shows optical images of the shaft mask pattern on the bevelled surface. Evidently there are complications present when patterning on an angled surface compared to a flat surface, resulting in some areas of PR remaining where it is undesirable – this is likely due to the angle of the bevel causing an artificial increase in mask to the vertically incident UV photons, meaning ineffective removal of PR. To address this, development of the PR masking process was undertaken on bevelled wafers with Olivia Howells at Swansea University, primarily varying the UV exposure time and intensity. The resultant PR mask from the develpment is shown in Figure 5.16, and can be seen to be significantly improved from the previous pre-etch images. Figure 5.17 shows a comparison of the shaft etch processed on each mask type, and unfortunately the improvement in the masking hasn't completely eliminated the silicon spikes produced by micromasking events. Larger micromasking artefacts have been removed, but it appears some additional effect is controlling the finer micromasking/grass. Additional investigation is necessary to diagnose the cause of the grass and improve the etch result.

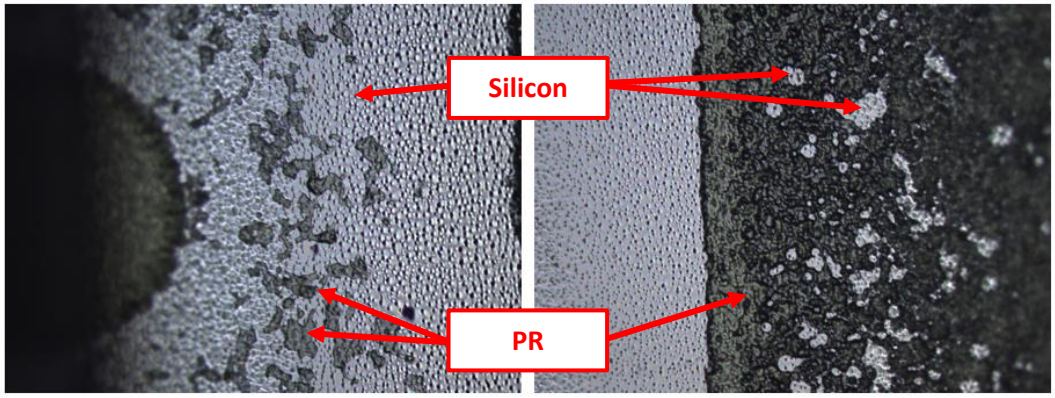

Figure 5.15. *Optical images of the shaft mask pattern on the bevel surface. Inconsistencies in the mask patterning are obvious, with both PR spots left where it is undesirable and open Si in areas that should be masked.*

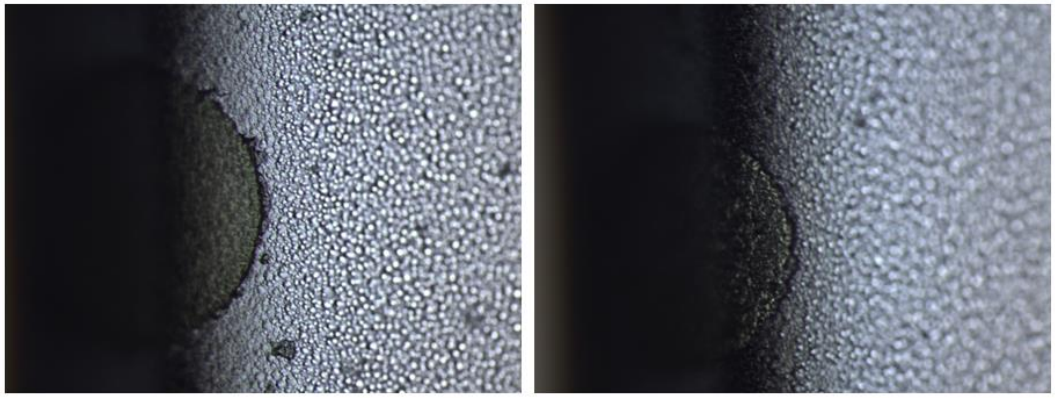

Figure 5.16. *Optical images of the improved shaft mask pattern on the bevel surface. Most significant masking defects have been addressed.*

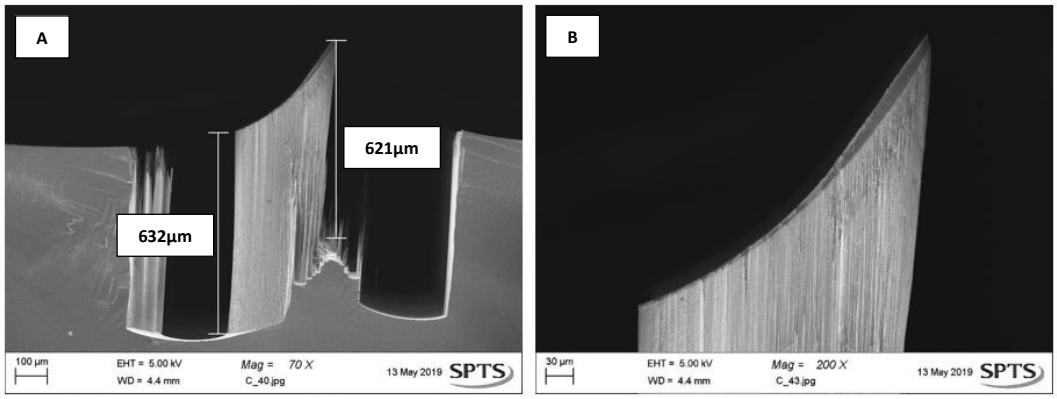

Figure 5.17. *SEM images of the shaft etch with the improved mask patterning on the bevel surface. Major micromasking evens have been reduced, but some finer grass remains around the feature. Image A shows the MN etched to a usable depth of 621µm, while image B is a higher magnification image of the MN tip. The top with of the feature is 322µm, with a tip angle of 29.6°.*

5.4.3 Non-Planar Silicon Smoothing

Continuing the investigation into the grass formation, cross-section SEM imaging of an un-masked bevelled wafer was undertaken. High-magnification imaging shows that the bevelled surface is not smooth, and in fact consists of jagged peaks approximately 2-5µm in height. Additionally, nano-scale roughness exists in the contours of these larger serrated peaks. Images can be seen in Figure 5.18. This significant surface roughness could be allowing PR to remain shadowed from the UV in the masking process, meaning that small pockets of PR exist hidden on the bevelled surface potentially leading to the grass seen during the etch. To test this, it was decided to explore the removal of the roughness to view its effect on the subsequent patterning and etching of the silicon.

For planar wafers, a common industrial technique is Chemical-Mechanical Polishing (CMP), a method that smooths wafer surfaces by both chemical reactions and mechanical abrasion [185]. Plasma-based smoothing processes also exist to remove roughness for planar surfaces [30], and are often referred to as CMP elimination as they remove the messy techniques used during the grinding of substrates for CMP.

For non-planar wafer surfaces such as the angled bevel, CMP can't be employed as the topography of the wafers means that the surface cannot be ground to a smooth finish while maintaining the desired features, and plasma-based smoothing is more difficult due to the angled surfaces. A novel plasma smoothing method for non-planar silicon wafers has been developed to effectively smooth the bevelled surface of the MN device wafers to the level shown in Figure 5.19. Roughness on the angled surface has been entirely eliminated, leaving a smooth surface especially in comparison to the pre-smoothing SEM images in Figure 5.18. The intricacies of this method cannot currently be discussed due to an ongoing patent submission not currently in the public domain (Application number GB2118859.4).

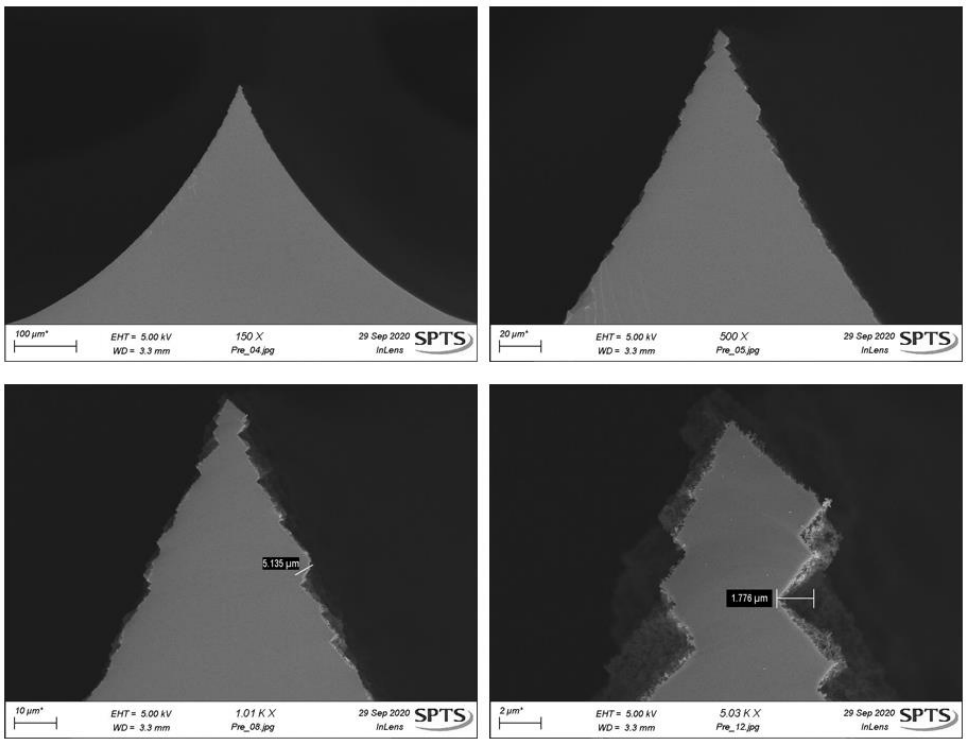

Figure 5.18. *SEM analysis of the pre-smoothing bevel roughness. The bevel exhibits micro-roughness up to 5µm with a jagged appearance, but also has much smaller nano-roughness all over the surface.*

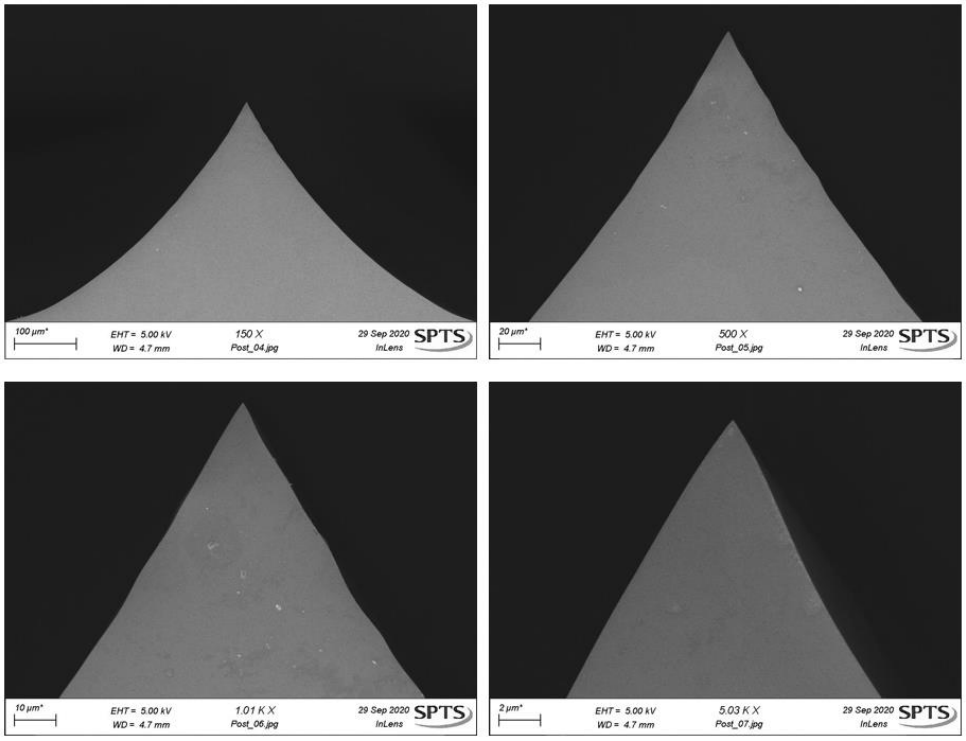

Figure 5.19. *SEM analysis of the bevel roughness after the novel smoothing process. Micro- and nano-roughness has been eliminated, resulting in a very smooth surface. The images are taken at the same magnification as the corresponding images in Fig 5.18 and are directly comparable.*

When etching the Shaft process on this smoothed bevel some smaller amounts of grass can still be seen, as in Figure 5.20 – although the grass was still present, it is to a lesser degree than previously observed. From this it can be concluded that the bevel roughness contributes to the formation of grass, but is not the sole cause of the micromasking seen during the rest of the development. Although there is still some minor grass, the smoothing of the bevel process does massively improve the consistency of the etch quality between runs, so is still a worthwhile step in the process.

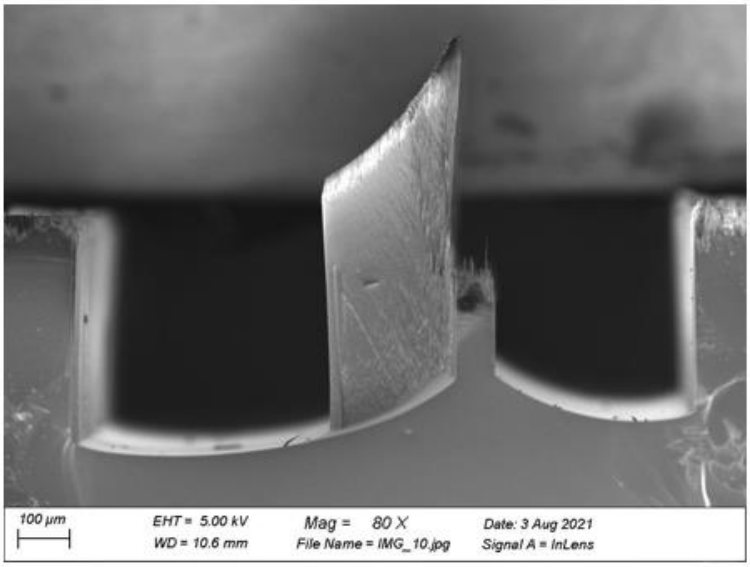

Figure 5.20. *SEM image of the shaft etch performed on the smoothed bevel surface. In general the etch quality is improved, though some minor grass remains. The MN is etched to a usable depth of 464µm, with a width of 243µm.*

Fundamentally then, the base level of grass after the shaft etch is not from either

a) the process, demonstrated by the clean etch on the flat test features;
b) the PR masking, as the finer grass showed minimal improvement with mask optimisations;
c) the roughness on the bevel surface, as some grass remained after smoothing the wafer.

To reduce the impact of the grass on the final MN form the process is altered to undercut the micromasking, but as described in Section 5.3.1 the negative effect of this is the decrease in profile. However, for this case the reduction of the grass is more important and the decrease in profile is acceptable at this level. The final form of the combination between the bevel and shaft etches, the solid silicon microneedle, can be seen in Figure 5.21.

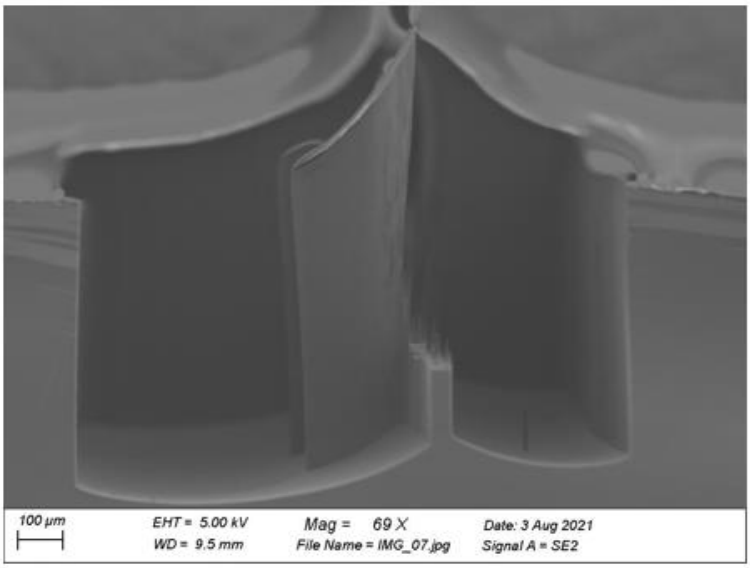

Figure 5.21. *SEM image of the shaft etch performed on the smoothed bevel surface with process changes. The solid microneedle form is shown with minimal grass at the expense of a slightly pinched profile. The MN is etched to a usable height of 731µm, with a top width of 263µm and base width of 223µm.*

5.5 Process Integration: Bevel, Bore, and Shaft

To fabricate a full microneedle, the three etch processes developed were combined on the same device wafer as described in Chapter 1 Section 1.7. Care has been taken throughout the developments to integrate the processes that are adjacent in the production flow to ensure minimal complications at this final stage of device processing, with examples detailed below.

Section 5.4 describes the work carried out to produce solid microneedles by combining the bevel and shaft etches. To fabricate hollow microneedles, this process combination must itself be integrated with the bore etch. Chapter 4 Section 4.4 details the work undertaken to perform the bore etch stopping on the bevelled surface, and by executing the shaft etch on a bevel + bore etch device wafer, hollow microneedles can be produced. In terms of the full integration of etch processes, no additional complications were expected from performing all three process on the same wafer compared to the developments combining two adjacent processes. This is because if aligned correctly, the bore and shaft etching do not interact with each other. In terms of the wider process flow, the only additional concern was that the bore opening must be completely covered by the masking material during the shaft etch to prevent etchant species from uncontrollably damaging the internal bore sidewalls – care was taken to avoid this.

A full hollow silicon microneedle is shown in Figure 5.22, and can be seen to have the desired characteristics for insertion and injection; a sharp tip for facile penetration, a near-vertical shaft to a depth that allows breach of the *stratum corneum*, and a bore to facilitate fluid flow through the MN. These microneedles are produced in 1x5 arrays, but the SEM used does not have a low enough magnification to capture all 5 MN in a single image. In total, 259 of the 365 arrays on the wafer have all 5 MN functional, resulting in a 71% yield for this combination of processes.

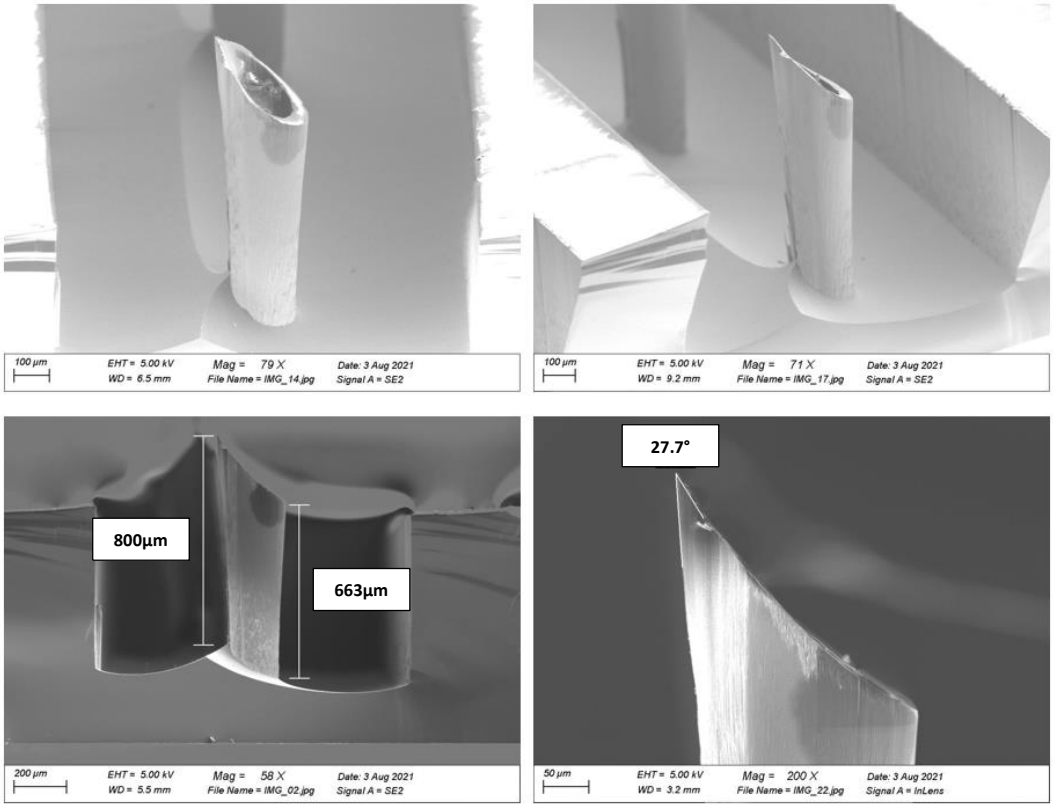

Figure 5.22. *SEM images of hollow silicon microneedles produced by plasma etching in the DSi-v™. The profile is slightly tapered, with a top width of 241µm and base width of 191µm, but the key elements of sharp tip (27.7°), central bore, and sufficient shaft height (800µm) can all be seen.*

5.6 Conclusions

A successful development of the shaft etch process has been carried out, allowing the hollow silicon microneedle to be inserted to the correct depth for transdermal fluid transport. Initially developed on test wafers, the shaft process was successfully transferred to bevel wavers to produce solid microneedles before the etch was completed on full device wafers to create hollow silicon microneedles.

Optimisations were necessary at each stage of the shaft etch development, with the main challenges being depth, profile, and grass. development began using test wafers processed in the Rapier™ chamber, with half-depth tests requiring recipe tuning to minimise

the grass formation at the feature base. Increasing the etch depth resulted in chronic grass at the wafer edge that could not be remedied without negatively impacting the sidewall profile. Development was moved to the DSi-v™ due to its advantages in high open area applications, and the transferred recipe showed much better results. Optimisation continued and the final result on a test wafer was etched to 790µm with a profile of 89° and no grass.

Initial combinations of the shaft etch with the bevelled surface showed promising results from an etch process perspective, but some issues with grass were present that were theorised to originate from the bevelled wafer or the patterning rather than the process. Tests were undertaken to investigate this and although not completely eliminated, the level of grass was reduced and the consistency of the post-etch results was improved to the point where process changes became effective in removing the grass. This was achieved through a combination of improved PR masking and the development of a novel plasma-based smoothing method for angled silicon surfaces.

Finally, the shaft etch was performed on a bevel + bore wafer to produce full hollow silicon microneedles, concluding the etch development work to optimise processes and fabricate MN using the novel manufacturing flow described in Chapter 1 Section 1.7 [6, 149].

Chapter 6

Device Testing, Project Conclusions, and Further Work

This chapter provides an overview of the proof-of-concept experiments undertaken to demonstrate basic device capability, before giving overall conclusions for the work undertaken in this project. Avenues of further work are discussed, with reference to possible benefits and challenges.

6.1 Preliminary Testing

Data for mechanical and biological tests was obtained in collaboration with fellow Swansea University student Olivia Howells, to provide qualitative information on the mechanical performance of the developed microneedles. The use of ex-vivo porcine and human skin tissue, for subsequent skin penetration testing, was approved by the local ethics committee, reference 08/WSE03/55.

Proof-of-concept mechanical testing was carried out to ensure that the MN would not fracture under thumb pressure insertion forces, for which the approximate normal force is <10N [78]. To assess the fracture force of MN, a Hounsfield/Tinius Olsen H1-KS compression analyser was used. The H1-KS utilises a 50N load cell descending at a rate of 4.5mm/s in order to determine the fracture force of a MN array. In these tests 1x5 MN arrays with shaft diameter 300µm were placed on the metal compression platform. Three repeat compression tests were completed, and results show that the MN array can resist a compression force of 22N before starting to fracture. This is over double the normal force applied in manual thumb insertion into skin. It should also be noted that the compression tests are conducted between two metal plates, and under real-world conditions penetrating through comparatively much more elastic skin it is likely that the MN would be able to withstand a higher insertion force [6].

The microneedles were prepared for testing by attachment to a Luer-lock compatible syringe adapter using glue around the edge of the die to prevent blockage of the bore holes, allowing flow through the MN and into the skin. Once connected to the syringe, the microneedle array protrudes vertically and insertion was accomplished by application perpendicular to the skin, using sufficient force to penetrate through the *stratum corneum* and into the lower layers until the MN baseplate rests on the surface of the skin. Depth of insertion is controlled by the height of the microneedles, permitting targeted injection

depths for different applications with varied shaft lengths without additional training. Injection is completed by controlled compression of the syringe plunger at a rate sufficient to facilitate fluid flow into the skin; if the solution is injected with too much force, the pressure can result in ejection of some of the fluid out of the skin. Removal of the microneedles is completed by simply withdrawing the MN array from the skin.

Preliminary insertion tests were conducted to prove the effectiveness of the MN skin penetration, and the potential for fluid injection into skin using microneedles. Initial insertion tests were undertaken using ex-vivo porcine skin to determine if the MNs effectively break through the *stratum corneum*. A 1x5 MN array was attached to a syringe by gluing it to a Luer-lock compatible syringe adapter, as can be seen in Figure 6.1 (Left). This was inserted into porcine skin using thumb pressure before being removed. To determine whether the *stratum corneum* was breached, the site of MN insertion on the porcine skin was stained with Methylene Blue (MB) – a hydrophilic water soluble dye that cannot independently diffuse through the intact *stratum corneum*. Any MB solution that does not have a path through the perforated *stratum corneum* can be removed from the skin surface using ethanol wipes. The sites of MN penetration are clearly visible after cleaning the surface by removing the excess dye. The penetration sites are stained with MB, which stains the skin layers beneath the *stratum corneum*, as can be seen in Figure 6.1 (Right) [6]. Penetration studies thus confirmed that the MN effectively break through the *stratum corneum* and allow substances (in this case MB) to penetrate in a 'poke and patch' application using solid MN.

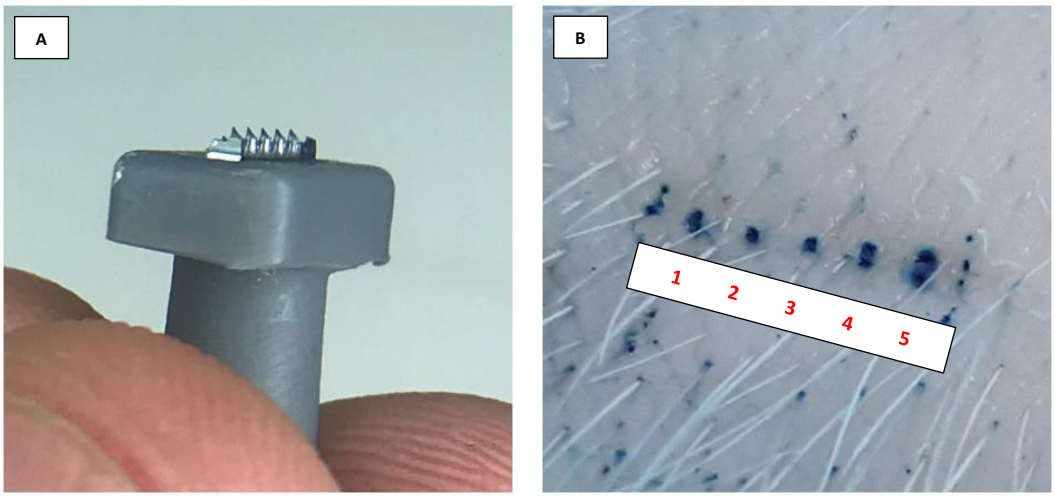

Figure 6.1. *(A) 1x5 microneedle array attached to a Luer-lock compatible syringe adapter. (B) The five sites of microneedle insertion into porcine skin, shown by the staining of the skin by Methylene Blue [6].*

To determine the depth of penetration, a solid microneedle array was applied to ex-vivo human breast tissue (local ethics committee reference 08/WSE03/55). Optical coherence tomography (OCT) was performed on the sample, and the image can be seen in Figure 6.2. The insertion channel created by the penetration of the microneedle is clearly visible, and exhibits the characteristic profile of the bevelled tip with its peak 400µm beneath the surface of the skin. Although the microneedle has an outer diameter of 300µm, the opening of the channel is 171µm due to the elasticity of the skin. The insertion channel depth of the bevelled tip at the shallowest position is 229µm, which is well beyond the *stratum corneum* which is typically <20µm in thickness [123, 124]. This suggests that once the microneedle is applied to the skin, the bore opening of a hollow MN would be beneath the stratum corneum and fully inserted into the epidermis indicating the effective penetration required for transdermal delivery applications.

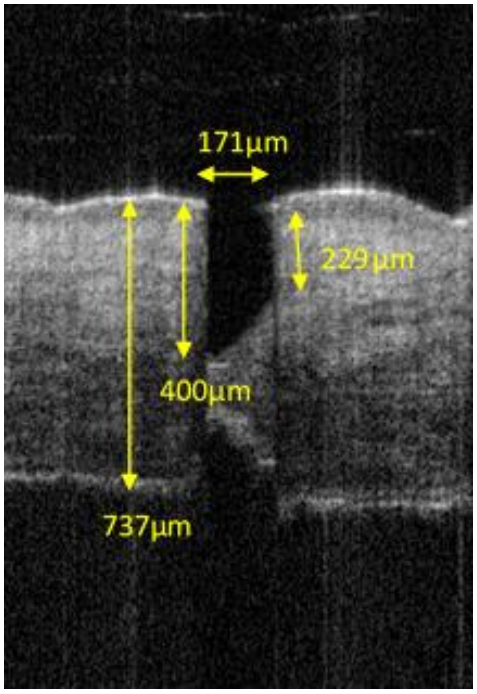

Figure 6.2. *Optical coherence tomography (OCT) image of ex-vivo human skin tissue after insertion and removal of the solid silicon microneedle array [6].*

To demonstrate transdermal injection, a hollow silicon microneedle array was attached to a syringe containing MB solution. Figure 6.3 shows the result of MN insertion and MB injection into porcine skin. The blue dots on the skin clearly show penetration of the MB into deeper skin layers, suggesting effective penetration of the *stratum corneum* and successful transdermal delivery of MB solution. It should be noted that the porcine skin used was quite old and thus very tough. Fresh skin is softer and it is suggested that MN testing on fresh skin would yield even easier penetration and more effective delivery.

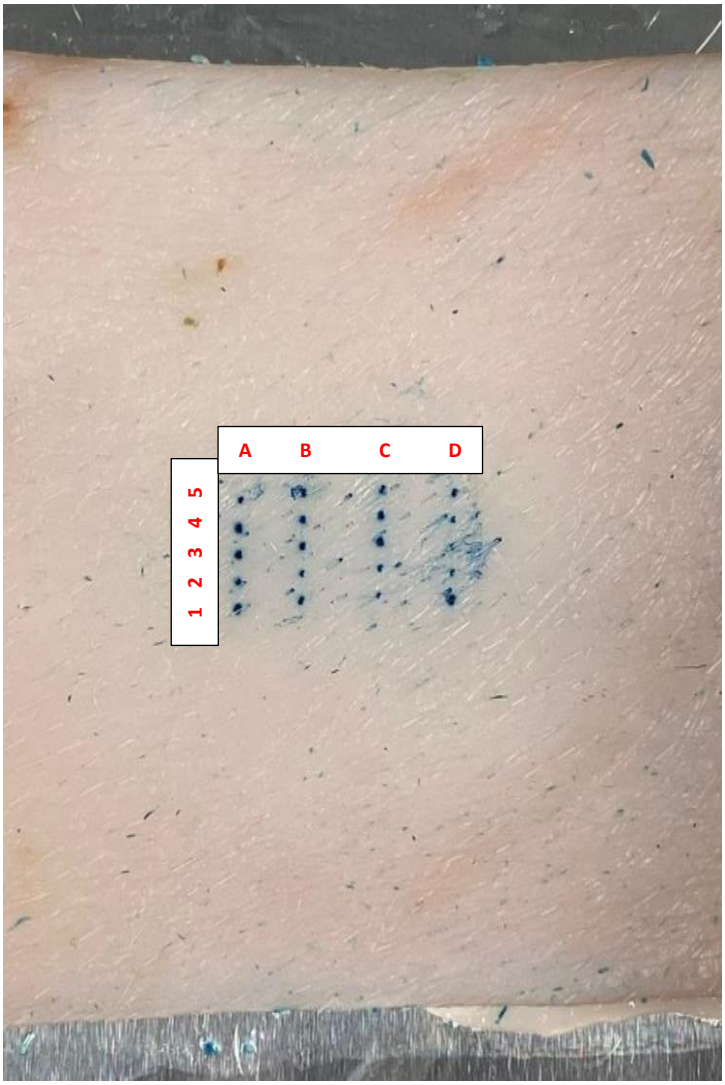

Figure 6.3. *Porcine skin showing the sites of Methylene Blue injection using hollow silicon microneedles. A single 1x5 hollow MN array was used for multiple applications, with individual needle injection sites (1-5) visible for each of the four repeated tests (A-D).*

Efficacy of transdermal fluid injection was tested by loading the syringe with DIL fluorescent dye and inserting the MN into porcine skin. 10µl of fluid is injected using a syringe pump, controlling the flow to a fixed injection rate of 10µl/min. A typical insulin pump flows at 10µl/hr [174], so the increased flow rate possible with MN shows the capability of hollow silicon MNs for biomedical drug delivery applications. Analysis of the injected porcine skin samples was conducted by imaging a histological cross-section of the MN injection site, Figure 6.4. This shows the DIL fluid at the base of the cavity created by the microneedle – visible due to the fluorescence of DIL at a wavelength of 565nm. The fluid was retained in

the MN channel, with no leakage onto the skin surface, indicating that hollow silicon microneedles can deliver fluid beneath the *stratum corneum* and could thus be used for transdermal injection.

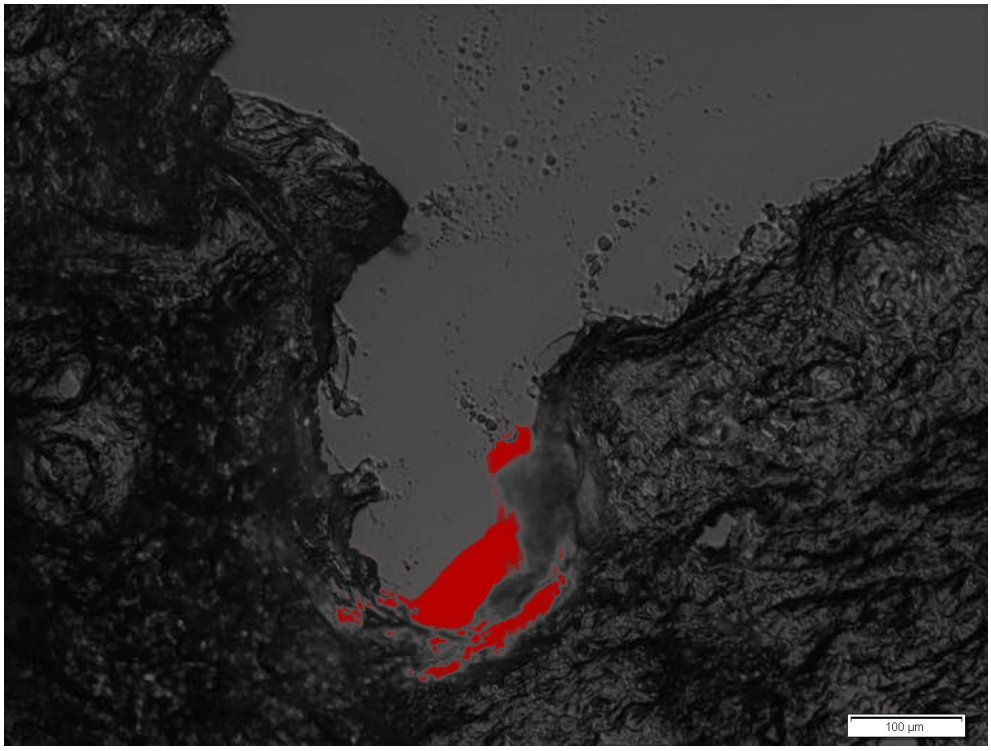

Figure 6.4. *Histological cross-section of a channel created in porcine skin by microneedle insertion. DIL fluid injected by MN can be seen at the base of the channel, in red, approximately 400µm deep [6].*

The tests conducted were intended to show proof-of-concept for the microneedle devices developed in this project, and have demonstrated the capability of hollow silicon MNs for effective penetration and injection of molecules into skin layers beneath the *stratum corneum*. Effective insertion was shown with disruption of the *stratum corneum*, and successful injection of fluid was evidenced by the retention of DIL fluid in the skin.

6.2 Project Conclusions

A novel fabrication process flow for hollow silicon microneedles has been developed and optimised. Each silicon plasma processing step has been completed on state-of-the-art DRIE machines to realise the intended microstructures.

Development of a single step Bevel etch process was initially performed on the Rapier™ system, during which a high depth non-uniformity (±11.3%) was observed. Investigations were undertaken to identify the cause and solutions to this uniformity issue. A critical factor of this uniformity variation was determined to be related to the local open area of a given feature, after an investigation involving the restriction of a test wafer's open area. This effect was confirmed by the comparison of experimental data to theoretical data generated by the area of two overlapping circles, demonstrated by Figures 3.4 and 3.6. The uniformity ring hardware typically used to mitigate this sort of effect was not an option due to the device wafers being carried on a larger wafer size, meaning that the uniformity ring would be too far away from the device wafer to have the impact required. Instead of this, pieces of silicon were bonded around the device wafer edge to simulate the uniformity ring, reducing the non-uniformity to ±6.8% with an identical process. Key process parameters were then identified and trialled, with the combination of removing the secondary source power and increasing the primary source power providing the best non-uniformity, ±3.83%. As this result was achieved using only the primary source, the etch was also tested on the alternative DSi-v™ etch system which exhibited a similar depth non-uniformity of ±4% but a much-improved lateral etch non-uniformity of ±2.76% (vs ±7.05% on the Rapier™). The improvement of the lateral etch non-uniformity increases the consistency of the patterning of the shaft etch by allowing the shaft pattern to be higher up on the bevel for more of the wafer, as demonstrated in Figure 3.11. The bevel etch was then further developed to create a point at all positions on the wafer, again improving shaft patterning consistency because

the point is always under the centre of the mask, also increasing the usable MN height as shown in Figure 5.12.

The realisation of the ultra-deep Bore etch was also initially developed on the Rapier™ system, targeting a minimum etch depth of 900µm. The initial switched starting process yielded results that were not of the quality required for the application, with significant roughness in the sidewall and a poor profile. This roughness could adversely affect the liquid flow through the bore. The sidewall roughness and profile were controlled by changing the platen temperature and gas flows, giving a very smooth result to 97% of the depth target. Increasing the depth resulted in an etch depth of 1157µm shown in Figure 4.6, a significant increase on previously reported UDRIE via etching. Although the Rapier™ is typically the system used for applications such as this, process development was transferred to the DSi-v™ system to align the bore etch with the previous work completed on the bevel etch. After initial transfer tests, a maximum depth of 1365µm was achieved, much deeper than the 900µm target and shown in Figure 4.9. Indeed, 1365µm is over twice the thickness of a standard device wafer and therefore the bore etch is at least double the height of standard Through Silicon Vias (TSVs). This extremely challenging etch depth was achieved in order to facilitate fabrication of MNs with a length of up to 1mm. To improve the chances of successful Bore process transfer to device wafers, tests were undertaken to understand and reduce the formation of notching on a flat etch stop layer. With the change from High- to Low- Frequency platen power and the optimisation of the platen pulsing duty cycle, notching on a flat surface was reduced from 21µm to a negligible level as can be seen by the comparison between Figures 4.12 and 4.13. Integration of the bore etch with the bevelled wafers was then undertaken, with the notching appearing on one side of the feature due to the charging of an angled surface (Figures 4.15 and 4.16) and an increase in sidewall roughness due to the restricted cooling of mounted wafers, though the quality of the result still yielded usable MN.

The Shaft etch development was also initially undertaken on the Rapier™, using flat test wafers to remove the possibility of any effects relating to performing the process on the angled surface of the bevelled wafers. The first tests showed good etch quality down to half target depth in the centre of the wafer, but exhibited grass formation at the edge of the wafer. The process was altered to remedy the grass formation at half depth, by increasing the E2 time. When increasing the process time to achieve increased depth, the grass returned to the edge features. Additionally, roughness obtained in the centre was evidence that increasing the depth further with this specific process would result in grass, as the sidewall roughness showed that increasing depth leads to increased micromasking in this regime. Because of this, process development was moved to the DSi-v™. With the same process, the DSi-v™ showed a much cleaner etch with no grass and tapering down to the base, indicating that the reduced volume of the DSi-v™ chamber does increase the efficacy of the etch step in the process. The developmental tests in the DSi-v™ focussed on the tuning of etch profile, with the largest changes coming with the removal of E2 ramping to combat the build-up of heat in the wafer, removal of SF_6 flow, and removal of platen power ramping to improve the etch front.

With each of the etches optimised on test structures, the shaft process was transferred to the bevelled wafers. Initial tests were completed on the flat top bevel before moving to the pointed bevels to increase the usable needle height, as shown in Figure 5.12. The first result on the pointed bevel was completed to half depth, and showed a clean etch front and vertical profile, Figure 5.13. Attempts to increase the depth resulted in a serious problem with micromasking originating from the etch surface. As there was no change in the process except increasing the process time, it was clear that the process was not the cause of the grass and further investigation into the cause of grass formation was necessary. Optical images showed inconsistent masking, and once this was fixed by optimising the lithography process to reduce resist residue after development, the grass was greatly reduced. However,

some grass still remained. SEM analysis of the angled bevel showed a rough surface of the order of 5µm in magnitude. To reduce this roughness, a novel plasma smoothing process for non-planar silicon was developed (patent application number GB2118859.4) with the pre- and post-smoothing results seen in Figures 5.18 and 5.19 respectively. Although this did not totally remedy the grass, it did improve the consistency of the masking and etching to a point where process changes became effective. It is suggested that lithography performed on smoothed surfaces produced more uniform resist development and thus reduced resist residue after development. Solid microneedle arrays were produced using the combination of these two steps (bevel, shaft), as shown in Figure 5.21. The bore etch was then integrated into the process flow using the knowledge gained from the development of the bore etch on both flat test wafers and angled bevel wafers. By integrating all three process steps on a single device wafer, full hollow silicon microneedles were fabricated as shown in Figure 5.22.

Preliminary compression tests confirmed sufficient mechanical strength under axial compression to sustain twice thumb pressure, and skin penetration studies showed effective penetration of the *stratum corneum* using skin insertion tests into ex-vivo porcine skin, with injection sites highlighted by methylene blue staining. Depth of penetration was analysed by OCT imaging of a microneedle insertion site ex-vivo human breast tissue which confirmed successful disruption of the *stratum corneum* and an injection depth up to 400µm using a 737µm long MN. Injection of fluid into porcine skin was demonstrated by skin penetration and subsequent injection of Methylene Blue solution through hollow silicon microneedles and also by imaging a histological cross section of porcine skin injected with DIL fluorescent dye using MN, where the DIL was shown to be located at the base of the insertion channel created by the injected microneedle. Using the controlled injection rate of 10µl/min, no leakage of the fluid onto the surface of the skin was observed.

6.3 Discussion

6.3.1 Applications and Alternative Designs

Development of specific biological applications was not the focus of this project, rather the intention is to collaborate with other research groups by providing MN arrays for testing of suitability for a variety of applications being developed by the individual parties. The focus of this work was to optimise the fabrication sequence to allow low-volume manufacturing of MN to be completed, tailored to the specific needs of the enquiring group. In future, the ramp up of production may be possible to enable mass fabrication and distribution of these devices, meaning that the steps developed needed to be compatible with that environment.

If required, the MN could be modified for specific applications depending on the intended use. For example, the shaft length can be varied to achieve a targeted insertion depth. Additionally, greater changes to the process flow are possible to achieve different MN types, as shown in Figure 1.2.

The fabrication of solid silicon microneedles is completed using the combination of the bevel and shaft processes, and the result can be seen in Figure 5.19. The production of solid MN opens avenues to different methods of delivery, most simply the ‘poke and patch’ method described in Chapter 1 Section 1.2.2. To produce coated MN, the solid microneedles could be covered with an active formulation, suitable for vaccine applications such as Influenza where large quantities of fluid are not required [54, 56]. Combined with porous silicon manufacturing techniques, the solid MN could be used to produce a porous MN array where the solution is captured by the cavities on the surface of the microneedle allowing passive diffusion [68-70].

If it’s possible to process the bore etch on the frontside rather than the wafer backside i.e. starting on the bevelled surface, it would be possible to create a microneedle similar in

function to the coated variant, illustrated in Figure 6.5. By only processing to a set depth rather than through the wafer, the large cavity could be filled with the active solution before insertion, allowing controlled diffusion of the formulation without the negative effect on penetration suffered by coated MN from the blunting of the tip and widening of the MN [63]. The processing of a frontside bore process would require a dedicated development.

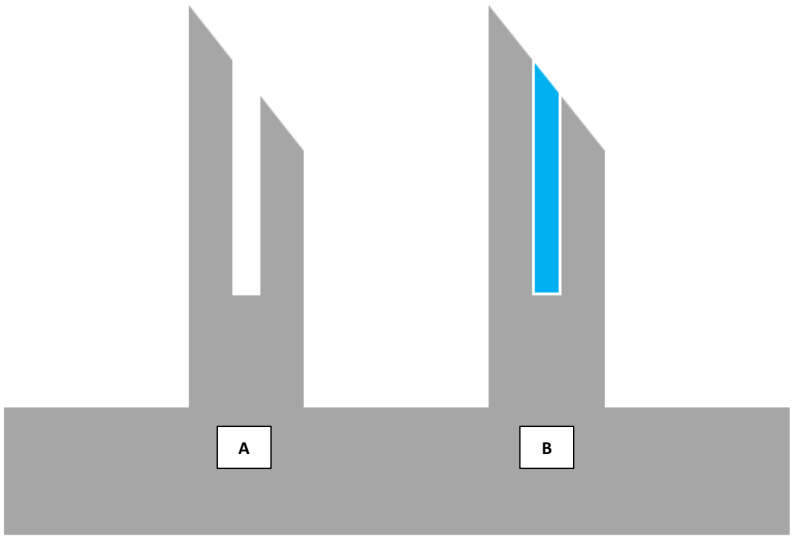

Figure 6.5. *(A) Illustration of a partial depth bore etch completed from the frontside, bevelled surface of the MN. (B) The bore is filled with the active solution (blue) permitting passive diffusion.*

6.3.2 Comparison to Existing MN

With the final device completed, comparisons to MN available on the commercial market can be drawn. Examples of existing hollow silicon microneedles are described in Chapter 1 Section 1.3.3.

Nanopass produce the MicronJet [113], a hollow silicon microneedle consisting only of a wet-etched bevel and bore [110] as shown in Figure 1.6a. Due to the wedge shape of the MicronJet, the instructions for use are more complex than the perpendicular insertion required with the MN produced in this project. Though still easier and safer to use than a

hypodermic needle, the MicronJet must be inserted at 45° to the skin with the correct side of the array facing down [186]. A line is present on the device applicator to aid with the correct orientation of the MN when injecting, however there is still the possibility of confusion if the user is not familiar with the device.

The DebioJect microneedle produced by DebioTech [114] and Bella-mu device from U-needle [117] can be seen in Figure 1.6b and Figure 1.6c respectively, and are more similar to the MN developed here due to the presence of the shaft. The DebioJect device uses a spring-loaded applicator to aid insertion [115] which adds complication to the device and an additional point-of-failure. The Bella-mu needle is produced in-plane before the needle is removed from the wafer and mounted in an applicator [12]. The Bella-mu MN are produced with excessive length and mounted sunken into the applicator to protrude to the correct height for use – this results in a lot of unused length, reducing the number of devices that are produced from one wafer.

The common benefit of the microneedles produced in this development over the existing variants of hollow silicon microneedles is the avoidance of hazardous wet chemicals in the manufacturing process [6]. The novel plasma production flow [149, 150] presented facilitates the manufacture of the hollow bevelled MN developed in this project without the use of KOH or HF, while maintaining the benefits presented by the combination of the bevel, bore, and shaft for painless transdermal injection.

6.3.3 Academic and Commercial Interest

The hollow silicon microneedles fabricated in this project have received attention from individuals and groups in both the commercial and research sectors. Several research groups have expressed interest in acquiring devices for their own testing, either of the device itself or a therapy being developed by the enquiring party. Jereon Wissink, Founder and CEO of U-needle BV, requested a meeting to discuss the device and specifically noted that he wasn't

aware that etching as deep as the bore was possible using a plasma etch process. Martin Peacock is the Director of Zimmer & Peacock AS, a company focussed on collaboration with academia and industry to bring new devices to market; his interest in the project is to accelerate the timeline of the microneedle devices to serve a commercial audience, with parties already enquiring about the purchase of these arrays for their own testing.

6.4 Further Work

6.4.1 Silicon Plasma Dicing

To create discrete devices from a whole processed wafer, the individual microneedle arrays must be separated. This is known as singulation or dicing, and the current method to achieve this and produce usable MN die for testing is saw dicing [187, 188]. As the name suggests, saw dicing uses a mechanical Diamond- or Silicon Carbide-tipped saw to remove material from between the die, separating the devices ready for use along dicing lanes or 'streets' [187, 188]. This is an established process but has some disadvantages. Firstly, the motion of the saw has an impact on the mechanical stability of die that are produced from the wafer, as the diamond saw can produce chips in the side of the silicon which may induce damage in the devices [187, 188]. Secondly, and specifically relating to the microneedles developed here, saw dicing leaves a wall around the device as the sawing must be completed through a thick part of the wafer, causing walls around the MN device. This can impact the ability of specific die to penetrate the skin as the height of the wall limits the penetration depth. An example of the wall can be seen behind the array in Figure 6.6. Mechanically sawing through a thick part of the wafer is necessary to avoid damaging the silicon baseplate on which the MN array sits.

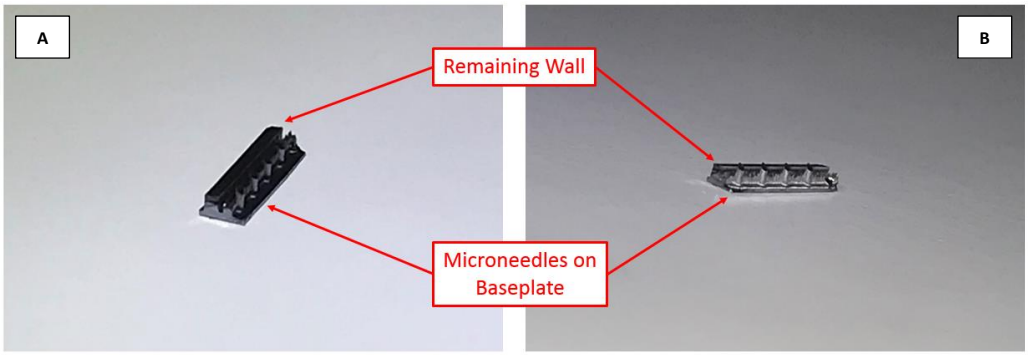

Figure 6.6. *Optical images of a microneedle array with one remaining wall behind the MN. (A) shows the wall along the back of the microneedles, with (B) showing the height of the wall in relation to the MN.*

An alternative to saw dicing is plasma dicing. The objective is the same, to separate the devices by removing the silicon between them, but with plasma dicing this is achieved using plasma etch processes similar to the DRIE processes used in the bore and shaft etches described in earlier chapters [189]. During the plasma dicing process, no additional mechanical stress is placed on the wafer [187, 188] so the dicing could be performed in regions where the silicon is thinner, both removing the issue of structural instability and the wall surrounding the MN. Integration of plasma dicing into the process flow would benefit the consistency of the final device by eliminating the presence of the wall at all positions on the device wafer, improving the insertion capabilities for all die.

As with the plasma etch processes shown in previous chapters, development and optimisation would be required to integrate this as a step in the process flow. However, the features for dicing are significantly simpler (typically >15µm CD trenches) than the developments already undertaken in this project, and plasma dicing is an established technology with examples of existing processes [189-192].

6.4.2 Increased Wafer Sizes

As described in previous chapters, the microneedles fabricated in this project were completed on 100mm diameter wafers. This is a standardised wafer size, but on the smaller end of the common diameters in use for silicon. The frequently used sizes for larger wafers are 150mm, 200mm, and 300mm, and scaling the MN production up to increased diameters has both benefits and drawbacks.

The microneedles need to be manufactured from thick (>1400µm) wafers to allow the creation of the shaft with a depth of up to 1mm. From the perspective of wafer procurement this raises an issue with moving to larger wafer sizes. A search of a wafer supplier [193] for silicon wafers of appropriate thickness gives no results for wafers of 200mm or larger, effectively limiting current options to 100mm or 150mm diameter wafers. For certain applications, including cosmetic microneedle treatments where shorter MN lengths are usable, more standard thickness wafers could be used.

The key benefit of increasing the wafer size is the number of die that can be produced on a single wafer. As an example, the current mask layout of the microneedle pattern on 100mm wafer size yields a maximum 365 die, but a concept layout for 150mm wafers would give a maximum 1004 die. This increase in die per wafer allows more devices to be produced in the same amount of time, desirable in production environments as it increases device throughput for the same operating costs, meaning a lower price per device.

There is also a cost benefit to developing this process flow on 150mm. In the current configuration, 100mm device wafers are placed on 150mm carrier wafers, so a 150mm device wafer would raise the prospect of a carrier-less process flow. This would save on expenditure, simply by reducing the number of wafers to be used coupled with the three-fold increase in the number of die. There would be significant development required for a carrier-less flow though, as the state of device wafers would severely impact the ability of

wafers to clamp. During the bore etch, the pointed bevel side must be placed face down on the platen, which could lead to complications with both cooling (due to the large cavities) and clamping (as the edge of the wafer would have to give a good seal against the platen). Additionally, the holes present in the wafer after the bore etch would need to be reliably covered for the same reasons. Despite these issues there are possible solutions, some of which can be achieved by modifying the mask design.

6.4.3 Other Materials

Plasma etch technology would be compatible with other materials for the creation of MN, given the right process flow. Although significantly more expensive, Silicon Carbide (SiC) [194, 195] is one such material of interest due to its compatibility with dry etch processing [196-198] and the mechanical advantages it holds over silicon [195].

Historically SiC has been used due to its advantageous electrical properties, where a wide bandgap has significant benefits over Si for power device performance [199, 200]. Although this is currently the main area of SiC usage, its mechanical properties have been used to create MEMs devices [201, 202] usually with harsh environments in mind such as high pressure or temperature [195, 203]. SiC is also biocompatible and maintains structural stability due to its relatively high inertness [194]. In the context of MN, this biocompatibility and resilience could be the basis for a personal multi-use MN array for repeated injections.

The use of SiC for microneedles would require a new design and process flow, due to the differences between etching Si and SiC. The history of etching SiC is also less explored than Si, and although plasma-based SiC etches have been developed for specific applications [198, 204] significant process work would be required to produce MN devices in SiC.

6.4.4 Theranostic Microneedles

Theranostic devices are named due to their ability to perform both diagnostic and therapeutic actions, with these devices combining the advantages of regular microneedles with sensing capabilities for *in-situ* sensing of biological metrics [78, 205-207].

Insulin injection for diabetes is one example of an application that benefits from automatic delivery [106, 205, 207]. The on-board sensor would be able to determine the patient's blood sugar level, and if necessary, administer insulin without the intervention or explicit knowledge of the patient. The ability to effectively administer drugs when needed automatically provides a significant benefit to people living with these types of conditions. Modern medicine can further benefit from theranostic technology through optimised therapies based on measured metrics from specific patients, such as protein and biomarker characterisation allowing tailoring of medical treatments to individuals [206].

The creation of microneedles from silicon gives a convenient platform for the future development of biosensor devices by the integration of additional semiconductor processing steps of dielectric and metal deposition [106]. The development of a new theranostic device from the MN described in the previous chapters would involve a significant amount of process development to design the chip, complete the new production steps, and test the resulting device. The new fabrication process would have to be repeated several times to optimise the device, so the development of a theranostic MN chip based on these microneedles would require a dedicated project to realise its potential.

References

1. *Evaluation of materials using scanning electron microscope - thinkymixer.com*. [cited 2022; Available from: https://www.thinkymixer.com/en-gl/library/report/evaluation-of-materials-using-scanning-electron-microscope-sem/.
2. *Skin Anatomy 101 - The Dermatology Specialists*. [cited 2022; Available from: https://www.thedermspecs.com/blog/skin-anatomy-101/.
3. *Anatomy of Skin - Chegg.com*. [cited 2022; Available from: https://www.chegg.com/learn/biology/anatomy-physiology-in-biology/anatomy-of-skin.
4. Levin, Y., et al., *Intradermal vaccination using the novel microneedle device MicronJet600: Past, present, and future.* Human Vaccines & Immunotherapeutics, 2015. **11**(4): p. 991-997.
5. Zhang, X., et al., *Development of Through Silicon Via (TSV) Interposer Technology for Large Die (21x21mm) Fine-pitch Cu/low-k FCBGA Package*, in *2009 Electronic Components and Technology Conference*. 2009, IEEE. p. 305-312.
6. Bolton, C.J.W., et al., *Hollow silicon microneedle fabrication using advanced plasma etch technologies for applications in transdermal drug delivery.* Lab on a Chip, 2020. **20**(15): p. 2788-2795.
7. SANDBY-MØLLER, J., T. POULSEN, and H.C. WULF, *Epidermal Thickness at Different Body Sites: Relationship to Age, Gender, Pigmentation, Blood Content, Skin Type and Smoking Habits.* Acta Dermato-venereologica, 2003. **83**(6): p. 410-413.
8. Sim, K.H., et al., *The Appropriateness of the Length of Insulin Needles Based on Determination of Skin and Subcutaneous Fat Thickness in the Abdomen and Upper Arm in Patients with Type 2 Diabetes.* Diabetes & Metabolism Journal, 2014. **38**(2): p. 120-133.
9. Rouhi, N., et al., *Fabrication of 3-D Silicon Microneedles Using a Single-Step DRIE Process.* Journal of Microelectromechanical Systems, 2015. **24**(5): p. 1409-1414.
10. Vescovo, P., et al., *Safety, tolerability and efficacy of intradermal rabies immunization with DebioJect.* Vaccine, 2017. **35**: p. 1782-1788.
11. Hamzah, A.A., et al., *Optimization of HNA etching parameters to produce high aspect ratio solid silicon microneedles.* Journal of Micromechanics and Microengineering, 2012. **22**: p. 10.
12. Abdilla, J., et al., *Assembly of intradermic, silicon microneedle, using state-of-the-art die bonding equipment*, in *IMAPS DPC 2020*. 2020. p. 10.
13. Liu, Y., et al., *Advanced deep reactive-ion etching technology for hollow microneedles for transdermal blood sampling and drug delivery.* IET Nanobiotechnology, 2013. **7**(2): p. 59-62.
14. Kim, H., L.S. Theogarajan, and S. Pennathur, *A repeatable and scalable fabrication method for sharp, hollow silicon microneedles.* Journal of Micromechanics and Microengineering, 2018. **28**.
15. Wu, B., A. Kumar, and S. Pamarthy, *High aspect ratio silicon etch: A review.* Journal of Applied Physics, 2010. **108**.
16. Jansen, H., et al., *A survey on the reactive ion etching of silicon in microtechnology.* Journal of Micromechanics and Microengineering, 1996. **6**: p. 14-28.
17. Donnelly, V.M. and A. Kornblit, *Plasma etching: Yesterday, today, and tomorrow.* Journal of Vacuum Science & Technology A: Vacuum, Surfaces, and Films, 2013. **31**(5).

18. Laermer, F. and A. Urban, *MEMS at Bosch – Si plasma etch success story, history, applications, and products.* PLASMA PROCESSES AND POLYMERS, 2019. **16**(9).
19. Panduranga, P., et al., *Isotropic silicon etch characteristics in a purely inductively coupled SF6 plasma.* Journal of Vacuum Science and Technology B, 2019. **37**(6).
20. Welch, C.C., et al., *Silicon etch process options for micro- and nanotechnology using inductively coupled plasmas.* Microelectronic Engineering, 2006. **83**: p. 1170-1173.
21. Kim, Y.-S., et al., *Semiconductor Microlenses Fabricated by One-Step Wet Etching.* IEEE Photonics Technology Letters, 2000. **12**(5): p. 507-509.
22. Zubel, I. and M. Kramkowska, *Etch rates and morphology of silicon (hkl) surfaces etched in KOH and KOH saturated with isopropanol solutions.* Sensors and Actuators A: Physical, 2004. **115**(2-3): p. 549-556.
23. Lee, H.Y., et al., *Fabrication of Microholes in Silicon Wafers by Using Wet-Chemical Etching.* New Physics: Sae Mulli, 2018. **68**(8): p. 834-838.
24. Yusof, N., et al., *Optimization of KOH etching process for MEMS square diaphragm using response surface method.* Indonesian Journal of Electrical Engineering and Computer Science, 2019. **15**(1): p. 113-121.
25. Kim, H.J., *Effect of electrode heating on the distribution of the ion production rate in a capacitively coupled plasma deposition reactor in consideration of thermal decomposition.* Vacuum, 2021. **189**: p. 18.
26. Reinhardt, K. and W. Kern, *Handbook of Silicon Wafer Cleaning Technology*. 3 ed. 2018: William Andrew.
27. Reinhardt, K.A. and R.F. Reidy, *Handbook for Cleaning for Semiconductor Manufacturing: Fundamentals and Applications*. 2011: John Wiley & Sons. 590.
28. Song, P., et al., *Surface recombination velocity on wet-cleaned silicon wafers using heterodyne lock-in ca rrierography imaging: measurement uniqueness investigation.* Semiconductor Science and Technology, 2020. **35**: p. 5.
29. Zhang, Y., et al., *High efficient polishing of sliced 4H-SiC (0001) by molten KOH etching.* Applied Surface Science, 2020. **525**: p. 9.
30. Mumford, R., *METHOD OF SMOOTHING A SURFACE*. 2018, SPTS Technologies Ltd: United States.
31. Kim, Y.-C., J.-H. Park, and M.R. Prausnitz, *Microneedles for drug and vaccine delivery.* Advanced Drug Delivery Reviews, 2012. **64**: p. 1547-1568.
32. Guillot, A.J., et al., *Microneedle-Based Delivery: An Overview of Current Applications and Trends.* Pharmaceutics, 2020. **12**: p. 27.
33. Rosso, J.Q.D. and J. Levin, *The Clinical Relevance of Maintaining the Functional Integrity of the Stratum Corneum in both Healthy and Disease-affected Skin.* Journal of Clinical and Aesthetic Dermatology, 2011. **4**(9): p. 22-42.
34. Gerstel, M.S. and V.A. Place, *Drug Delivery Device*. 1976, Alza Corporation: United States.
35. HENRY, S., et al., *Microfabricated Microneedles: A Novel Approach to Transdermal Drug Delivery.* Journal of Pharmaceutical Sciences, 1998. **87**(8): p. 922-925.
36. Yeo, D.C., et al., *Microneedle physical contact as a therapeutic for abnormal scars.* European Journal of Medical Research, 2017. **22**(28): p. 9.
37. CHO, S.I., et al., *Evaluation of the Clinical Efficacy of Fractional Radiofrequency Microneedle Treatment in Acne Scars and Large Facial Pores.* Dermatologic Surgery, 2012. **38**(7pt1): p. 1017-1024.
38. Gualeni, B., et al., *Minimally invasive and targeted therapeutic cell delivery to the skin using microneedle devices.* British Journal of Dermatology, 2018. **178**: p. 731-739.
39. Deng, Y., et al., *Transdermal Delivery of siRNA through Microneedle Array.* Scientific Reports, 2016. **6**: p. 8.

40. Han, S.-K., S.-J. Lee, and H.-Y. Ha, *Skin Moisturizing Effects of a Microneedle Patch Containing Hyaluronic Acid and Lonicerae flos.* Processes, 2021. **9**(2): p. 8.
41. Lee, H.J., et al., *Efficacy of Microneedling Plus Human Stem Cell Conditioned Medium for Skin Rejuvenation: A Randomized, Controlled, Blinded Split-Face Study.* Annals of Dermatology, 2014. **26**(5): p. 584-591.
42. Gorzelanny, C., et al., *Skin Barriers in Dermal Drug Delivery: Which Barriers Have to Be Overcome and How Can We Measure Them?* Pharmaceutics, 2020. **12**(7): p. 684-715.
43. Badran, M.M., J. Kuntsche, and A. Fahr, *Skin penetration enhancement by a microneedle device (Dermaroller®) in vitro: Dependency on needle size and applied formulation.* European Journal of Pharmaceutical Sciences, 2009. **36**: p. 511-523.
44. McCrudden, M.T.C., et al., *Microneedle Applications in Improving Skin Appearance.* Experimental Dermatology, 2015. **24**: p. 561-566.
45. He, X., et al., *Microneedle System for Transdermal Drug and Vaccine Delivery: Devices, Safety, and Prospects.* Dose-Response, 2019: p. 18.
46. Vinayakumar, K.B., et al., *A hollow stainless steel microneedle array to deliver insulin to a diabetic rat.* Journal of Micromechanics and Microengineering, 2016. **26**: p. 9.
47. Lee, I.-C., et al., *Formulation of two-layer dissolving polymeric microneedle patches for insulin transdermal delivery in diabetic mice.* JOURNAL OF BIOMEDICAL MATERIALS RESEARCH A, 2017. **105**(1): p. 84-93.
48. Ma, Y., et al., *An Insulin Microneedle Pen (IMP) for Self-Subcutaneous Insulin Injection.* Advanced Materials Technologies, 2018. **3**(12): p. 8.
49. Pere, C.P.P., et al., *3D printed microneedles for insulin skin delivery.* International Journal of Pharmaceutics, 2018. **544**: p. 425-432.
50. Davis, S.P., et al., *Hollow Metal Microneedles for Insulin Delivery to Diabetic Rats.* IEEE Transactions on Biomedical Engineering, 2005. **52**(5): p. 909-915.
51. Ito, Y., et al., *Dissolving Microneedles as Skin Allergy Test Device.* Biological and Pharmaceutical Bulletin, 2017. **40**(4): p. 531-534.
52. Caudill, C.L., et al., *Spatially controlled coating of continuous liquid interface production microneedles for transdermal protein delivery.* Journal of Controlled Release, 2018. **284**: p. 122-132.
53. Hochberg, L.R., et al., *Neuronal ensemble control of prosthetic devices by a human with tetraplegia.* Nature, 2006. **422**(13): p. 164-171.
54. Koutsonanos, D.G., et al., *Transdermal Influenza Immunization with VaccineCoated Microneedle Arrays.* PLoS ONE, 2009. **4**(3): p. 10.
55. Xie, Y., B. Xu, and Y. Gao, *Controlled transdermal delivery of model drug compounds by MEMS microneedle array.* Nanomedicine: Nanotechnology, Biology, and Medicine, 2005. **1**(2): p. 184-190.
56. Kim, Y.-C., et al., *Formulation and coating of microneedles with inactivated influenza virus to improve vaccine stability and immunogenicity.* Journal of Controlled Release, 2010. **142**: p. 187-195.
57. Mikszta, J.A., et al., *Microneedle-Based Intradermal Delivery of the Anthrax Recombinant Protective Antigen Vaccine.* Infection and Immunity, 2020. **74**(12): p. 6806-6810.
58. Kim, E., et al., *Microneedle array delivered recombinant coronavirus vaccines: Immunogenicity and rapid translational development.* EBioMedicine, 2020. **55**: p. 12.
59. Nguyen, T.T., et al., *Skin immunization with third-generation hepatitis B surface antigen using microneedles.* Vaccine, 2019. **37**: p. 5954-5961.
60. McConville, A., C. Hegarty, and J. Davis, *Mini-Review: Assessing the Potential Impact of Microneedle Technologies on Home Healthcare Applications.* Medicines, 2018. **5**(50): p. 15.

61. Duan, D., et al., *Enhanced Delivery of Topically-Applied Formulations Following Skin Pre-Treatment with a Hand-Applied, Plastic Microneedle Array.* Current Drug Delivery, 2011. **8**: p. 557-565.
62. Bariya, S.H., et al., *Microneedles: an emerging transdermal drug delivery system.* Journal of Pharmacy and Pharmacology, 2012. **64**: p. 11-29.
63. Alkilani, A.Z., M.T.C. McCrudden, and R.F. Donnelly, *Transdermal Drug Delivery: Innovative Pharmaceutical Developments Based on Disruption of the Barrier Properties of the stratum corneum.* Pharmaceutics, 2015. **7**: p. 438-470.
64. Haj-Ahmad, R., et al., *Microneedle Coating Techniques for Transdermal Drug Delivery.* Pharmaceutics, 2015. **7**: p. 486-502.
65. Park, J.-H., M.G. Allen, and M.R. Prausnitz, *Polymer Microneedles for Controlled-Release Drug Delivery.* Pharmaceutical Research, 2006. **23**(5): p. 1008-1019.
66. Sullivan, S.P., N. Murthy, and M.R. Prausnitz, *Minimally invasive protein delivery with rapidly dissolving polymer microneedles.* Advanced Materials, 2008. **20**(5): p. 933-938.
67. Lee, J.W., J.-H. Park, and M.R. Prausnitz, *Dissolving microneedles for transdermal drug delivery.* Biomaterials, 2008. **29**: p. 2113-2124.
68. Anglin, E.J., et al., *Porous silicon in drug delivery devices and materials.* Advanced Drug Delivery Reviews, 2008. **60**: p. 1266-1277.
69. Haidary, S.M., E.P. Córcoles, and N.K. Ali, *Nanoporous Silicon as Drug Delivery Systems for Cancer Therapies.* Journal of Nanomaterials, 2012. **2012**: p. 15.
70. Boks, M.A., et al., *Controlled release of a model vaccine by nanoporous ceramic microneedle arrays.* International Journal of Pharmaceutics, 2015. **491**: p. 375-383.
71. Donnelly, R. and D. Douroumis, *Microneedles for drug and vaccine delivery and patient monitoring.* Drug Delivery and Translational Research, 2015. **5**: p. 311-312.
72. Ashraf, M.W., et al., *Fabrication and analysis of hollow microneedles and polymeric piezoelectric valveless micropump for transdermal drug-delivery system.* IET Communications, 2012. **6**(18): p. 3248-3256.
73. Khanna, P., et al., *Sharpening of hollow silicon microneedles to reduce skin penetration force.* Journal of Micromechanics and Microengineering, 2010. **20**.
74. Li, Y., et al., *Fabrication of sharp silicon hollow microneedles by deep-reactive ion etching towards minimally invasive diagnostics.* Microsystems & Nanoengineering, 2019. **5**(41): p. 11.
75. Jurcicek, P., et al., *Design and fabrication of hollow out-of-plane silicon microneedles.* IET Micro & Nano Letters, 2013. **8**(2): p. 78-81.
76. Griss, P. and G. Stemme, *Side-Opened Out-of-Plane Microneedles for Microfluidic Transdermal Liquid Transfer.* JOURNAL OF MICROELECTROMECHANICAL SYSTEMS, 2003. **12**(3): p. 296-301.
77. Lim, S.H., J.Y. Ng, and L. Kang, *Three-dimensional printing of a microneedle array on personalized curved surfaces for dual-pronged treatment of trigger finger.* Biofabrication, 2017. **9**: p. 13.
78. Sharma, S., et al., *Rapid, low cost prototyping of transdermal devices for personal healthcare monitoring.* Sensing and Bio-Sensing Research, 2017. **13**: p. 104-108.
79. Zhibiao, L., et al., *The Study on Fabrication of Solid Metal Microneedles Based on Optimized Process of Electrochemical Etching and Cutting*, in *The International Conference of Intelligent Robotic and Control Engineering 2018*. 2018, IEEE. p. 56-59.
80. Parker, E.R., et al., *Bulk Micromachined Titanium Microneedles.* JOURNAL OF MICROELECTROMECHANICAL SYSTEMS, 2007. **16**(2): p. 289-295.
81. Bystrova, S. and R. Luttge, *Micromolding for ceramic microneedle arrays.* Microelectronic Engineering, 2011. **88**: p. 1681-1684.

82. Lee, H.J., et al., *A new thin silicon microneedle with an embedded microchannel for deep brain drug infusion.* Sensors and Actuators B: Chemical, 2015. **209**: p. 413-422.
83. Chen, B., et al., *Silicon microneedle array with biodegradable tips for transdermal drug delivery.* Microsystem Technologies, 2008. **14**: p. 1015-1019.
84. Chaudhri, B.P., et al., *A high aspect ratio SU-8 fabrication technique for hollow microneedles for transdermal drug delivery and blood extraction.* Journal of Micromechanics and Microengineering, 2010. **20**: p. 6.
85. Wang, J., et al., *Preparation of Microneedle Array Mold Based on MEMS Lithography Technology.* Micromachines, 2021. **12**(23): p. 13.
86. Stavrinidis, G., et al., *SU-8 microneedles based dry electrodes for Electroencephalogram.* Microelectronic Engineering, 2016. **159**: p. 114-120.
87. Rad, Z.F., et al., *High-fidelity replication of thermoplastic microneedles with open microfluidic channels.* Microsystems & Nanoengineering, 2017. **3**: p. 11.
88. Janphuang, P., et al., *Polymer based microneedle patch fabricated using microinjection moulding*, in *ICEAST 2018*. 2018, MATEC Web of Conferences.
89. Lee, K., et al., *Drawing Lithography: Three-Dimensional Fabrication ofan Ultrahigh-Aspect-Ratio Microneedle.* Advanced Materials, 2010. **22**(4): p. 483-486.
90. Han, M., et al., *A novel fabrication process for out-of-plane microneedle sheets of biocompatible polymer.* Journal of Micromechanics and Microengineering, 2007. **17**: p. 1184-1191.
91. Chen, Y., et al., *Fabrication of coated polymer microneedles for transdermal drug delivery.* Journal of Controlled Release, 2017. **265**: p. 14-21.
92. Chu, L.Y., S.-O. Choi, and M.R. Prausnitz, *Fabrication of Dissolving Polymer Microneedles for Controlled Drug Encapsulation and Delivery: Bubble and Pedestal Microneedle Designs.* Journal of Pharmaceutical Sciences, 2010. **99**(10): p. 4228-4238.
93. Tuan-Mahmood, T.-M., et al., *Microneedles for intradermal and transdermal delivery.* European Journal of Pharmaceutical Sciences, 2013. **50**(5): p. 623-627.
94. Mansoor, I., U.O. Hafeli, and B. Stoeber, *Hollow Out-of-Plane Polymer Microneedles Made by Solvent Casting for Transdermal Drug Delivery.* Journal of Microelectromechanical Systems, 2012. **21**(1): p. 44-52.
95. Lhernould, M.S., M. Deleers, and A. Delchambre, *Hollow polymer microneedles array resistance and insertion tests.* International Journal of Pharmaceutics, 2015. **480**: p. 152-157.
96. Wang, P.-C., et al., *Hypodermic-Needle-Like Hollow Polymer Microneedle Array: Fabrication and Characterization.* JOURNAL OF MICROELECTROMECHANICAL SYSTEMS, 2014. **23**(4): p. 991-998.
97. Wang, P.-C., et al., *Hollow Polymer Microneedle Array Fabricated by Photolithography Process Combined with Micromolding Technique*, in *31st Annual International Conference of the IEEE EMBS*. 2009: Minneapolis, Minnesota, USA. p. 7026-7029.
98. Rad, Z.F., P.D. Prewett, and G.J. Davies, *Rapid prototyping and customizable microneedle design: Ultra-sharp microneedle fabrication using two-photon polymerization and low-cost micromolding techniques.* Manufacturing Letters, 2021. **30**: p. 39-43.
99. Sammoura, F., et al., *Polymeric microneedle fabrication using a microinjection molding technique.* Microsystem Technologies, 2007. **13**: p. 517-522.
100. Bao, L., et al., *Recent advances in porous microneedles: materials, fabrication, and transdermal applications.* Drug Delivery and Translational Research, 2022. **12**: p. 395-414.

101. García-López, E., H.R. Siller, and C.A. Rodríguez, *Study of the fabrication of AISI 316L microneedle arrays*, in *46th SME North American Manufacturing Research Conference, NAMRC 46*. 2018, Procedia Manufacturing: Texas, USA. p. 117-124.
102. Aldawood, F.K., A. Andar, and S. Desai, *A Comprehensive Review of Microneedles: Types, Materials, Processes, Characterizations and Applications.* Polymers, 2021. **13**: p. 2815-2849.
103. Fisher, G., M.R. Seacrist, and R.W. Standley, *Silicon Crystal Growth and Wafer Technologies.* Proceedings of the IEEE, 2012. **100**: p. 1454-1474.
104. Liu, L., et al., *A minimally invasive micro sampler for quantitative sampling with an ultrahigh-aspect-ratio microneedle and a PDMS actuator.* Biomedical Microdevices, 2016. **18**: p. 11.
105. Ashraf, M.W., et al., *Design, Fabrication and Analysis of Silicon Hollow Microneedles for Transdermal Drug Delivery System for Treatment of Hemodynamic Dysfunctions.* Cardiovascular Engineering, 2010. **10**: p. 91-108.
106. Donnelly, R.F., T.R.R. Singh, and A.D. Woolfson, *Microneedle-based drug delivery systems: Microfabrication, drug delivery, and safety.* Drug Delivery, 2010. **17**(4): p. 187-207.
107. Liwei, L. and A.P. Pisano, *Silicon-processed microneedles.* Journal of Microelectromechanical Systems, 1999. **8**(1): p. 78-84.
108. Jarvis, K.L., T.J. Barnes, and C.A. Prestidge, *Surface chemistry of porous silicon and implications for drug encapsulation and delivery applications.* Advances in Colloid and Interface Science, 2012. **175**: p. 25-38.
109. Li, X. and P.W. Bohn, *Metal-assisted chemical etching in HF/H2O2 produces porous silicon.* APPLIED PHYSICS LETTERS, 2000. **77**(16): p. 2572-2574.
110. Gardeniers, H.J.G.E., et al., *Silicon Micromachined Hollow Microneedles for Transdermal Liquid Transport.* JOURNAL OF MICROELECTROMECHANICAL SYSTEMS, 2003. **12**(6): p. 855-862.
111. *Hydrofluoric Acid - Safety Data Sheet*. 2020, ThermoFisher Scientific.
112. *Potassium Hydroxide - Safety Data Sheet*. 2021, ThermoFisher Scientific.
113. *Homepage - NanoPass Technologies Ltd*. [cited 2022; Available from: https://www.nanopass.com/.
114. *DebioJect - DebioTech SA*. [cited 2022; Available from: https://www.debiotech.com/debioject/.
115. Lhernould, M.S., et al., *Review of Patents for Microneedle Application Devices Allowing Fluid Injections Through the Skin.* Recent Patents on Drug Delivery & Formulation, 2015. **9**(2): p. 146-157.
116. *Homepage - U-Needle*. [cited 2022; Available from: https://www.uneedle.com/.
117. *Bella-mu - U-Needle*. [cited 2022; Available from: https://www.uneedle.com/needle/bella-mu.
118. McGrath, J.A., R.A.J. Eady, and F.M. Pope, *Rook's Textbook of Dermatology*. Seventh ed. 2004: Blackwell Publishing.
119. Habif, T.P., *Clinical Dermatology: a color guide to diagnosis and therapy*. Sixth ed. 2016: Elsevier.
120. Marks, J.G. and J.J. Miller, *Lookingbill and Marks' Principles of Dermatology*. Sixth ed. 2019: Elsevier.
121. James, W.D., T.G. Berger, and D.M. Elston, *Andrews' Diseases of the skin: clinical dermatology*. Eleventh ed. 2011: Saunders Elsevier.
122. Narayan, R., *Biomedical Materials*. Second ed. 2021: Springer.
123. Prausnitz, M.R., et al., *Skin Barrier and Transdermal Drug Delivery.* Medical Therapy, 2012: p. 2065-2073.

124. Russell, L.M., S. Wiedersberg, and M.B. Delgado-Charro, *The determination of stratum corneum thickness An alternative approach.* European Journal of Pharmaceutics and Biopharmaceutics, 2008. **69**(3): p. 861-870.
125. Jenner, E., *An Inquiry into the Causes and Effects of the Variolæ Vaccinæ*. 1798, London: Sampson Low.
126. Mogey, G.A., *Centenery of Hypodermic Injection.* British Medical Journal, 1953. **2(4847)**: p. 1180-1185.
127. Deacon, B. and J. Abramowitz, *Fear of Needles and Vasovagal Reactions Among Phlebotomy Patients.* Anxiety Disorders, 2006. **20**: p. 946-960.
128. Ball, J. and G. Pike, *Needlestick Injuries in 2008*. 2008, Royal College of Nurses.
129. Saia, M., et al., *Needlestick Injuries: Incidence and Cost in the United States, United Kingdom, Germany, France, Italy, and Spain.* Biomedicine International, 2010. **1**: p. 41-49.
130. Wilburn, S.Q. and G. Eijkemans, *Preventing Needlestick Injuries among Healthcare Workers: A WHO–ICN Collaboration.* International Journal of Occupational and Environmental Health, 2004. **10**: p. 451-456.
131. YANG, Y.-H., et al., *The Effectiveness of a Training Program on Reducing Needlestick Injuries/Sharp Object Injuries among Soon Graduate Vocational Nursing School Students in Southern Taiwan.* Journal of Occupational Health, 2007. **49**: p. 424-429.
132. Blenkharn, J.I., *Sharps management and the disposal of clinical waste.* British Journal of Nursing, 2009. **18**(14): p. 860-864.
133. Olowokure, B., H.V. Duggal, and L.E. Armitage, *The disposal of used sharps by diabetic patients living at home.* International Journal of Environmental Health Research, 2003. **13**: p. 117-123.
134. Govender, D. and A. Ross, *Sharps disposal practices among diabetic patients using insulin.* South African Medical Journal, 2012. **102**(3): p. 163-164.
135. Blenkharn, J.I. and C. Odd, *Sharps Injuries in Healthcare Waste Handlers.* Annals of Occupational Hygiene, 2008. **52**(4): p. 281-286.
136. Moustafa, F., et al., *Needle Manufacturing, Quality Control, and Optimization for Patient Comfort.* Journal of Drugs in Dermatology, 2021. **20**(1): p. 44-48.
137. Elmiyeh, B., et al., *Needle-stick injuries in the National Health Service: a culture of silence.* Journal of the Royal Society of Medicine, 2004. **97**: p. 326-327.
138. Gill, H.S., et al., *Effect of microneedle design on pain in human subjects.* The Clinical Journal of Pain, 2010. **24**(7): p. 585-594.
139. Prausnitz, M.R., et al., *Microneedle-based vaccines.* Current topics in microbiology and immunology, 2009. **333**: p. 369-393.
140. Donnelly, R.F., et al., *Microneedle Arrays Allow Lower Microbial Penetration Than Hypodermic Needles In Vitro.* Pharmaceutical Research, 2009. **26**(11): p. 2513-2522.
141. Vicente-Perez, E.M., et al., *Repeat application of microneedles does not alter skin appearance or barrier function and causes no measurable disturbance of serum biomarkers of infection, inflammation or immunity in mice in vivo.* European Journal of Pharmaceutics and Biopharmaceutics, 2017. **117**: p. 400-407.
142. Wei-Ze, L., et al., *Super-short solid silicon microneedles for transdermal drug delivery applications.* International Journal of Pharmaceutics, 2010. **389**: p. 122-129.
143. Quan, F.-S., et al., *Dose sparing enabled by skin immunization with influenza viruslike particle vaccine using microneedles.* Journal of Controlled Release, 2010. **147**(3): p. 326-332.
144. Damme, P.V., et al., *Safety and efficacy of a novel microneedle device for dose sparingintradermal influenza vaccination in healthy adults.* Vaccine, 2009. **27**(3): p. 454-459.

145. Roxhed, N., et al., *Painless Drug Delivery Through Microneedle-Based Transdermal Patches Featuring Active Infusion.* IEEE Transactions on Biomedical Engineering, 2008. **55**(3): p. 1063-1071.
146. Kaushik, S., et al., *Lack of Pain Associated with Microfabricated Microneedles.* Anesthesia & Analgesia, 2001. **92**(2): p. 502-504.
147. Gupta, J., et al., *Infusion pressure and pain during microneedle injection into skin of human subjects.* Biomaterials, 2011. **32**(11): p. 6823-6831.
148. Chen, X., et al., *Dry-coated microprojection array patches for targeted delivery of immunotherapeutics to the skin.* Journal of Controlled Release, 2009. **139**: p. 212-220.
149. Roberts, K., H. Ashraf, and P.F. Eng, *MICRONEEDLES*. 2020, SPTS Technologies Ltd: Europe.
150. Roberts, K., H. Ashraf, and P.F. Eng, *MICRONEEDLES*. 2021, SPTS Technologies Ltd: United States.
151. Davis, S.P., et al., *Insertion of microneedles into skin: measurement and prediction of insertion force and needle fracture force.* Journal of Biomechanics, 2004. **37**: p. 1155-1163.
152. Pei, Z.J., G.R. Fisher, and J. Liu, *Grinding of silicon wafers: a review from historical perspectives.* International Journal of Machine Tools and Manufacture, 2008. **48**(12-13): p. 1297-1307.
153. SEMI. *Standards*. 2021; Available from: https://www.semi.org/en/products-services/standards.
154. Flamm, D.L., *Mechanisms of silicon etching in fluorine- and chlorine-containing plasmas.* Pure & Applied Chemistry, 1990. **62**(9): p. 1709-1720.
155. Ghoshal, T., et al., *"In situ" hard mask materials: a new methodology for creation of vertical silicon nanopillar and nanowire arrays.* Nanoscale, 2012. **4**(24): p. 7743-7750.
156. Fridman, A., *Plasma Chemistry*. 2008: Cambridge University Press.
157. Chu, P.K. and X. Lu, *Low Temperature Plasma Technology: Methods and Applications*. 2013: CRC Press.
158. Tachi, S., K. Tsujimoto, and S. Okudaira, *Low-temperature reactive ion etching and microwave plasma etching of silicon.* Applied Physics Letters, 1988. **52**(8): p. 616-618.
159. KOVACS, G.T.A., N.I. MALUF, and K.E. PETERSEN, *Bulk Micromachining of Silicon.* Proceedings of the IEEE, 1998. **86**(8): p. 1536-1551.
160. Hopwood, J., *Review of inductively coupled plasmas for plasma processing.* Plasma Sources Science and Technology, 1992. **1**: p. 109-116.
161. DeSalvo, G.C., et al., *Wet Chemical Digital Etching of GaAs at Room Temperature.* Journal of The Electrochemical Society, 1996. **143**(11): p. 3652-3656.
162. *Sigma SEM - Carl Zeiss Ltd*. [cited 2021; Available from: https://www.zeiss.com/microscopy/int/products/scanning-electron-microscopes/sigma.html.
163. *Omega DRIE Products - SPTS Technologies Ltd*. [cited 2021; Available from: https://www.spts.com/product/si-drie.
164. Thomas, D., et al., *Deep Silicon Etching - Increasingly Relevant >20 Years On!* ECS Transactions, 2016. **72**(19): p. 9-22.
165. Resnik, M., et al., *Comparison of SF6 and CF4 Plasma Treatment for Surface Hydrophobization of PET Polymer.* Materials, 2018. **11**: p. 10.
166. Takahashi, K. and K. Tachibana, *Solid particle production in fluorocarbon plasmas. I. Correlation with polymer film deposition.* Journal of Vacuum Science & Technology, 2001. **19**(5): p. 2055-2060.

167. Laermer, F. and A. Schilp, *METHOD OF ANISOTROPICALLY ETCHING SILICON*. 1994, Robert Bosch GmbH.
168. *DM120000 Optical Microscope - Leica Microsystems*. [cited 2021; Available from: https://www.leica-microsystems.com/products/light-microscopes/p/leica-dm12000-m/.
169. *MX50 Optical Microscope - Olympus*. [cited 2021; Available from: https://www.olympus-global.com/en/news/1998b/nr981125mx50le.html.
170. Antony, J., *Design of Experiments for Engineers and Scientists*. 2003: Elsevier Ltd.
171. Karttunen, J., J. Kiihamäki, and S. Franssila, *Loading effects in deep silicon etching.* Proceedings of SPIE, 2000. **4174**: p. 90-97.
172. Jensen, S. and O. Hansen, *Characterization of the Microloading Effect in Deep Reactive Ion Etching of Silicon.* Proceedings of SPIE, 2003. **5342**.
173. Oh, J.-H., et al., *Influence of the delivery systems using a microneedle array on the permeation of a hydrophilic molecule, calcein.* European Journal of Pharmaceutics and Biopharmaceutics, 2008. **69**: p. 1040-1045.
174. *Medtronic Minimed 780g System - Insulin Pump Therapy*. 2022; Available from: https://www.medtronic-diabetes.co.uk/insulin-pump-therapy/minimed-780g-system.
175. Motoyoshi, M., *Through-Silicon Via (TSV).* Proceedings of the IEEE, 2009. **97**(1): p. 43-48.
176. Tang, Y., A. Sandoughsaz, and K. Najafi, *Ultra High Aspect-Ratio And Thick Deep Silicon Etching (UDRIE)*, in *2017 IEEE 30th International Conference on Micro Electro Mechanical Systems (MEMS)*. 2017: Las Vegas, NV. p. 700-703.
177. Tang, Y., et al., *Ultra Deep Reactive Ion Etching of High Aspect-Ratio and Thick Silicon Using a Ramped-Parameter Process.* Journal of Microelectromechanical Systems, 2018. **27**(4): p. 686-697.
178. *MORFLEX - Flexible Process Control for MEMS & TSV - SPTS Technologies Ltd*. [cited 2021; Available from: https://www.spts.com/resources/tech-insights/morflex-flexible-process-control-for-mems-tsv.
179. Hopkins, J., et al., *The Benefits of Process Parameter Ramping During The Plasma Etching of High Aspect Ratio Silicon Structures.* MRS Online Proceedings Library, 1998. **546**: p. 63-68.
180. Lai, S., et al. *Notch Reduction in Silicon on Insulator (SOI) Structures Using a Time Division Multiplex Etch Processes*. in *MOEMS-MEMS Micro and Nanofabrication*. 2005. San Jose, California, United States: SPIE.
181. Kim, K.H., et al., *DRIE fabrication of notch-free silicon structures using a novel silicon-on-patterned metal and glass wafer.* Journal of Micromechanics and Microengineering, 2011. **21**(045018): p. 7.
182. Jeong, J.-W., *High Aspect Ratio Si Etching in STS2*. 2010, Stanford University. p. 1-4.
183. Hopkins, J., et al., *METHOD AND APPARATUS FOR ETCHING A SUBSTRATE*. 2001, Surface Technology Systems Limited.
184. Iliescu, C., et al., *Transdermal drug delivery: microfabrication insights*, in *International Semiconductor Conference* 2009, IEEE. p. 203-209.
185. Krishnan, M., J.W. Nalaskowski, and L.M. Cook, *Chemical Mechanical Planarization: Slurry Chemistry, Materials, and Mechanisms.* Chemical Reviews, 2010. **110**: p. 178-204.
186. *Instructions for Use - NanoPass Technologies Ltd*. [cited 2022; Available from: https://www.nanopass.com/micronjet-microneedle-device/instructions-for-use/.
187. Hooper, A., et al. *Review of wafer dicing techniques for via-middle process 3DI/TSV ultrathin silicon device wafers*. in *Electronic Components and Technology Conference*. 2015.

188. Lei, W.-S., A. Kumar, and R. Yalamanchili, *Die singulation technologies for advanced packaging: A critical review.* Journal of Vacuum Science & Technology B, 2012. **30**(4): p. 27.
189. Suhard, S., et al., *Demonstration of a collective hybrid die-to-wafer integration using glass carrier*, in *IEEE 71st Electronic Components and Technology Conference (ECTC)*. 2021. p. 2064-2070.
190. Barnett, R., O. Ansell, and D. Thomas, *Considerations and Benefits of Plasma Etch Based Wafer Dicing*, in *2013 IEEE 15th Electronics Packaging Technology Conference (EPTC 2013)*. 2013, IEEE: Singapore. p. 569-574.
191. Barnett, R., et al. *IMPROVED SEMICONDUCTOR DEVICE RELIABILITY FROM PLASMA DICING*. in *International Wafer-Level Packaging Conference*. 2019. San Jose, USA.
192. Barnett, R., D. Thomas, and O. Ansell. *SINGULATION BY PLASMA ETCHING. INTEGRATION TECHNIQUES TO ENABLE LOW DAMAGE, HIGH PRODUCTIVITY DICING.* in *ASME 2015 International Technical Conference and Exhibition on Packaging and Integration of Electronic and Photonic Microsystems*. 2015. San Francisco, USA.
193. *Silicon Wafer Search - Inseto*. [cited 2022; Available from: https://www.inseto.co.uk/product-category/semiconductor-wafers/si_wafer/.
194. Bonaventura, G., et al., *Biocompatibility between Silicon or Silicon Carbide surface and Neural Stem Cells.* Scientific Reports, 2019. **9**.
195. Marsi, N., et al., *A Review: Properties of Silicon Carbide Materials in MEMS Application.* International Journal of Nanoelectronics and Materials, 2020. **13**: p. 113-128.
196. Osipov, A.A., et al., *Dry etching of silicon carbide in ICP with high anisotropy and etching rate.* IOP Conference Series: Materials Science and Engineering, 2020. **862**.
197. Osipov, A.A., et al., *Etching of SiC in Low Power Inductively-Coupled Plasma.* Russian Microelectronics, 2018. **47**(6): p. 427-433.
198. Pirnaci, M.D., et al., *Systematic Characterization of Plasma-Etched Trenches on 4H-SiC Wafers.* ACS Omega, 2021. **6**: p. 20667−20675.
199. She, X., et al., *Review of Silicon Carbide Power Devices and Their Applications.* IEEE TRANSACTIONS ON INDUSTRIAL ELECTRONICS, 2017. **64**(10): p. 8193-8205.
200. Yaakub, M.F., et al., *Silicon carbide power device characteristics, applications and challenges: an overview.* International Journal of Power Electronics and Drive System (IJPEDS), 2020. **11**(4): p. 2194-2202.
201. Wood, G.S., et al., *3C-Silicon Carbide Microresonators for Timing and Frequency Reference.* Micromachines, 2016. **7**(11): p. 23.
202. Mackowiak, P., et al., *Piezoresistive 4H-Silicon Carbide (SiC) pressure sensor*, in *IEEE Sensors*. 2021, IEEE: Sydney, Australia.
203. Guo, X., et al., *Silicon Carbide Converters and MEMS Devices for High-temperature Power Electronics: A Critical Review.* Micromachines, 2019. **10**(6): p. 26.
204. Ozgur, M., M. Pedersen, and M. Huff, *Comparison of the Etch Mask Selectivity of Nickel and Copper for a Deep, Anisotropic Plasma Etching Process of Silicon Carbide (SiC).* ECS Journal ofSolid State Science and Technology, 2018. **8**(2): p. 55-59.
205. Rad, Z.F., P.D. Prewett, and G.J. Davies, *An overview of microneedle applications, materials, and fabrication methods.* Beilstein Journal of Nanotechnology, 2021. **12**: p. 1034-1046.
206. Jeelani, S., et al., *Theranostics: A treasured tailor for tomorrow.* Journal of Pharmacy And Bioallied Science, 2014. **6**(5): p. 6-8.
207. Yang, J., et al., *Recent Progress in Microneedles-Mediated Diagnosis,Therapy, and Theranostic Systems.* Advanced Healthcare Materials, 2022: p. 29.

Appendix

Supplementary documents.

Contents

Lab on a Chip, Volume 20 Issue 15, p.2788-2795, 2020

C. J. W. Bolton, O. Howells, G. J. Blayney, P. F. Eng, J. C. Birchall, B. Gualeni, K. Roberts, H. Ashraf, O. J. Guy

"Hollow silicon microneedle fabrication using advanced plasma etch technologies for applications in transdermal drug delivery"

DOI: 10.1039/d01c00567c

Lab on a Chip

PAPER

Cite this: *Lab Chip*, 2020, **20**, 2788

Hollow silicon microneedle fabrication using advanced plasma etch technologies for applications in transdermal drug delivery

Chris J. W. Bolton, *[ab] Olivia Howells,[b] Gareth J. Blayney,[b] Pey F. Eng,[c] James C. Birchall,[d] Benedetta Gualeni,[d] Kerry Roberts,[a] Huma Ashraf[a] and Owen J. Guy[b]

Received 1st June 2020,
Accepted 20th June 2020

DOI: 10.1039/d0lc00567c

rsc.li/loc

A novel production process flow is presented here for the manufacture of hollow silicon microneedles using deep reactive-ion etching (DRIE) technology. The patent-pending three-step process flow has been developed to produce multiple arrays of sharp-tipped, hollow microneedles, which facilitate easy insertion and controlled fluid injection into excised skin samples. A bevelled tip and vertical sidewalls for the microneedle have been achieved with good uniformity, despite >45% open etch area. Processing steps and etch challenges are discussed, and preliminary skin testing results are presented, showing effective needle insertion and delivery of fluorescent dye into *ex vivo* skin from human breast tissue.

Introduction

Microneedles (MN) are becoming increasingly popular in biomedical applications for several reasons: transdermal insertion is regarded as painless and minimally invasive, compared to traditional hypodermic needles;[2,3] reduced discomfort and fear of injection among patients;[2–4] reduced risk of infection.[5,6] Microneedles do not have the same potential for physical or infectious harm presented by conventional hypodermic needles, and therefore use of hollow microneedles in place of hypodermics would significantly decrease the risk of sharps injuries to medical professionals.[4,7–10]

Microneedles are typically constructed from plastic,[11,12] metal[13] or silicon.[14] Examples of hollow plastic needles are available,[11] however the majority of commercially available polymer microneedles remain solid due to the difficulty involved with integrating the bore.[12,15,16] The plastic moulding process also restricts flexibility in the design whereas dry silicon etching allows for tailoring of processes to individual applications, for example needle length to target different skin depths.

Metal MNs are expensive to produce[17] and it has proven difficult to machine hollow metal MNs in a cost effective production process. In terms of width dimensions, the 32G hypodermic needle is similar to the hollow silicon microneedles presented here, but the risk associated with the much increased length of the hypodermic requires continuous training programmes in order to be handled safely,[18,19] and their use results in more pain compared to microneedles.[3]

Hollow bevelled silicon microneedles have been demonstrated,[14] but in general their fabrication either relies heavily on wet chemicals such as KOH or HF for the creation of the bevelled surface,[14,20–22] or plasma etching of the bevel surface results in an unconventional needle shape.[14,23]

Advancements in dry etching technologies have made it possible to develop a manufacture process flow that produces repeatable silicon hollow bevelled microneedles.[24]

The novel process flow here benefits from the avoidance of hazardous wet chemicals while maintaining a recognisable and easily used needle shape. Additionally, the nature of the semiconducting material further permits the future development of an all-in-one diagnostic and therapeutic (theranostic) device.[25] Metal plating and dielectric deposition on silicon means that a sensing microchip device with the additional capability of administering medicines in relation to data input from the MN sensor could be developed.[25]

Hollow microneedles hold a key advantage over the multitude of available 'solid' microneedles; the ability to inject a controlled dose. Solid microneedles do not give the same benefit of pressured sub-dermal injection of fluids, and instead rely on the passive diffusion of fluid through previously created holes.[12] This method is adequate for the cosmetics industry,[26] but does not deliver the precision needed for state of the art medical applications. Additionally, the bevelled tip of the microneedle decreases the insertion

[a] *SPTS Technologies, Ringland Way, Newport, NP18 2TA, UK. E-mail: chris.bolton@spts.com*
[b] *College of Engineering, Swansea University, Swansea, SA2 8PP, UK*
[c] *BioMEMS Technologies, Cardiff, UK*
[d] *School of Pharmacy and Pharmaceutical Sciences, Cardiff University, Cardiff, CF10 3NB, UK*

force required to break through a patient's *stratum corneum*, reducing discomfort and potential issues with *in situ* breakage due to application force.[2,23,27]

The primary focus of this article is to present a novel process flow for the fabrication of hollow silicon microneedles, exclusively using dry plasma processing techniques. In addition to this, the results of a number of proof of concept experiments are presented to show effective insertion and injection of the MNs. However, at this stage these biological tests are not intended to be comprehensive and will be expanded upon in future studies.

Method

Etching and photolithography

Silicon wafers were purchased from Si-mat (Silicon Materials, Germany) while photolithography resists and developer were purchased from Microchemicals GmbH. Etching steps were performed on a SPTS Technologies DSi-v RF plasma processing chamber (Fig. 1).

A Laurell WS-650 spin coater was used to coat the wafers with AZ125 NXT photoresist for the bevel and bore patterning process, while a SUSS MicroTec AS8 spray coater was used to deposit AZnLof2070 photoresist for the microneedle shaft patterning. Photolithography resist patterning was hardened using a SUSS MicroTec MA8 UV mask aligner that allows backside alignment. Once patterned, wafer masking was completed using AZ276 developer.

Characterisation

Proof of concept microneedle penetration characterisation was performed using either full thickness porcine skin (Wetlab Ltd. Warwicks, UK) or post-surgical human breast tissue (under full ethical approval and informed patient consent, local research ethics committee reference 08/WSE03/55). Methylene blue, FITC-insulin and DIL (1,1′-dioctadecyl-3,3,3′,3′-tetramethylindocarbocyanine perchlorate), used for characterisation of skin penetration efficacy, were purchased (Sigma-Aldrich, Dorset, UK). An axial compression analyser (Hounsfield/Tinius Olsen H1-KS, PA, USA) was used for mechanical testing. Imaging was performed using fluorescent microscopy (Zeiss Axio Imager M1, Germany) and ImageJ software (Version 1.51k, National Institutes of Health, MD, USA).

Plasma etch processing

A high density, inductively coupled plasma etch system was used to etch the silicon for microneedle production. Due to the requirements of the etched features the selected module was a DSi-v from SPTS Technologies Ltd (Fig. 1). In this tool, the gas enters the chamber thorough a central gas feed before being excited to form a plasma using an RF coil around the top chamber section. The plasma diffuses into the lower chamber, which has a smaller volume compared to other DRIE (deep reactive ion etching) machines, reducing the plasma residence time. Lower residence time leads to a more effective etch step, keeping larger features clean and free from process-induced defects – which is critical for the production of silicon microneedles. The wafer sits on a ceramic platen in the chamber and is electrostatically clamped, allowing it to be cooled by flowing helium to the backside of the substrate. RF bias is applied to the platen to accelerate ions towards the wafer surface, facilitating the physical element of DRIE.

The MN features were etched on die sizes typically 1.7 mm × 7.5 mm, located on a 100 mm diameter wafer. The 100 mm device wafers were carried on a 150 mm substrate, allowing future development of a scalable process for larger (150 mm diameter) wafers. Etched features were analysed using a scanning electron microscope (SEM), to characterise and quantify critical dimensions, surface roughness, and etch quality.

Fabrication steps

The novel process flow for dry etch silicon microneedle fabrication (Fig. 2) consists of three main parts: the bevel

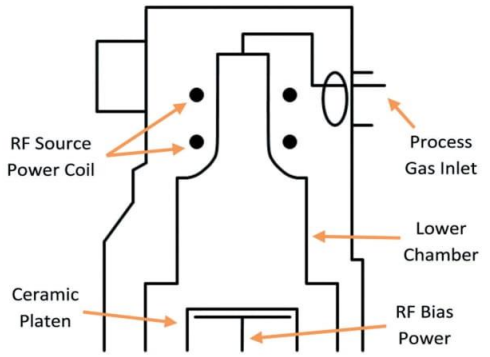

Fig. 1 Cross-section of SPTS Technologies Ltd DSi-v plasma etch chamber. The central gas inlet leads to a low volume chamber for plasma etching of silicon substrates.

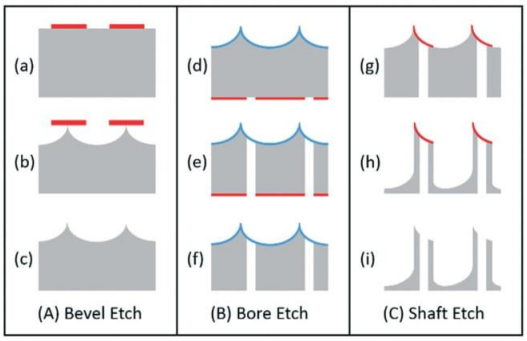

Fig. 2 Process flow for hollow silicon microneedle production, patent pending.[1] Silicon wafers are shown in grey, with photoresist masks and oxide stop layers shown in red and blue respectively.

creation for the angled sharp MN tip [(A) or steps (a) to (c)]; the central bore etch, used for fluid transport within the MN [(B) or steps (d) to (f)]; and the shaft etch, to determine the length and consequently skin penetration depth [(C) or steps (g) to (i)]. Photolithography steps were developed at the Centre for Nanohealth, Swansea University, using AZ125 NXT photoresist resist for steps (a) and (d) and spray coated AZnLof2070 photoresist for step (g). Although this process flow is designed for the manufacture of hollow microneedles, solid microneedles can also be produced by simply removing step (B) from the fabrication sequence.

Dry etch processes

Single step etch

Step (b) in the process flow (Fig. 2) is the creation of the sloped surface required for the bevel of the microneedle. To achieve this, a single step etch was setup whereby vertical and lateral etching takes place in addition to simultaneous passivation. In this case, platen RF bias applied during the process provided ion bombardment to the base surface of the feature.[24] This physical assistance gave the etch some directionality under conditions that would otherwise lead to an isotropic etch form. This partial directionality during the isotropic etch enabled tuning of the bevel angle and resulted in the desired shape for microneedle bevel production.

Switched processing

Traditional switched etching consists of two steps, a polymer deposition (typically consisting of C_4F_8) and an etch step. Anisotropic 2-step DRIE protects the sidewall with the deposition step, and then selectively etches the base of the feature before returning to the deposition step, a sequence known as the Bosch process.[28] More recent switched etching techniques are similar but commonly manifest as a three step process (shown in Fig. 3), consisting of a polymer deposition step (Dep; panel 2), a deposition removal step (etch 1, E1; panel 3), and a silicon etch step (etch 2, E2; panel 4). While the separation of the etch step into E1 and E2 adds to the complexity of the process, it also allows both steps to be more effective. The base deposition is removed more quickly by a physical E1, and the silicon is etched faster in the chemical E2 to increase the overall process etch rate. The separation of steps also has benefits in base roughness, as the base deposition is cleared (with SF_6, O_2 or an SF_6/O_2 combination) before the dedicated etching of Si with SF_6 begins. The cyclical repetition of steps (panels 5–7) produces a directional anisotropic etch with close to vertical sidewalls (panel 8), ideal for steps (e) and (h) of the microneedle process flow (Fig. 2).

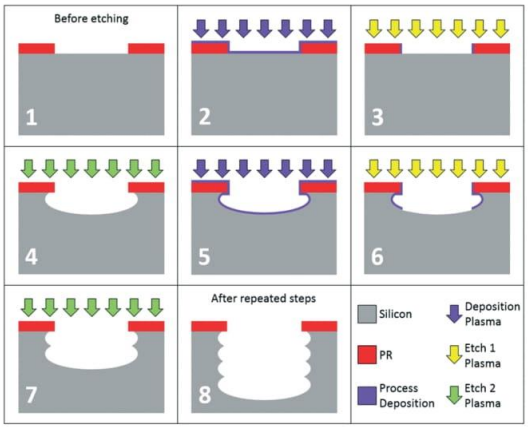

Fig. 3 3-Phase switched etching, illustrated step-by-step.

Process challenges

High open area. The successful etching of high open area wafers (>30%) has long been a challenge for DRIE, as the competition for fluorine radicals increases with the amount of open silicon. This leads to 'loading' effects, where certain parts of a wafer etch more quickly due to relatively lower localised surrounding silicon, which has a detrimental effect on etch depth uniformity. Large differences between these areas (usually centre and edge) is highly undesirable as it can render certain die unusable, reducing total yield.

Bore aspect ratio and depth. The bore etch is similar in application to a traditional through-silicon *via* (TSV),[29] however the etch depth of the microneedle bore is much greater (up to 1.2 mm). A typical TSV etch would be performed with the intention of connecting devices through a thinned wafer, usually 200–500 μm thick with TSV critical dimension (CD) 20–50 μm.[29] In the microneedles case, the TSV (bore) CD needs to be larger to accommodate fluid and particulate flow down the length of the shaft. The TSV depth is also greatly increased as the bore must reach from the top bevelled surface of the wafer to the backside. As microneedle production demands thick wafers to provide sufficient needle insertion depth into skin, this requires dimensions of the bore TSV to be approximately 100 × 1150 μm, more than double the depth of other TSV applications.[29] This significant depth increase exaggerates the risk of process side effects linked to high aspect ratio (AR) etches. Undesirable process effects include wall roughness, grass, striations, and profile changes.[24] Process optimisations focussed on minimising these effects, while maintaining etch quality for the required depth.

Results

Uniformity improvements

For the three etch stages shown in Fig. 2, the etch depth uniformity was a particular challenge for the bevel (b) and shaft (h) steps, as these were performed on patterns with >45% total open area. To control the uniformity of these applications, mask sets were designed whereby excess silicon was available around the edge of the wafer. In the case of the bevel etch (b), this change, in addition to process recipe

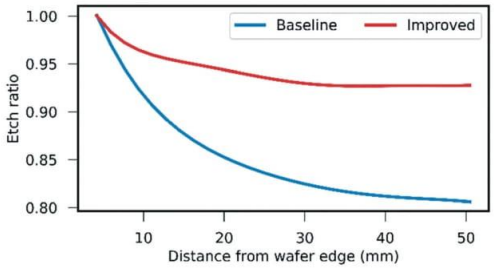

Fig. 4 Graph comparing etch depths from edge to centre of wafer, before and after improvements.

optimisations of 25% RF power increase and 10 mT pressure decrease, resulted in the etch depth uniformity improving from >±11% to <±4% (Fig. 4). This exceeds the uniformity expectation for a wafer with a pattern of this open area and increases the number of usable die per wafer. A similar improvement was also applied to the shaft etch (h), which was optimised for depth uniformity <±3%.

Bevel etch

A peaked profile was achieved by undercutting the PR mask with a single step dry etch process using SF_6, C_4F_8, and O_2 with a flow ratio approximately 6 : 1 : 1 at 70 mTorr chamber pressure. 2500 W RF power was applied with the source coil, and 40 W was used for the RF bias to the platen. Process results are shown in Table 1.

Profile control is essential to produce the angled tip of the needle. Pressure and platen bias were used to control the level of anisotropy for this etch,[24] and a favourable angle of ~20° (Fig. 5) was thus created for the sharp MN tip, which reduces the insertion force required.[27] As well as limiting the mechanical strain on the microneedle upon insertion, the lower force needed to penetrate skin due to the ~20° tip results in less pain for patients.[2,27] In other examples of silicon microneedles, the needle tip is fabricated using a chemical wet etch after the creation of the bore,[14,22] which can compromise bore quality and ultimately limits the final microneedle shapes that can be produced. Processing the needle tip by dry etching allows the bore and shaft to be defined afterwards, thus avoiding wet chemicals and associated process complications.

Table 1 Numerical results for all plasma etch steps in the microneedle production flow

Parameter (units)	Bevel	Bore	Shaft
Depth (μm)	500	1157	790
Etch rate (μm min^{-1})	8.5	8.1	6.2
Profile (°)	~20.0	89.5	89.0
Selectivity (Si : PR)	90	16	74
Uniformity (±%)	4.0	1.1	2.2

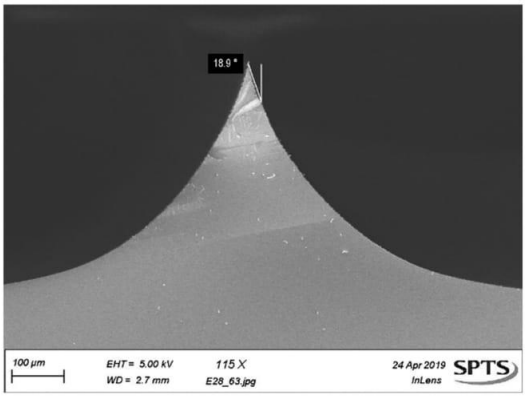

Fig. 5 SEM image showing bevel-etched sharp tip for microneedles.

Bore etch

After being removed from the wafer carriers, bevelled wafers were patterned for the bore step. This included a stop layer on the bevel surface, shown in Fig. 2. Once patterning is completed, wafers are rebonded to the carrier substrate with the backside up to allow for the etching of the bore. While bonded in this configuration, the bevels are protected from damage by protrusions that prevent the sharp tips from bearing weight. Fig. 6 shows a deep TSV etch demonstrated on thick test wafers achieving 1157 μm depth with a *via* CD of 100 μm using the 3-step switched process described above. The Dep, E1, and E2 steps consisted of 450 sccm C_4F_8, 200/100 sccm O_2/SF_6, and 720 sccm SF_6, respectively. Across the total process length, step times, chamber pressure, and platen RF bias values were all varied to maintain a vertical etch profile.

The AR of the bore is in line with current industrial processes at >11 : 1,[24,29] however, the depth presented here

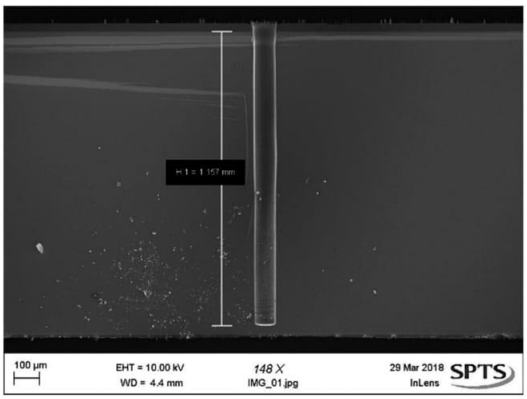

Fig. 6 SEM image showing bore, etched to a depth of 1157 μm on a test wafer for fluid or cell transport.

represents a significant increase on previously demonstrated etches in terms of absolute depth with a circular TSV. 1157 μm is also deeper than 'Ultra Deep Reactive Ion Etch' (UDRIE) processes performed on trenches of a similar CD, despite TSV's having limited species transport to the base of the feature compared to trenches and therefore presenting additional AR,[24] etch rate, and depth challenges.[30]

Previously mentioned AR dependent effects[24] were eliminated by balancing Dep and E2 step times and pressures to minimise damage to the feature, which produced a high quality etch result, exceeding the depth required for MN production. The straight profile does not restrict fluid movement along the bore, while smooth sidewalls aid in limiting turbulent flow and maintained cell viability in cell delivery studies.[31]

Shaft etch

The shaft etch (Fig. 7) resulted in >89° pillar angle to a depth of 790 μm. This was completed with medium source RF powers and low chamber pressure in all three steps. The gas flows were 360 sccm C_4F_8, 320 sccm SF_6, and 315 sccm SF_6 for Dep, E1, and E2 respectively. During the E1 and E2 steps, platen RF bias was applied with 112 W and 36 W respectively; this aids in maintaining a straight sidewall to the microneedle. The achieved profile is key in maintaining mechanical rigidity of the MN; too narrow at the base and the wall thickness between the outside of the microneedle and the central bore becomes a possible fracture point.[27] This shape would also introduce the issue of an 'arrowhead' profile to the microneedle, which is more likely to become lodged in a patient's skin.

Device integration

Fig. 8 shows the combination of the bore etch (Fig. 2e) with the bevel etch (Fig. 2b). Additionally, the bevel (Fig. 2b) and shaft (Fig. 2h) etches can be combined to produce solid microneedles which can be used for insertion testing, as the force required is the same for microneedles with or without the central bore.[27] The integration of the bore with the solid needles offers no further process complications (Fig. 9).

The three processes in combination are used to fabricate a hollow microneedle that can be produced in variable lengths, depending on application. The MN die are then singulated and mounted to syringe adaptors for delivery applications, or coated with metals to create electrodes for theranostic use.[25]

Further improvements to the etch quality could be made with optimisation of the masking and lithography steps. Patterning PR on an angled surface such as the bevel introduces unique challenges, where any PR defects present

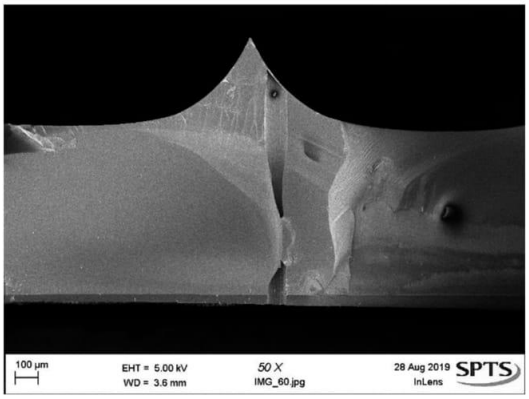

Fig. 8 SEM image showing the bore etch performed on a bevel surface. The bore transfers to bevel wafers with no issues, stopping on a backside layer.

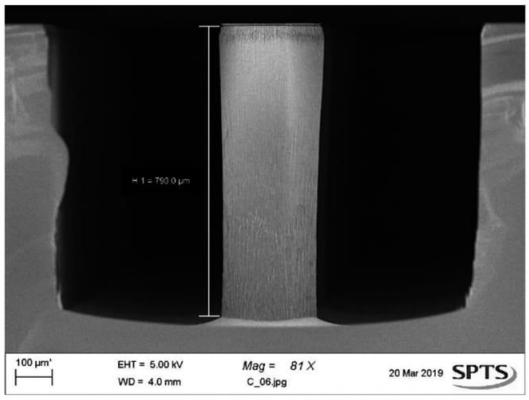

Fig. 7 SEM image showing the shaft, etched for microneedle length of 790 μm on a test wafer.

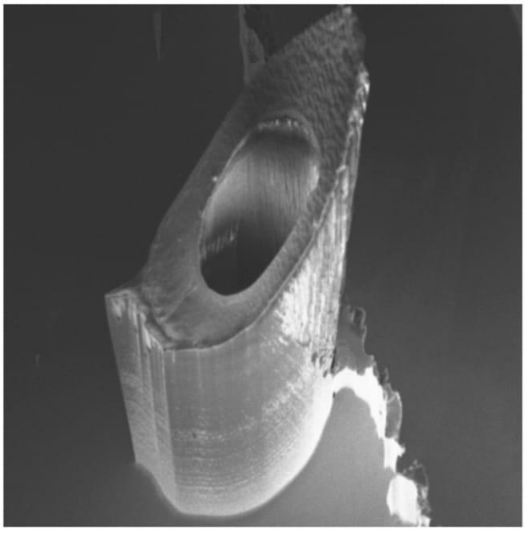

Fig. 9 Silicon microneedle with central bore.[1]

on the wafer surface results in roughness and isolated silicon spikes during the etch. Within the current patterning regime, the microneedle etch has been optimised to reduce these effects by increasing the time of the shaft etch E2 step to undercut any defects present on the bevel surface, minimising roughness in the final device.

Delivery through hollow microneedles

Mechanical testing

Axial compression tests (n = 3) were performed on 1 × 5 MN arrays using a Hounsfield/Tinius Olsen compression analyser (model H1-KS). A 50 N load cell enabled the compression platform to descend, exerting an increasing force on the MNs at a fixed rate of 4.5 mm s^{-1} to determine the point of fracture. The analyser detected several MN fractures over a compression distance of 250–400 μm, which is attributable to each of the 5 MNs breaking over different compression distances. The results indicate that the MN arrays withstand a maximum force of 22 N before completely fracturing, showing that a MN array has sufficient mechanical strength to resist fracture upon thumb pressure insertion, which is deemed to be <10N.[32] Furthermore, as the compression platform is composed of hard metal with little elasticity or movement, it is likely that the MN will be able to withstand a greater force upon penetration through the softer, elastic skin.

Insertion testing

Proof of concept experiments were conducted using 1 × 5 microneedle arrays. A single array was glued to a syringe adaptor that was attached to a syringe *via* a Luer-lock (Fig. 11, Right). To determine whether the microneedles were sharp enough to penetrate through the *stratum corneum*, methylene blue staining was conducted, following insertion of MNs. Methylene blue is a hydrophilic, low molecular weight molecule that cannot diffuse through the hydrophobic *stratum corneum* independently. Any exposure of the hydrophilic viable cells beneath the *stratum corneum* would stain blue, indicating that the *stratum corneum* had been breached.[33] Microneedles were inserted into porcine skin (Wetlab Ltd. Warwicks, UK) *via* thumb pressure, stained with methylene blue (Sigma-Aldrich, Dorset, UK) for five minutes and washed with ethanol wipes. Fig. 10 shows visual confirmation of the penetration of all five microneedles.

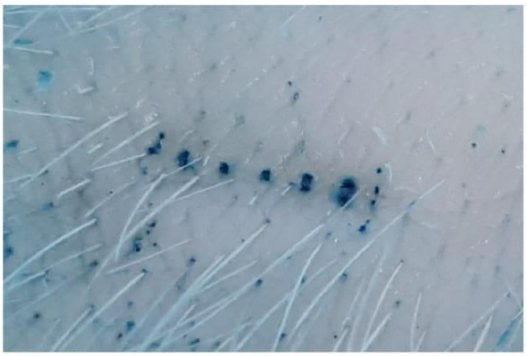

Fig. 10 Visual skin penetration efficiency of 1 × 5 microneedle array, stained with methylene blue. Imaged with a Samsung A70 (2019) smartphone.

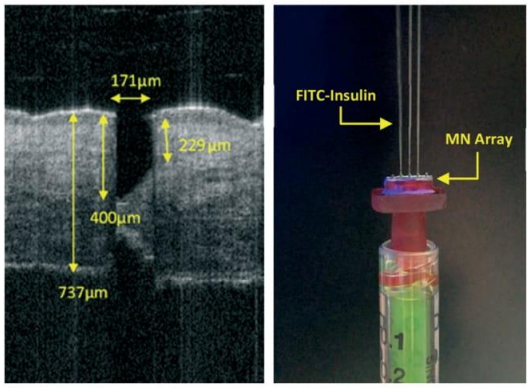

Fig. 11 Left; OCT imaging of excised human breast skin after the application of a silicon microneedle. Right; FITC-insulin injection through hollow microneedles attached to a syringe, imaged with a Samsung A70 (2019) smartphone.

Skin penetration and fluid flow

To demonstrate microneedle penetration depths, optical coherence tomography (OCT) on excised human breast tissue (local research ethics committee reference 08/WSE03/55) was performed (Fig. 11, Left). The OCT image clearly shows an insertion profile, characteristic of a bevelled tip microneedle, illustrating efficient microneedle penetration through the *stratum corneum*. The total length of the microneedle pre-penetration measured 700 μm, however, the OCT indicated the microneedle formed an insertion channel profile of at least 400 μm–57% of the original length. At this penetration depth, it was confirmed that the bore of the microneedle was fully inserted beneath the *stratum corneum* and into the epidermis. Depth measurements were extracted using ImageJ software.

Testing of hollow microneedles for their injection potential was conducted using FITC-labelled insulin that fluoresces under UV (ultraviolet) light. Fig. 11 (Right) demonstrates a microneedle adaptor Luer-locked to a syringe. Upon applying thumb pressure to the syringe plunger, straight, consistent liquid jets were produced, indicating FITC-insulin (Sigma-Aldrich, Dorset, UK) was able to flow easily through the microneedle bores of three out of five microneedles. The lack of flow in the two other microneedles was due to adhesive blocking the bore.

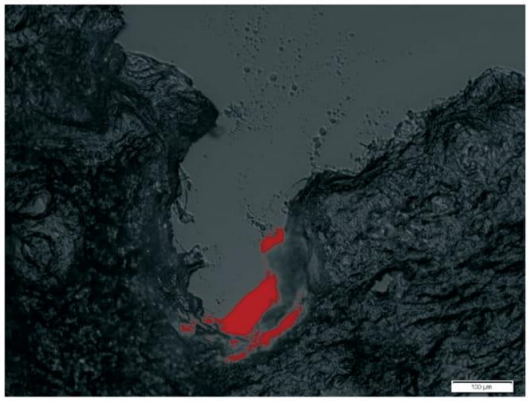

Fig. 12 Histology cross section of microneedle microchannel with DIL fluorescent dye injection.

Transdermal fluid injection

To confirm the capability of the microneedles for injection into porcine skin, a syringe was loaded with DIL fluorescent dye (Sigma-Aldrich, Dorset, UK) and attached to a syringe pump; a constant flow rate of 10 μl min^{-1} was applied. 10 μl of DIL was injected into porcine skin and the sample immediately frozen in liquid nitrogen. Skin was then sectioned vertically to a thickness of 8 μm using a cryostat (Leica, Milton Keynes, UK) to visualise the microneedle insertion profile and dye staining of the skin tissue surrounding the injection site.

The micrograph (Fig. 12) shows a microneedle insertion channel with a strongly fluorescent region at the apex of where the MN was injected; this area fluoresces at the emission wavelength 565 nm characteristic of DIL. As the dye is highly concentrated at the base of the micro insertion channel, this confirms the dye is injected *via* microneedle penetration and not introduced through natural skin conduits. The dye did not leak out over the microchannel cavity and was retained at the base; this suggests that hollow silicon microneedles are suitable for transdermal injection and facilitate delivery of substances including pharmaceutical compounds into epidermal and dermal skin layers.

Conclusions

The microneedles produced by the novel manufacture flow (Fig. 2) presented here offer significant advantages over other injection methods currently available. The sub-millimetre construction limits the risk of injury[4,7–10] and reduces pain in patients *via* facile injection,[2–4] potentially countering patient phobia of hypodermic needle use.[2,34] In addition to the benefits over conventional hypodermic injection, the hollow bevelled silicon microneedle allows for greater versatility than other microneedles. Forced injection through the centre TSV (bore) allows for controlled fluid volume delivery, whilst the sharp bevelled tip limits pain for patients by reducing insertion force.[2,27] In addition, the semiconducting base material introduces a pathway to future theranostic device chips.[25]

Conflicts of interest

There are no conflicts of interest to declare.

Acknowledgements

Funding provided by EPSRC EP/L020734/1, Welsh Government Smart Expertise "ASSET", Knowledge Economy Skills Scholarships (KESS), a pan-Wales higher level skills initiative led by Bangor University on behalf of the HE sector in Wales. It is part funded by the Welsh Government's European Social Fund (ESF) convergence programme for West Wales and the Valleys.

References

1 K. Roberts, H. Ashraf and P. F. Eng, *EP3415465A1*, 2018.
2 H. S. Gill, D. D. Denson, B. A. Burris and M. R. Prausnitz, *Clin. J. Pain*, 2010, **24**, 585–594.
3 S. Kaushik, A. H. Hord, D. D. Denson, D. V. McAllister, S. Smitra, M. G. Allen and M. R. Prausnitz, *Anesth. Analg.*, 2001, **92**, 502–504.
4 M. R. Prausnitz, J. A. Mikszta, M. Cormier and A. K. Andrianov, *Curr. Top. Microbiol. Immunol.*, 2009, **333**, 369–393.
5 R. F. Donnelly, T. R. R. Singh, M. M. Tunney, D. I. J. Morrow, P. A. McCarron, C. O'Mahony and A. D. Woolfson, *Pharm. Res.*, 2009, **26**, 2513–2522.
6 E. M. Vicente-Perez, E. Larrañeta, M. T. C. McCrudden, A. Kissenpfennig, S. Hegarty, H. O. McCarthy and R. F. Donnelly, *Eur. J. Pharm. Biopharm.*, 2017, **117**, 400–407.
7 J. I. Blenkharn, *British Journal of Nursing*, 2009, **18**, 860–864.
8 *Managing the Risk of Sharps Injuries*, NHS Employers, 2015.
9 C. Cooley and J. Gabriel, *Nursing Times*, 2004, vol. 100, pp. 28–29.
10 S. Q. Wilburn and G. Eijkemans, *Int. J. Occup. Environ. Health*, 2004, **10**, 451–456.
11 I. Mansoor, U. O. Hafeli and B. Stoeber, *J. Microelectromech. Syst.*, 2012, **21**, 44–52.
12 D. Duan, C. Moeckly, J. Gysbers, C. Novak, G. Prochnow, K. Siebenaler, L. Albers and K. Hansen, *Curr. Drug Delivery*, 2011, **8**, 557–565.
13 S. P. Davis, W. Martanto, M. G. Allen and M. R. Prausnitz, *IEEE Trans. Biomed. Eng.*, 2005, **52**, 909–915.
14 Y. Li, H. Zhang, R. Yang, Y. Laffitte, U. Schmill, W. Hu, M. Kaddoura, E. J. M. Blondeel and B. Cui, *Microsyst. Nanoeng.*, 2019, **5**, 11.
15 P. Janphuang, M. Laebua, C. Sriphung, P. Taweewat, A. Sirichalarmkul, K. Sukjantha, N. Promsawat, P. Leuasoongnoen, S. Suphachiaraphan, K. Phimol, D. Isarakorn and S. Tancharakorn, presented in part at the *ICEAST 2018*, 2018.
16 J.-H. Oh, H.-H. Park, K.-Y. Do, M. Han, D.-H. Hyun, C.-G. Kim, C.-H. Kim, S. S. Lee, S.-J. Hwang, S.-C. Shin and C.-W. Cho, *Eur. J. Pharm. Biopharm.*, 2008, **69**, 1040–1045.

17 E. García-López, H. R. Siller and C. A. Rodríguez, presented in part at the *46th SME North American Manufacturing Research Conference*, NAMRC 46, Texas, USA, 2018.
18 S. Ahmad, A. Ghani, A. Yaqoob and O. Singh, *Int. J. Curr. Res. Rev.*, 2017, **9**, 24–29.
19 M. C. Ottino, A. Argentero, P. A. Argentero, G. Garzaro and C. M. Zotti, *BMJ Open*, 2019, **9**, 1–8.
20 P. Jurcicek, H. Zou, S. Zhang and C. Liu, *Micro Nano Lett.*, 2013, **8**, 78–81.
21 H. Kim, L. S. Theogarajan and S. Pennathur, *J. Micromech. Microeng.*, 2018, **28**, 035007.
22 H. J. G. E. Gardeniers, R. Luttge, E. J. W. Berenschot, M. J. D. Boer, S. Y. Yeshurun, M. Hefetz, R. V. T. Oever and A. V. D. Berg, *J. Microelectromech. Syst.*, 2003, **12**, 855–862.
23 P. Khanna, K. Luongo, J. A. Strom and S. Bhansali, *J. Micromech. Microeng.*, 2010, **20**, 045011.
24 B. Wu, A. Kumar and S. Pamarthy, *J. Appl. Phys.*, 2010, **108**, 051101.
25 S. Jeelani, R. C. J. Reddy, T. Maheswaran, G. S. Asokan, A. Dany and B. Anand, *J. Pharm. BioAllied Sci.*, 2014, **6**, 6–8.
26 M. T. C. McCrudden, E. McAlister, A. J. Courtenay, P. González-Vázquez, T. Raghu, R. Singh and R. F. Donnelly, *Exp. Dermatol.*, 2015, **24**, 561–566.
27 S. P. Davis, B. J. Landis, Z. H. Adams, M. G. Allen and M. R. Prausnitz, *J. Biomech.*, 2004, **37**, 1155–1163.
28 F. Laermer and A. Schilp, US5501893A, 1994.
29 M. Motoyoshi, *Proc. IEEE*, 2009, **97**, 43–48.
30 Y. Tang, A. Sandoughsaz and K. Najafi, presented in part at the *2017 IEEE 30th International Conference on Micro Electro Mechanical Systems (MEMS)*, Las Vegas, NV, 2017.
31 B. Gualeni, S. A. Coulman, D. Shah, P. F. Eng, H. Ashraf, P. Vescovo, G. J. Blayney, L.-D. Piveteau, O. J. Guy and J. C. Birchall, *Br. J. Dermatol.*, 2018, **178**, 731–739.
32 S. Sharma, A. Saeed, C. Johnson, N. Gadegaard and A. E. Cass, *Sens. Biosensing Res.*, 2017, **13**, 104–108.
33 K. Moronkeji, S. Todd, I. Dawidowska, S. D. Barrett and R. Akhtar, *J. Controlled Release*, 2017, **265**, 102–112.
34 B. Deacon and J. Abramowitz, *Anxiety Disorders*, 2006, **20**, 946–960.